THE DESCENT IMAGER/SPECTRAL RADIOMETER (DISR) EXPERIMENT ON THE HUYGENS ENTRY PROBE OF TITAN

M. G. TOMASKO, D. BUCHHAUSER, M. BUSHROE, L. E. DAFOE, L. R. DOOSE, A. EIBL, C. FELLOWS, E. McFARLANE, G. M. PROUT, M. J. PRINGLE, B. RIZK, C. SEE, P. H. SMITH and K. TSETSENEKOS

Lunar and Planetary Laboratory, University of Arizona, Tucson, AZ, 85721, USA

Received 20 January 1999; Accepted in final form 3 November 1999

Abstract. The payload of the Huygens Probe into the atmosphere of Titan includes the Descent Imager/Spectral Radiometer (DISR). This instrument includes an integrated package of several optical instruments built around a silicon charge coupled device (CCD) detector, a pair of linear InGaAs array detectors, and several individual silicon detectors. Fiber optics are used extensively to feed these detectors with light collected from three frame imagers, an upward and downward-looking visible spectrometer, an upward and downward looking near-infrared spectrometer, upward and downward looking violet phtotometers, a four-channel solar aerole camera, and a sun sensor that determines the azimuth and zenith angle of the sun and measures the flux in the direct solar beam at 940 nm. An onboard optical calibration system uses a small lamp and fiber optics to track the relative sensitivity of the different optical instruments relative to each other during the seven year cruise to Titan. A 20 watt lamp and collimator are used to provide spectrally continuous illumination of the surface during the last 100 m of the descent for measurements of the reflection spectrum of the surface. The instrument contains software and hardware data compressors to permit measurements of upward and downward direct and diffuse solar flux between 350 and 1700 nm in some 330 spectral bands at approximately 2 km vertical resolution from an alititude of 160 km to the surface. The solar aureole camera measures the brightness of a 6° wide strip of the sky from 25 to 75° zenith angle near and opposite the azimuth of the sun in two passbands near 500 and 935 nm using vertical and horizontal polarizers in each spectral channel at a similar vertical resolution. The downward-looking spectrometers provide the reflection spectrum of the surface at a total of some 600 locations between 850 and 1700 nm and at more than 3000 locations between 480 and 960 nm. Some 500 individual images of the surface are expected which can be assembled into about a dozen panoramic mosaics covering nadir angles from 6° to 96° at all azimuths. The spatial resolution of the images varies from 300 m at 160 km altitude to some 20 cm in the last frames. The scientific objectives of the experiment fall into four areas including (1) measurement of the solar heating profile for studies of the thermal balance of Titan; (2) imaging and spectral reflection measurements of the surface for studies of the composition, topography, and physical processes which form the surface as well as for direct measurements of the wind profile during the descent; (3) measurements of the brightness and degree of linear polarization of scattered sunlight including the solar aureole together with measurements of the extinction optical depth of the aerosols as a function of wavelength and altitude to study the size, shape, vertical distribution, optical properties, sources and sinks of aerosols in Titan's atmosphere; and (4) measurements of the spectrum of downward solar flux to study the composition of the atmosphere, especially the mixing ratio profile of methane throughout the descent. We briefly outline the methods by which the flight instrument was calibrated for absolute response, relative spectral response, and field of view over a very wide temperature range. We also give several examples of data collected in the Earth's atmosphere using a spare instrument including images obtained from a helicopter flight program, reflection spectra of various types of terrain, solar aureole measurements including the determination of aerosol size, and measurements of the downward flux

Space Science Reviews **104:** 469–551, 2002.

of violet, visible, and near infrared sunlight. The extinction optical depths measured as a function of wavelength are compared to models of the Earth's atmosphere and are divided into contributions from molecular scattering, aerosol extinction, and molecular absorption. The test observations during simulated descents with mountain and rooftop venues in the Earth's atmosphere are very important for driving out problems in the calibration and interpretion of the observations to permit rapid analysis of the observations after Titan entry.

1. Introduction

Optical measurements of solar radiation made inside Titan's atmosphere can reveal a great deal about many important physical processes occurring there. Measurement of the absorption of ultraviolet light determines the amount of energy available to drive the photochemical reactions that lead to changes in atmospheric composition and to the production of atmospheric aerosols. Measurement of the brightness of the sky near the disk of the sun, the solar aureole, constrains the size, shape, composition, and distribution of aerosols and cloud particles and their optical properties. These properties of the aerosols control their ability to absorb sunlight and emit thermal infrared radiation. Measurements of the net flux of solar energy as a function of altitude determine the amount of sunlight absorbed in each layer of the atmosphere, yielding the net solar heating rate. Knowledge of the particle properties, gas composition, and temperature profile permit computation of the net radiative cooling rate. This combined with the solar heating rate provides the radiative forcing for atmospheric dynamics, which in turn can affect the distribution of aerosol and cloud particles and influence climate. The composition, thermal balance, dynamics, and meteorology of the atmosphere also affect (and are affected by) the properties of the planetary surface. Images of the surface in reflected sunlight together with near infrared reflection spectra can reveal the nature of the surface and its interactions with atmospheric processes.

The Descent Imager/Spectral Radiometer (DISR) is the optical instrument aboard the Huygens Probe that makes measurements at solar wavelengths. This instrument was developed in a collaborative effort by scientists from the US, France, and Germany. The list of Co-Investigators for the DISR experiment includes M. G. Tomasko, L. R. Doose, and P. H. Smith (of the University of Arizona), R. West (of the Jet Propulsion Laboratory), R. Solderblom (of U.S.G.S. in Flagstaff), B. Bézard, M. Combes, A. Coustenis, C. deBergh, and E. Lellouch (of the Paris Observatory (PO)), B. Schmitt (of the Institute of Glaciology in Grenoble, France), H. U. Keller and N. Thomas (of the Max Planck Insitute for Aeronomy (MPAE) in Lindau, Germany), and F. Gliem (of the Technical Institute of Braunschweig (TUB), Germany). For the U.S. effort, our key aerospace partner was Lockheed Martin Aerospace (LMA) in Denver.

By including substantial hardware contributions from several institutions in Europe, a significantly more capable instrument was developed than would have

been possible using the resources of one country alone. DISR measures solar radiation using silicon photodiodes, a two-dimensional silicon Charge Coupled Device (CCD) detector (provided by H. U. Keller and our German investigators) along with two InGaAs near-infrared linear array detectors (provided by B. Bézard and our investigators from Paris). Fiber optics (developed by Lockheed Martin Aerospace with our U.S. investigators) connect the detectors to many separate sets of fore-optics that collect light from different directions and in different spectral regions. In this way the instrument can make a suite of measurements carefully selected to answer key questions concerning the nature of Titan's surface and the composition, meteorology, thermal balance, and clouds and aerosols in the atmosphere of Titan.

The purpose of this paper is to describe the DISR instrument and the scientific investigation planned for its descent through Titan's atmosphere on the Huygens probe. We have previously described (Tomasko *et al.*, 1996, 1997) the design approach for the instrument. Here we concentrate on the properties of the instrument using measurements made after the instrument was completed, including some calibration measurements as well as measurements made from a helicopter and from the surface of the Earth. The scientific objectives of the experiment are outlined briefly in section 2 to set the context for the description of the instrumental approach summarized in section 3. Section 4 summarizes the measurements planned during the mission. Section 5 briefly summarizes the types of laboratory calibration data collected for the instrument. A final section shows a sample of data obtained from a test unit during our field test program on Earth, and serves to illustrate the ability of the flight experiment to meet our objectives at Titan.

2. Scientific Objectives

2.1. Thermal balance and dynamics

A basic objective of the DISR investigation is to measure directly the vertical profile of the solar heating rate. This will be done using measurements of the upward and downward solar flux over the spectral interval from 350 nm to 1700 nm between 160 km to the surface at a vertical resolution of approximately 2 km. The downward flux minus the upward flux gives the net flux, and the difference in the net flux at two altitudes gives the amount of solar energy absorbed by the intervening layer of atmosphere. Knowledge of the solar heating profile is necessary for understanding the thermal balance of Titan's atmosphere.

The combination of the solar heating profile with the thermal cooling profile provides the net radiative drive for atmospheric dynamics. The radiative cooling profile will be modeled using the temperature profile and the opacity of atmospheric gases and cloud and aerosol particles at wavelengths in the thermal infrared. The gaseous composition and temperature profile will be measured by other Huy-

gens and Cassini instruments. The DISR measurements make an important contribution by determining the size, shape, optical properties, and vertical distribution of aerosol and cloud particles. Using models for the variation of particle properties and thermal profile over the surface of Titan, the variations of solar heating and thermal cooling over the disk can be computed. Once the solar heating and thermal cooling have been combined, model computations can be used to estimate the wind field from the radiative forcing.

Finally, DISR will measure the horizontal wind direction and speed as functions of altitude from sets of panoramic images of the surface obtained every few kilometers in altitude which will show the drift of the probe over the surface of Titan. Sets of 36 images covering nadir angles from 6° to 96° around a full 360° in azimuth are obtained within two minute periods during imaging operations. Overlap between individual images, views of the horizon, and housekeeping observations of the orientation of the probe are available to determine the motion of the instrument platform relative to the vertical when these images were obtained. This information will be used to separate angular motion under the parachute from drift over the surface between the times of successive image panoramas. The measured wind speed and direction determined by DISR can be compared to the wind field computed from the net radiative forcing determined above.

2.2. Distribution and properties of aerosol and cloud particles

Several properties of the cloud and aerosol particles are important for understanding their interaction with the solar and thermal radiation field. The size of the particles compared to the wavelength of the radiation is important for understanding particle scattering. Measurements of both the forward scattering and polarizing nature of the aerosols on Titan have been used to show that spherical particles can not simultaneously explain these two types of observations (see Hunten *et al.*, 1985). Information on particle shape in addition to size is therefore required for understanding particle scattering. The vertical distribution of the particles also influences the profiles of solar and thermal radiation. Finally, a suite of optical properties as functions of wavelength are needed to permit accurate computations of the interactions of the particles with radiation. These properties include the optical depth, single scattering albedo, and the shape of the scattering phase function. The variation of these optical properties with wavelength, together with determinations of size and shape, can yield the imaginary refractive index and thus constrain the composition of the particles.

DISR will measure many of these properties using combinations of measurements of small-angle scattering in the solar aureole in two colors, measurements of side- and back-scattering in two colors and two planes of polarization, measurements of extinction as a function of wavelength from the blue to the near infrared, and measurements of the diffuse transmission and reflection properties of layers in the atmosphere as outlined in sections 3 and 4.

2.3. NATURE OF THE SURFACE

The surface of Titan was hidden from view of the cameras aboard the Pioneer and Voyager spacecraft by the layers of small haze particles suspended in the atmosphere. Nevertheless, intriguing suggestions regarding the nature of the surface have been made (Lunine, 1993), including the possibility that the surface consists of a global ocean of liquid methane-ethane. Recent radar observations and direct observations at longer wavelengths by the Hubble Space Telescope (Smith *et al.*, 1996; Lemmon *et al.*, 1995) show that the surface is not a global ocean. The many fascinating surfaces observed by the Voyager mission on satellites of the outer solar system showed a surprising range of phenomena including craters, glacial flows, frost and ice coverings, and active geysers and volcanoes. These preliminary explorations of the small bodies of the outer solar system suggest that the surface of Titan may well also contain surprises.

DISR will determine the physical state (solid or liquid) of the surface near the probe impact site, and determine the fraction of the surface in each state. DISR will measure the topography of the surface, thus constraining some of the physical processes that have formed the surface. DISR will obtain reflection spectra of surface features from the blue to the near infrared in order to constrain the composition of the different types of terrain observed. In addition, DISR will image the surface at resolution scales from hundreds of meters (similar to those accessible from the orbiter) to tens of centimeters over as large an area as possible to permit studies of the physical phenomena occurring on the surface and to clarify the physical interactions of the surface and the atmosphere.

2.4. COMPOSITION OF THE ATMOSPHERE

The Huygens Probe contains a mass spectrometer/gas chromatograph to measure directly the composition of the atmosphere. Nevertheless, direct sampling techniques can give inaccurate mixing ratios for condensable constituents if a cloud particle enters and slowly evaporates in the inlet system, as happened during the Pioneer Venus mission (Hoffman *et al.*, 1980). The DISR provides an important complementary capability for measuring the mixing ratio of methane, the most likely condensable constituent, using a technique that is not subject to this potential problem. The mixing ratio of methane will be obtained from the increasing depth of methane absorption bands as the gas path between the instrument and top of the atmosphere increases during the descent.

Methane can exist as a solid, liquid, or gas on Titan, and has been suggested to play a role in the meteorology of Titan similar to the role played by water on the Earth. The DISR measurements of the methane mixing profile will be analogous to a relative humidity profile on the Earth.

Finally, the atmosphere of Titan is believed to consist primarily of nitrogen, methane and argon. The DISR measurements of the mixing ratio of methane together with the determination of total mean molecular weight of the atmosphere by

radio occultation measurements made by the Cassini Orbiter will indirectly yield the argon to nitrogen mixing ratio as an important backup to the mass spectrometer measurements planned for the Huygens Probe.

3. Instrument Approach

3.1. Overview

In order to achieve this broad range of scientific objectives, it is necessary to measure the brightness of the sunlight in Titan's atmosphere with several different spatial fields of view, in several directions, and with various spectral resolutions. For measurements of solar energy deposition, for example, measurements are needed of the downward and upward solar flux with broad and flat spectral sensitivity, and with a cosine zenith angle weighting. For determination of the composition of the surface, spectral resolution is desirable, and spatial information is necessary. For determination of the physical processes occurring on the surface, images are needed with very broad fields of view looking downward toward the surface. To determine the size distribution of aerosol particles above the altitude of the probe, upward-looking measurements are needed of the brightness of the region of the sky near the sun (the solar aureole) in at least two colors with modest angular resolution. Images looking outward toward the horizon are useful for sensing the presence of thin haze layers during the descent.

It was not possible to include in the limited payload of the Huygens Probe separate instruments devoted to each of these scientific measurements. Nevertheless, it has been possible to increase considerably the usefulness of the single Huygens optical instrument by making extensive use of fiber optics to collect light from different directions and bring it to a few centrally located detectors after various spectral or spatial analyses. In this way redundant electrical systems have been minimized, and moving mechanical parts have been all but eliminated. A parachute swivel and rotation vanes on the perimeter of the probe provide a rotating platform for direct and diffuse sensing as well as image mosaics. A summary of the locations of the fields of view and spectral coverage of the DISR optical measurements is given in Table 1.

The DISR instrument can be thought of as consistng of two halves, one using a charge coupled device (CCD) array detector and the other half built around a pair of linear near infrared array detectors. The pair of linear array detectors are at the focus of a small grating spectrometer as shown schematically in Figure 1. The grating spectrometer is fed by two optical fibers. One fiber looks down and a small lens is used to collect light from a 3° by 9° field of view centered at 20° nadir angle. This permits measurement of the intensity as a function of wavelenth coming from this location on the ground. As the probe rotates, information is collected over the entire range of azimuth angles. Models are used for the variation of the intensity

TABLE 1
Summary of DISR instruments

Upward-Looking Instrument	Azimuth Range	Zenith Range	Spectral Range (nm)	Spectral Scale (per pixel)	Spatial Scale (per pixel)	Pixel Format
Violet Photometer (ULV)	170°	5°–88°	350–480	–	–	1
Visible Spectrometer (ULVS)	170°	5°–88°	480–960	2.4 nm	–	8 × 200
Infrared Spectrometer (ULIS)	170°	5°–88°	870–1700	6.3 nm	–	132
Solar Aureole (SA 1) Vertical Polarization	6°	25°–75°	500±25	–	1°	6 × 50
Solar Aureole (SA 2) Horizontal Polarization	6°	25°–75°	500±25	–	1°	6 × 50
Solar Aureole (SA 3) Vertical Polarization	6°	25°–75°	935±35	–	1°	6 × 50
Solar Aureole (SA 4) Horizontal Polarization	6°	25°–75°	935±35	–	1°	6 × 50
Sun Sensor (SS) (64°cone FOV)	64°cone	25°–75°	939±6	–	–	1
Downward-Looking Instrument	**Azimuth Range**	**Nadir Range**	**Spectral Range (nm)**	**Spectral Scale (per pixel)**	**Spatial Scale (per pixel)**	**Pixel Format**
Violet Photometer (DLV)	170°	5°–88°	350–480	–	–	1
Visible Spectrometer (DLVS)	4°	10°–50°	480–960	2.4 nm	2°	20 × 200
Infrared Spectrometer (DLIS)	3°	15.5°–24.5°	870–1700	6.3 nm	–	132
High-Resolution Imager (HRI)	9.6°	6.5°–21.5°	660–1000	–	0.06°	160 × 256
Medium-Resolution Imager (MRI)	21.1°	15.75°–46.25°	660–1000	–	0.12°	176 × 256
Side-Looking Imager (SLI)	25.6°	45.2°–96°	660–1000	–	0.20°	128 × 256

with nadir angle, and the observations are used to constrain the upward solar flux at wavelengths from 850 to 1700 nm. The second feed fiber for the IR spectrometer looks at the bottom of a horizontal diffusing plate. The plate is surrounded by an external baffle that limits its field of view to zenith angles from 5° to 88° and to

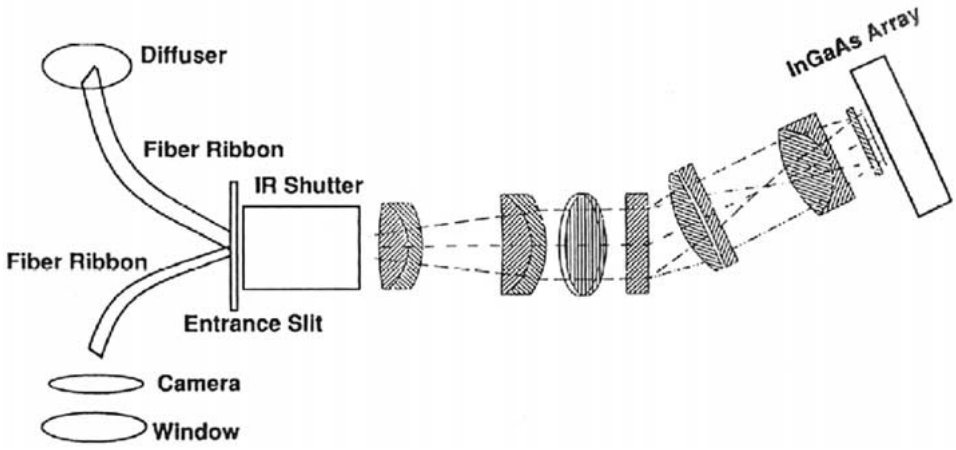

Figure 1. Schematic layout of the infrared spectrometer. Separate fiber ribbons bring the light from a diffuser (looking up) and from a camera lens (looking down) to adjacent positions along the input slit of the spectrometer. A small mechanical shutter located just behind the input slit can be commanded open or closed to separately measure the dark current of the detector when it is warm and the total bright plus dark signal. The light leaving the grating spectrometer is focused on the pair of linear detectors. Also shown is a tipped glass plate which is oriented to partially compensate for the different efficiency of the grating for input light which is linearly polarized parallel or perpendicular to the grooves of the grating.

170° in azimuth. The baffle is termed a 'bear's ear baffle' because of its appearance (see Figure 2). The diffusing plate makes the response of upward-looking IR spectrometer roughly proportional to the cosine of the zenith angle. Thus, the instrument measures half the diffuse downward flux plus the direct downward flux (when the sun is included in the field of view of the instrument) or only half the diffuse downward flux (when the probe has rotated so that the sun is behind the baffle).

The second half of the DISR instrument contains the CCD detector and the fiber optic bundle that feeds this detector. The fiber optic bundle is constructed so that different portions of the bundle are fed by different optical systems at the input end, but the light is all brought together in front of the CCD detector (see Figure 3). The gap between the end of the fiber optic bundle and the face of the CCD detector is <20 μm. The CCD pixels are 17 by 23 μm in size centered 23 μm apart both vertically and horizontally. Because the gap is smaller than a CCD pixel, not much resolution is lost across the gap between the end of the fiber optic conduit and the face of the CCD. The individual fibers in the fiber optic conduit are 8 μm in diameter, so several fibers feed each CCD pixel.

The sensative area of the CCD array is 520 by 256 pixels times 23 μm for each pixel, or about 12 mm horizontally by 5.9 mm vertically. The fiber optic conduit is about 6 by 12 mm at this end and is mounted very close to the face of the CCD. From here the fiber optic conduit is separated into nine different bundles. Three

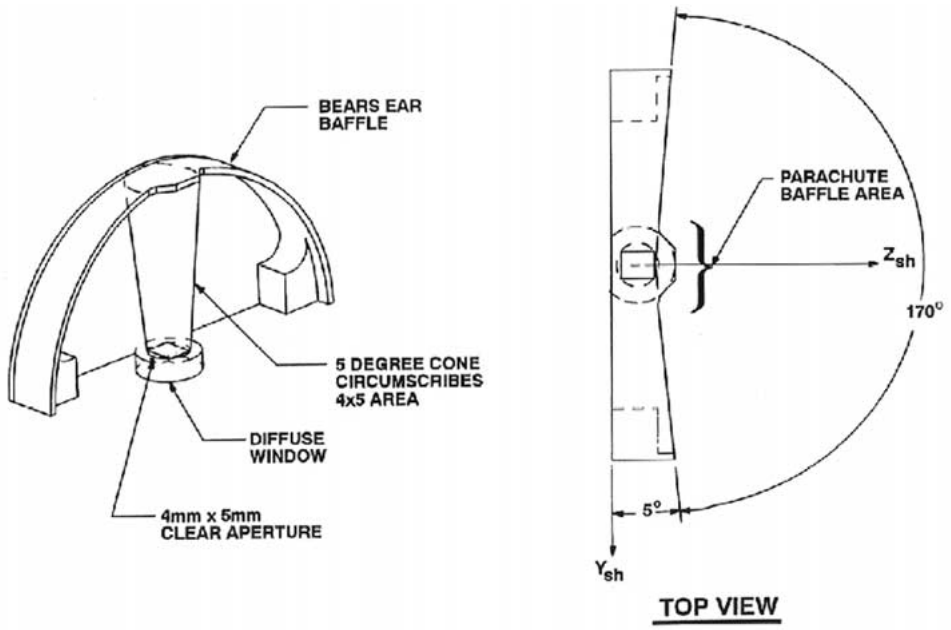

Figure 2. The shape of the 'bear's ear' baffle which surrounds the diffuser of the upward-looking infrared spectrometer to define its limit its field of view to 170° in azimuth and to the range from 5° to nearly 90° in zenith angle. The region within 5° of the zenith is masked to avoid viewing the parachute.

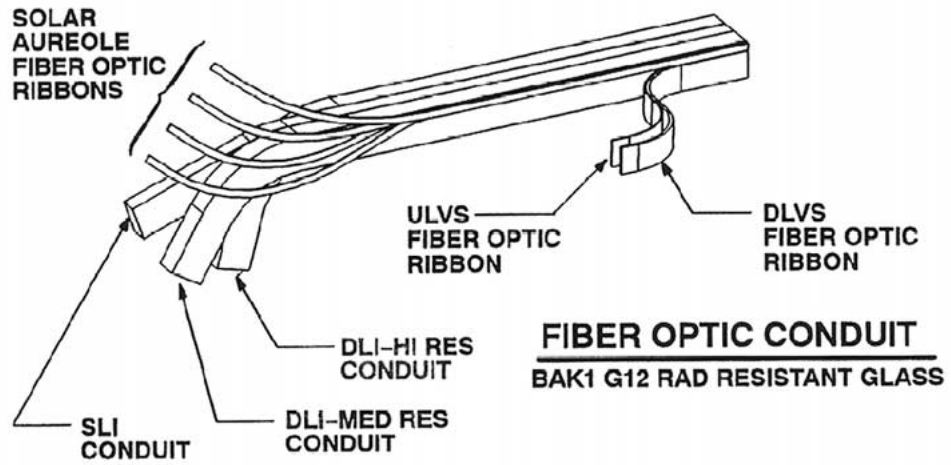

Figure 3. The layout of the fiber optic conduit which brings light from the three imagers, from the four-channel solar aureole camera, and from the upward-looking and downward-looking visible spectrometer to the face of the CCD detector (right hand end of the conduit).

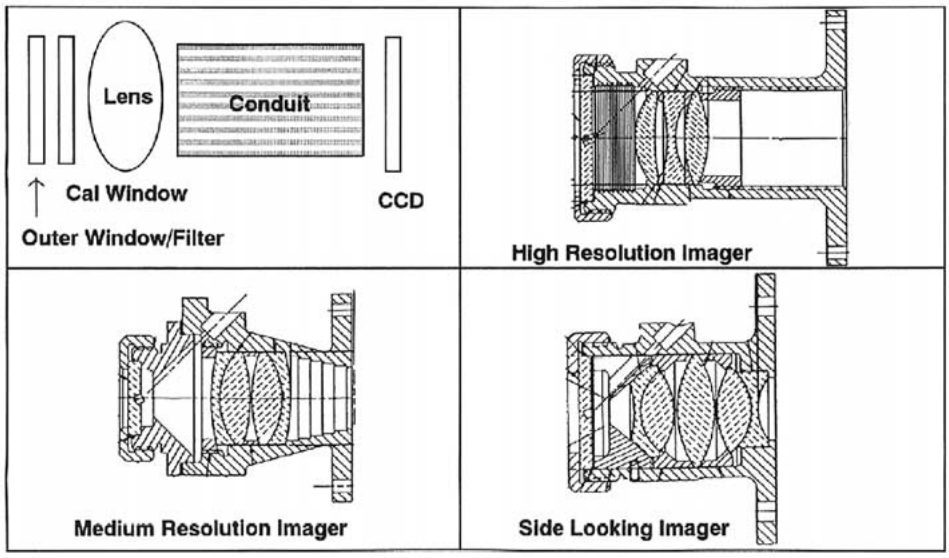

Figure 4. The schematic layout of the windows, lenses, fiber optic conduit, and CCD detector used for the three imagers. The configuration of the lenses in each of these imagers is also shown.

of the bundles (3.7 × 5.9 mm, 2.9 × 5.9 mm, and 4.0 × 5.9 mm lead to three separate lens systems pointed at central nadir angles of 14°, 31°, and 71°. The f/2.5 lenses at the end of each of these three fiber bundles focus an image on the front of each fiber bundle. The arrangement of the windows, lenses, image conduits, and the CCD detector is shown schematically in Figure 4.

Figure 5 shows the arrangement of the upward and downward-looking visible spectrometer windows, fibers, optics, and the CCD detector. Two separate fiber optic ribbons lead from the CCD detector to the focus of a small grating spectrometer. One of these ribbons feeds an area of 20 × 200 pixels (5 mm × 0.5 mm), while the other covers 8 by 200 CCD pixels. The thicker ribbon is used for the downward-looking portion of the visible spectrometer while the thinner ribbon is used for the upward-looking portion. At the input slit plane of the grating spectrometer, separate fibers lead to a small lens system that images the slit onto a 4° by 40° long region on the ground centered at 30° nadir angle. The other fiber leads to the bottom of a flat diffusing plate that is surrounded by an external 'bear's ear' baffle that limits its field of view from 5° to 88° zenith angle and to 170° in azimuth. In addition, a 10° wide shadow bar extends down roughly the center of the field of view. Data can be collected when the sun illuminates the diffuser, or when the sun is behind the shadow bar or behind the back of the baffle. Combinations of these measurements can yield the direct and diffuse downward solar flux.

Figure 6 shows the schematic layout of the solar aureole system. Four 6 × 50 pixel regions of the CCD are fed by separate ribbons of fibers that are fed by lenses, filters, and polarizers to image a strip of sky 6° wide in azimuth and extending from

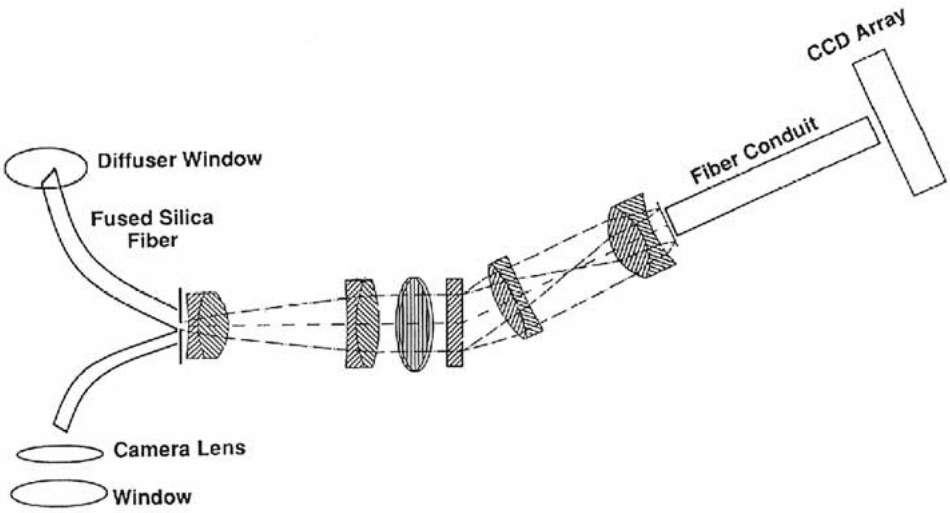

Figure 5. The schematic layout of the components of the upward and downward-looking visible spectrometer. The upward looking input views the bottom of a diffuser. The downward looking input uses a lens to project the entrance slit onto a $4^\circ \times 40^\circ$ region that extends from 10° to 50° nadir angle.

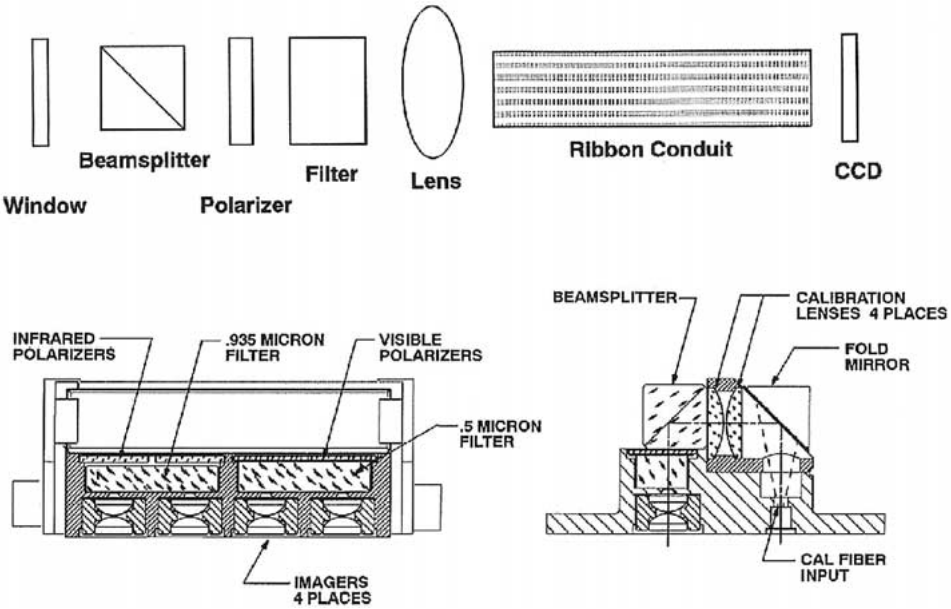

Figure 6. The schematic layout of the components of the solar aureole system. The beamsplitter is used to introduce light from the inflight calibration system into the four channels of the solar aureole system.

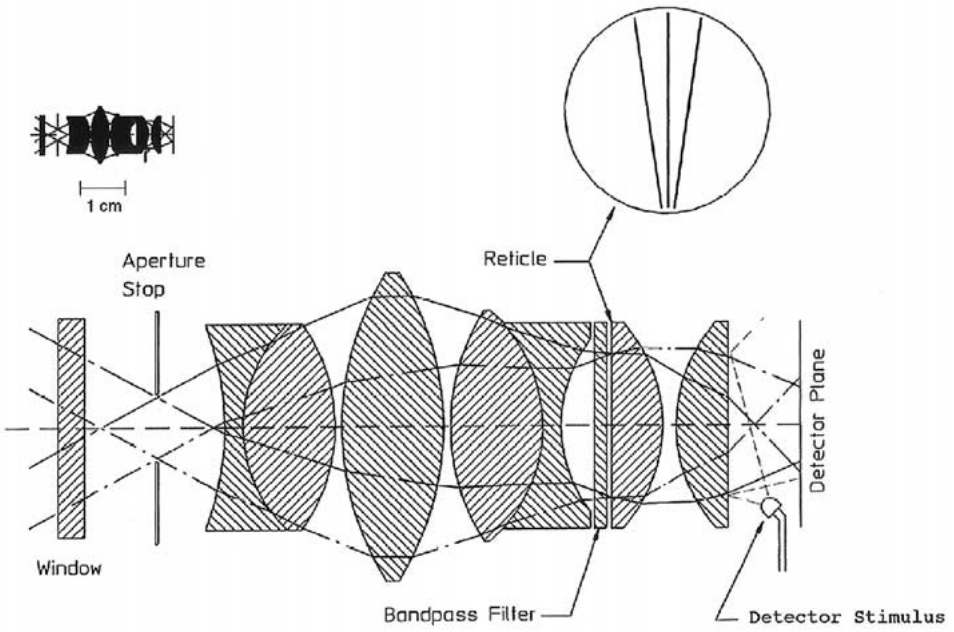

Figure 7. The schematic layout of the sun sensor. The three-slit reticle is deposited on the front of one of the plano-convex lenses next to the bandpass filter. The size of the optical elements are shown to scale in the upper left corner with a bar to indicate a size of 1 cm. The detector stimulus is used to inject pulses of light into the system to test functionality during cruise.

25° to 75° in zenith angle. These four strips are measured in two wavelengthe bands (near 500 and 935 nm). In each wavelength band, a linear polarizing analyzers are used to measure separately the horizontal and vertical components of linear polarization.

The separate grating spectromenters feeding the CCD and linear array detectors measure the upward and downward streaming solar flux from 480 nm to 960 nm and from 850 to 1700 nm, respectively. Two separate silicon detectors are used to extend the upward and downward flux measurements to the violet region between 350 and 480 nm. These individual detectors are placed behind diffusing plates mounted behind external 'bear's ear' baffles. The upward looking violet photometer (ULV) is placed behind the diffuser used by the ULVS, and shares the same external baffle and shadow bar. The downward looking violet photometer (DLV) uses a separate diffuser and bear's ear baffle.

Finally, a separate silicon detector, lens, and vertical slit assembly is used to determine when the instrument has rotated to the azimuth of the sun. The pulses generated by this system are used to control the azimuth at which measurements are made by the rest of the system. The schematic layout of this system is shown in Figure 7.

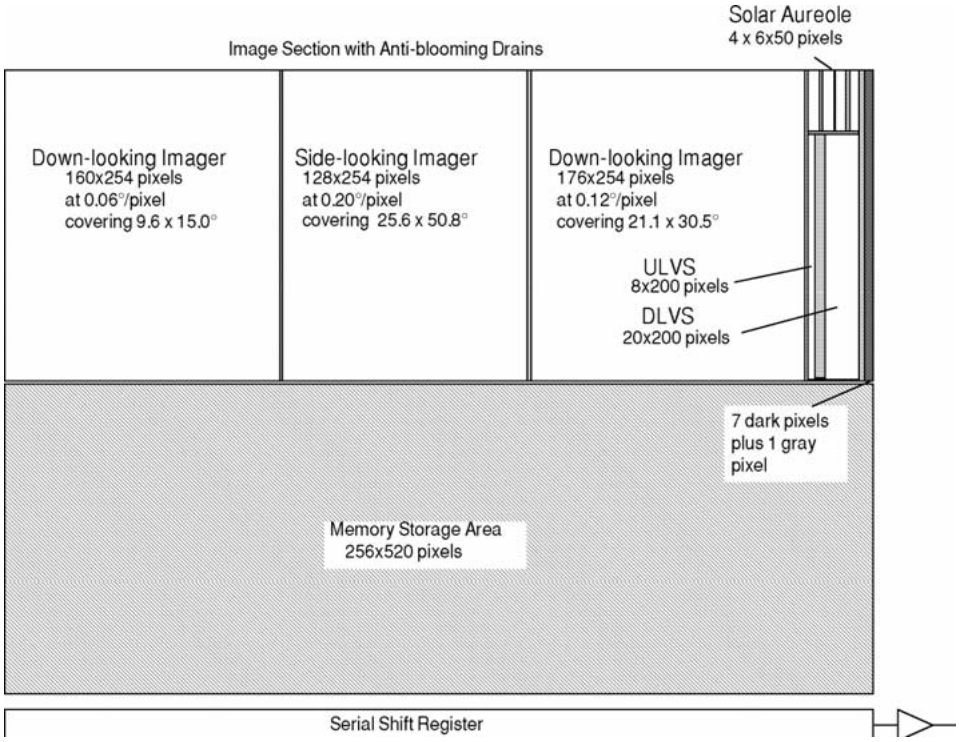

Figure 8. Layout of the face of the CCD detector.

3.2. DETECTORS

Co-I Dr. H. U. Keller of the Max Planck Institute for Aeronomy (MPAE) in Germany is responsible for the CCD subsystem. LORAL Fairchild supplied the flight CCDs to the MPAE group. The data interface between the German and American electronics is at the output of the 12-bit analog-to-digital (A/D) converter.

The format of the CCD is shown in Figure 8. The CCD is a 512 $\times$ 520 pixel frame transfer device. It is divided into an image section and a memory, or storage, section, each 256 $\times$ 520 pixels in size. The image section contains antiblooming drains on the side of each pixel. The individual pixels are 17 $\times$ 23 μm (sensitive area) on 23 μm centers. The CCD is fed by optical fibers from 9 optical subsystems: the HRI, MRI, SLI, ULVS, DLVS, and the four-channel SA radiometer (two colors in each of two orthogonal polarization states). The quantum efficiency of the CCD is $>$50% at the peak.

Exposure time is controlled by 0.5 ms shifts of the charge from the image section to the storage section of the chip which is covered by an opaque metal film. The exposure is the time between rapid shifts. No mechanical shutter is needed and no moving parts are used in this system. The full CCD frame is read out and digitized for imaging data, a process that takes about 2.2 seconds for the entire

frame. Only the first 49 columns are digitized for taking spectra and solar aureole measurements, thus shortening the readout time to about 300 ms when only these measurements are made.

After A/D conversion, the data are reduced from 12 to 8 bits/pixel by a square-root algorithm which balances the size of the quantization steps according to the distribution of shot noise in the observations. The image data are then compressed in a lossy hardware compressor by factors between 3 and 8:1. The hardware that accomplishes the lossy image compression was provided by Co-Investigator Dr. F. Gliem of the Technical Institute of Braunschweig, Germany. The spectral and solar aureole data from the CCD are compressed with a lossless software compression algorithm by a factor of about 2 and then buffered for transmission.

The dark current from the CCD is measured by the signals from the column of masked pixels along the edge of the chip. These data are read out and inserted into the telemetry stream once every few minutes. At Titan entry, the chip is at a temperature of some 260 K, and the dark current is a few percent of typical signals. After some 40 minutes of the nominal 140 minute descent, the detector cools to a temperature less than 200 K, and the dark current is essentially negligible.

The full well capacity of the CCD pixels is about 125,000 electrons. This is digitized at 30 electrons/step (before square-root compression). The read noise of the system is about 15 electrons. For all but the lowest signals, the data are shot-noise limited.

Two linear photodiode arrays (for the DLIS and the ULIS) along with their associated preamplifier electronics were provided by Co-I Dr. B. Bézard of the Paris Observatory. Each of the two arrays contains 150 individual InGaAs photodiodes bonded to a sapphire substrate and connected to CCD readout registers. The two modules are assembled on a ceramic base and are protected by a hermetically sealed titanium case which includes a coated sapphire window. A copper thermal lug bonded at the rear of the ceramic base and connected by a thermal strap to the exterior of the Huygens Probe is used for cooling the detector assembly. A silicon diode bonded onto the ceramic base provides a measure of the temperature of the focal plane array. Each pixel has a photo-active area of 38 by 300 μm. The pixel pitch is 52 μm. The detector arrays are used for detecting radiation with wavelengths from 850 to 1700 nm. Peak quantum efficiencies $>80\%$ were measured. The detector assembly was manufactured by Thomson-TCS (Saint Egreve, France). The general design is based on the technology used in the SPOT 4 satellite devoted to Earth observations (Bodin and Reulet, 1987). The IR preamplifier board in the sensor head and the clocking electronics (on a board in the DISR electronics assembly) were built by AETA (Fontenay-aux-roses, France).

Between readouts of the photodiodes, charge is accumulated both due to dark current and at a rate proportional to the flux of incident photons. Upon readout, this is digitized using a 14-bit A/D converter. The gain is 920 electrons per digital step with a full scale of some 14 million electrons. The dark current in the InGaAs diodes decreases roughly by a factor of 2.5 for every 10 K decrease in temperature.

Measurements at 270 K show dark currents in the range 0.5–2 pA. Somewhat larger dark currents are expected at Titan as a result of the impact of energetic protons during the cruise. The minimum time between reads is 8 msec, which is sufficiently short that only a small fraction of the wells contain dark current at the temperature (near 260 K) expected at the start of the Titan descent. After some 40 minutes, the temperature of the detector decreases to $<$200 K, and dark current is almost negligible.

A shutter mechanism (the only moving part in the entire DISR) at the entrance slit of the IR spectrometer permits separate measurements of the dark signal and the dark plus light signal throughout the descent. Spectra with shutter open and closed are both included in the telemetry stream. In addition, seven pixels at the beginning and end of the array are masked with an opaque resin and provide a measure of the typical dark current. In case of shutter failure, they would provide an estimate of the dark current that can be used to remove the dark signal from shutter-open spectra obatained at warm temperatures.

The readout noise has been measured to be $\sim$1100 electrons for temperatures $<$270 K. The shot noise is generally lower than the readout noise. About 10% of the pixels exhibit, in addition, a 1/f noise due to defects in the p-n junction of the diode itself. Its amplitude is roughly proportional to the dark signal and amounts to 0.1 to 1% of the dark level.

The CCD and IR array spectrometers together cover wavelengths from 480 nm to 1700 nm. There is considerable interest in the radiation shortward of 480 nm which is strongly absorbed by the aerosols in the upper stratosphere. Since there are only extremely weak methane bands in this part of the spectrum, high spectral resolution is not required. Two silicon photodiodes, appropriately filtered so that the bandpass between 350 and 480 nm gives a relatively flat spectral response, measure the flux in the upward and downward-looking directions.

3.3. DISR Sub-Instruments

3.3.1. *Imagers*

The design of the imagers is driven by several considerations. The range to Titan's surface decreases by three orders of magnitude during the descent from 160 km at entry to only a few hundred meters at the last image. Even the maximum range of 160 km is orders of magnitude less than is typical for images of planetary surfaces obtained by any other technique, including close flybys. Thus, the usual requirement for high angular resolution, necessary for observations made at longer range, are much relaxed in our case. We have chosen a maximum angular resolution of 0.06°/pixel, similar to that of the naked human eye. This pixel size of about one milliradian gives a spatial scale of 160 m/pixel at start of descent and about 10 cm/pixel at 100 m. The low resolution overlaps that available from orbiters and the high resolution near impact is three orders of magnitude greater.

Given the limitation of only 256 pixels across the active area of the CCD detector, even this relatively low angular resolution would limit the coverage in a single image to 15°. In order to observe as large an area as possible on the surface, we have chosen to divide the long dimension of the CCD into three image frames centered at different angles from the nadir that together cover a range of nadir angles from 6.5° to 96°. This is done with the division shown in Figure 8. As the probe rotates, sets of three images can be obtained at 12 azimuths to give a panorama with full coverage over nadir angles from 6.5° to 75°. A set of 24 images in azimuth, obtained in two staggered sets of 12 in successive measurement sets, permits full coverage in azimuth for the most side-looking imager and also completes the mosaic from nadir angles of 6.5° to 96°. The footprints on the surface of the individual images in a panoramic mosaic are shown in Figure 9.

The size of the imager pixels and their nadir angles define the relationship between integration time and blurring due to probe rotation during the image exposure. We limit the integration time so that rotation during the exposure is <1.5 times the angular size of a pixel in the center of the field of view of the High-Resolution Imager. The blur in the other imagers is less than that in the HRI.

This limitation on integration time translates into a relation between the f/number of the optical system and the signal-to-noise (S/N) ratio in the images for a model of the brightness of the surface of Titan. We selected an f/2.5 system to permit S/N > 100 at the rotation rate of 1.5 rpm expected at low altitudes for a nominal model of the surface of Titan and the quantum efficiency and transmission expected for the imaging system.

For good imaging, we require that the optical systems be capable of giving spot sizes (full width at half maximum) smaller than 2 CCD pixels. The spot size is produced by geometrical aberrations in the lenses, diffraction, and by the spreading of light between the back face of the fiber bundle and the surface of the CCD. Because the end of the fiber optic bundle is within 20 μm of the face of the CCD, spot sizes smaller than 2 pixels can be achieved.

The light is brought from the three separate lens assemblies to the face of the CCD by a fiber optic bundle produced by Collimated Holes, Inc. (CHI). The fibers are small compared to the 17×23 μm size of the active area of the CCD pixels, so that many (about 6) fibers feed each pixel. Extramural absorption is added between the clad fibers to absorb light that might emerge from individual fibers. The glass used for the fiber optic conduit is specially selected for resistance to darkening from energetic particle impact.

The spectral range of the imagers is limited to wavelengths between 660 and about 1000 nm. The long wavelength end is defined by the limit of the CCD detector. The short wavelength end is selected to prevent Rayleigh scattering by the atmosphere below the probe from dominating the signal due to light reflected directly by the surface. All three imagers have the same spectral range. Color can be added to the monochromatic images using measurements of spectral reflectivity of the surface measured by the DLVS. We plan to correlate the spectral measurements

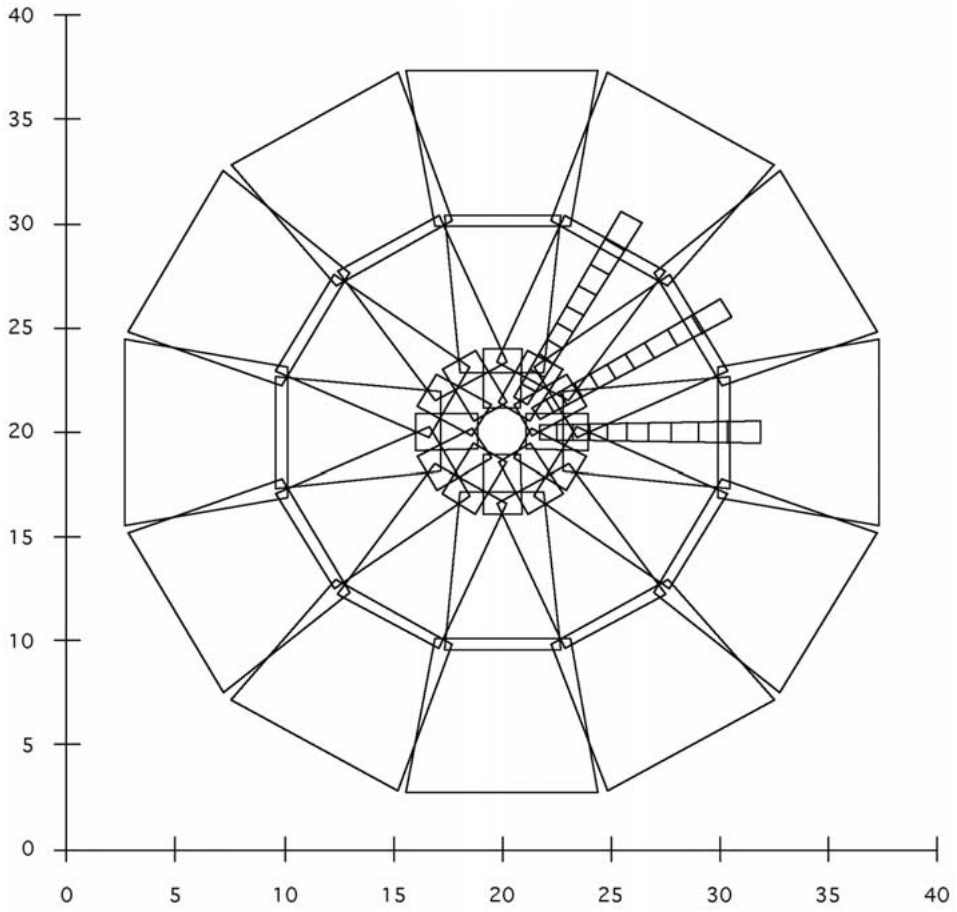

Figure 9. A view of the ground as seen from an altitude of 10 km showing the boundaries of individual images which together make a panoramic mosaic. The dimensions along the vertical and horizontal axes are distances in km. DISR also measures the spectral reflection of the surface at 10 $4^\circ \times 4^\circ$ locations along the slit of the DLVS at each of the 12 azimuths. (The locations of these spectral measurements are only shown at 3 azimuths here for clarity.)

of several thousand surface points with the morphology of these points as seen in the images to produce a library of color as a function of the type of terrain (craters, canyons, lakes, stream beds, etc.) In this way color images of the surface can ultimately be made from our measurements.

As described below, we expect to obtain more than 500 separate images of the surface which can be assembled into 36-image panoramic mosaics every few km from the start of descent at an altitude of 160 km to the surface.

3.3.2. *Visible Spectrometer*

Measurements of the spectrum of the upward and downward streaming sunlight as functions of altitude during the descent support most of the scientific objectives of the DISR experiment including: (1) measurement of the profile of the absorption of solar energy; (2) measurement of the vertical profile of methane; (3) measurements of the optical properties, size, and vertical distribution of atmospheric aerosols and clouds; and (4) measurements of the composition and nature of the surface of Titan. Accordingly, significant effort and experiment resources have been devoted to this portion of the instrument.

The visible spectrometer uses separate fiber bundles to bring downward- and upward-streaming sunlight to adjacent positions along the entrance slit. The speed of the collimator and camera optics of the transmission grating spectrometer is f/2. A tipped flat plate is included in the beam just before the grating to decrease the sensitivity of the measured intensity to the state of linear polarization of the incident light. The spectral range is limited by a filter to wavelengths from 480 to 960 nm in first order. The upward and downward-looking spectra are focused on the ends of two fiber optic ribbons which join the fiber conduit used for the imagers. The spectra are spread over 200 CCD pixels in the spectral direction. The spectral spread function has a width (FWHM) of two pixels. The resulting resolving power of the spectrometer, $\lambda/\Delta\lambda$, is 100 at the blue end and 200 at the red end of the spectrum.

The input optics used to collect the light from the upward and downward directions are quite different. In the upward-looking case, the design is driven by the desire to measure the downward-streaming flux. Thus, a horizontal diffusing plate is viewed by the input optical fibers using a small lens. The diffuser makes the angular response function similar to the ideal response function (proportional to the cosine of the zenith angle). Because the instrument protrudes only a small distance from the body of the probe, a baffle is used to limit the range of azimuth angles to 170°. This baffle is blackened to minimize reflection of skylight from the baffle to the diffuser. The range of zenith angles accepted by the baffle is from 5° (to avoid seeing the parachute overhead) to 88°. Measurements made with the optical axis of the instrument within 85° of the direction to the sun include both the diffuse and direct solar beam. A shadow bar ($\sim$10° wide) is mounted over the diffusing plate. Measurements made with the sun behind the shadow bar and again with the sun out from behind the bar permit separation of the direct and diffuse downward solar fluxes in the half of the upper hemisphere centered on the sun. An additional measurement is also made with the optical axis of the instrument directed 180° away from azimuth of the sun to give the portion of the downward diffuse flux coming from this half of the upper hemisphere.

For the measurements in the downward direction, other considerations become important. Because we want to study the reflection spectrum of distinct regions on the ground, spatial resolution is as important as the determination of the upward flux. We therefore chose to image the slit of the spectrometer on the ground and to

spread the light along the slit over 20 CCD pixels. Thus, we can spatially resolve 10 regions along the slit on the surface. The slit is bore sighted along the vertical axis of the field of the imagers to provide the morphological context of the spectrally measured regions. The slit is 4° wide and extends from 10° to 50° nadir angle. The 40° nadir angle range covering 20 CCD pixels gives 10 resolution elements each 4° square on the ground. The spectral intensities measured can be weighted with the cosines of the known nadir angles and integrated in nadir angle. At least 8 different evenly spaced azimuths are measured to permit an integration in azimuth for the upward flux. Thus, the optics and the sampling scheme permit integration of the spectral radiation field for the upward flux and also provide spatially resolved measurements of the spectral reflectivity of the surface.

Upward and downward spectra are obtained roughly every two km during the descent from 160 km to the surface. In the upward direction, the integration times for the measurements under the shadow bar are limited to insure that the measurements are completed while the diffuser is completely shaded. For downward-looking measurements, the integration times are limited so that the probe does not rotate more than 1.5 times the angular width of the spectrometer slit at a nadir angle of 30° (the center of the slit) during the integrations. The f/2 system permits S/N > 100 in a single spectral and spatial pixel for the downward-looking spectrometer. For the upward-looking measurements, 8 CCD detector pixels are combined along the length of the slit (which has no spatial resolution for the ULVS) to give similar S/N for the ULVS and DLVS.

3.3.3. *IR Spectrometer*

The IR spectrometer has two entrance paths, one viewing upward, and one viewing downward, in order to measure both the upward and downward fluxes. The ULIS has a diffuser as the entrance window (as for the ULVS), viewing about half the upward hemisphere. This allows the measurement of flux directly. The downward-looking input has a fused silica window and input lenses that define the field of view (FOV) at the entrance slit of the spectrometer. The input optics of these instruments transfer IR radiation through fiber optics to two aligned entrance slits placed one above the other perpendicular to the plane of dispersion of the grating. A shutter is installed just inside the input slits. An f/2 collimator lens assembly focuses the beams onto the transmission grating, and a camera lens assembly focuses the dispersed light onto the IR focal plane array. The IR spectrometer uses transmission gratings working in first order with achromatic lenses. A polarization compensator, consisting of a coated tilted plate, is included in the collimated beam in front of the grating to reduce sensitivity to the state of polarization of the incoming beam. Both the upward and downward-looking spectra are imaged directly on the two linear arrays of InGaAs detectors through a sapphire window with antireflection coating.

The optical field of view of ULIS is defined by the diffuser and external baffles and is 170 degrees in azimuth by 83 degrees in zenith angle (from 5 to 88 degrees

zenith). The spectrometer slit of DLIS maps into a 3° by 9° field of view (pixel footprint) with the center of the field of view 20° from the nadir.

In the case of the ULVS, the exposure time is sufficiently short that an adequate exposure is possible under the narrow shadow bar even when the probe is rotating at its maximum rate of 15 rpm. In the case of the ULIS, the total integration time is of the order of 60 s. Thus, no shadow bar is used to separate the direct and diffuse downward flux. Instead, measurements are accumulated in four azimuthal quadrants relative to the sun, and the shade provided by the probe itself is used to separate the direct and diffuse downward flux in the ULIS. For the DLIS, measurements are accumulated in 8 separate azimuthal regions relative to the sun.

In the normal mode of operation, the total time for data collection is an integral number of probe rotations, but is always constrained to be between one and three minutes. The time for data collection is estimated at the beginning of each cycle, and is updated during the cycle based on the data from the sun sensor after each rotation.

Within each azimuthal region, data are collected alternately with the shutter closed and with the shutter open. The process is symmetrical in time so that linear drifts in temperature (and hence dark current) are accounted for when the shutter-closed data are subtracted from the shutter-open data. The total shutter-open time is equal to the shutter-closed time. Within each azimuth region, the process begins and ends with the shutter closed for half the time used for the other open and closed intervals. Within each shutter-open or shutter-closed interval, the IR array can be read more than one time (depending on rotation period and temperature) to avoid saturation by the dark current. In addition, the shutter rate is kept at about 5 Hz so that temperature variations beyond linear drifts and their changes in dark current are adequately compensated.

3.3.4. *Solar Aureole Camera*

The solar aureole camera will measure the intensity of scattered sunlight over a range of scattering angles sensitive to particle size. Scattering at small angles (less than 40°, depending on particle size) is a good diagnostic of particle projected area. The forward scattering lobe becomes more strongly peaked at small scattering angles as the particle radius increases. The width of the forward scattering lobe does not depend strongly on particle shape for equal projected area particles, and it is insensitive to the particle refractive index.

Particle shape effects are much more pronounced at intermediate and large scattering angles, especially in polarization. The solar aureole camera will measure the vertical and horizontal polarization in the sunward and anti-sunward directions as the probe spins. These measurements will be performed at two wavelengths (500 and 935 nm) to provide sensitivity over a wide range of altitudes and particle size.

The angular sampling characteristics of the solar aureole camera are listed in Table 1. Measurements at small angular distance from the sun are made when the sun is behind the shadow bar, as viewed from the solar aureole camera window. The

solar zenith angle during descent is near 50°. In the sunward direction the camera covers scattering angles of 5°–25°. During the measurement in the anti-sun direction the scattering angle coverage is 75°–125°, on a 1° grid (see Figure 10). Each measurement samples the total column above the probe. The aureole contribution from a 2-km layer of the atmosphere is found by taking the difference between two measurements.

When measurements are collected near the sun, the shadow bar prevents direct sunlight from striking the Solar Aureole window assembly. A beam splitter is used to provide input from a calibration lamp. Calibrations are performed every six months during the cruise to Titan and four times during the descent. They are made in such a way that the signal from the atmosphere can be subtracted from the total signal.

A telecentric micro-lens design provides wide angular coverage at f/2 for the solar aureole system. The polarizers used for the visible and near IR channels are quite pure; the polarization they impart to unpolarized light is within a few percent of 100%. The degree of polarization can be obtained from the measurements if the direction of the polarization vector is assumed to be known. For the small particles expected in the atmosphere of Titan, the polarization is expected to be perpendicular to the scattering plane near 90° scattering angle, so the degree of polarization in the scan made at scattering angles between about 75° and 125° will be known. Optical fiber ribbons are located at the foci of the camera lenses. They merge with fiber ribbons from the other visible optical elements to feed the focal plane as shown in Figure 8.

The use of solar aureole measurements to retrieve particle size distributions is well known, and several retrieval algorithms have been described in the literature (see, e.g. Dave, 1971; Nakajima *et al.*, 1983). Accurate retrievals require a high signal/noise ratio. The solar aureole camera was designed to achieve S/N $>$ 100.

The 6° $\times$ 50° solar aureole field-of-view maps onto a 6 $\times$ 50 pixel area of the CCD. Calculations show that S/N will be $>$100 provided that 6 pixels are summed. Pixel summing will be performed during data analysis by summing pixels along arcs with constant angular distance from the sun. In this way no angular resolution will be lost to pixel summing. The expected S/N varies from $\sim$100 to $\sim$900 depending on wavelength, altitude, solar zenith angle and azimuth during the measurement interval between 160 km altitude and the surface.

3.3.5. *Violet Photometers*

The purpose of the violet photometers is to extend the spectral range of the measurements to 350 nm from the short wavelength limit of 480 nm of the visible spectrometers. Because no sharp spectral features are expected in this spectrum, a single spectral channel is used. In this spectral region, the spectrum of the incident sunlight is modified by the absorbing properties of the small photochemical aerosols in Titan's stratosphere. These particles absorb more and more of the short wavelength end of the spectrum with increasing depth into the atmosphere. Hence,

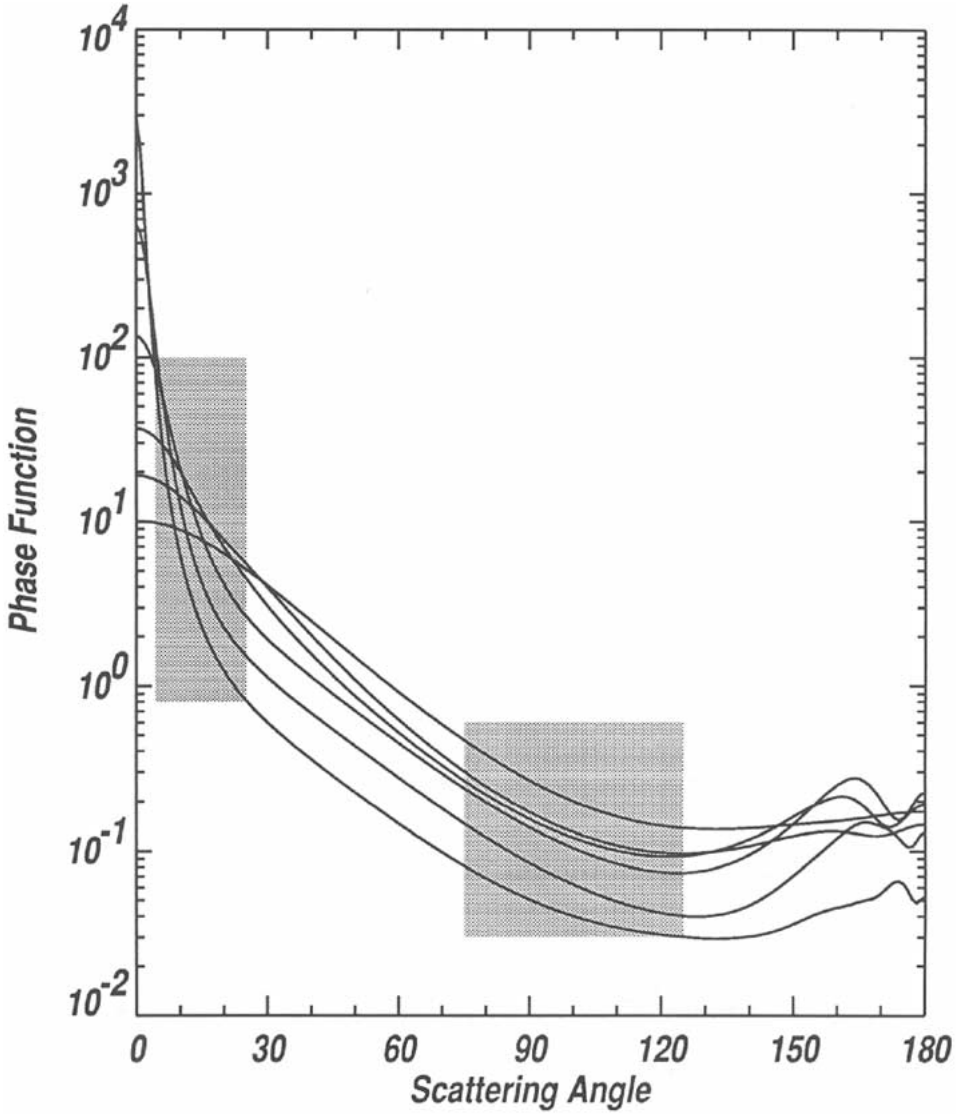

Figure 10. The solar aureole camera samples the scattering angle ranges shown by the shaded regions, for a solar zenith angle of 50 degrees. Also shown are phase function curves for spheres having a log-normal size distribution with mode radii ranging from 0.0625 to 2 microns doubling each time, at a wavelength of 0.5 microns. The smallest particles have the smallest forward-scattering peak.

in order to measure the energy deposition, it is important to filter the response of the detectors to make them relatively spectrally flat so that the violet measurements can be converted to absorbed energy independent of assumptions regarding the spectrum of the light measured. The product of the spectral response of the violet

detectors and the transmission of the violet filters is spectrally flat to about ±15% from 350 to 480 nm for these measurements.

The Upward-Looking Violet (ULV) photometer shares the diffuser of the ULVS system, and the field of view of the ULV is identical to that of the ULVS. The shadow bar permits separation of the direct and diffuse downward flux in the violet in the same way as for the ULVS, and the sampling in azimuth is the same for the ULV and the ULVS systems. The DLV uses exactly the same baffle and diffuser design mounted on the bottom of the sensor head to measure the upward violet flux, but without the shadow bar. The sampling in azimuth of the DLV is limited to two regions, near the azimuth of the sun and near 180° from the sun. These two measurements sum to give the total upward violet flux.

For the sake of simplicity, the electronics for the ULV/DLV systems use the same 12-bit A/D converter used for several other housekeeping functions including voltage and temperature monitoring. The light level in the upward-looking violet channel at the top of the atmosphere is known from the solar spectrum. A single gain with a fixed time constant is used in the ULV system with no provision for gain change or change in integration time in flight. The gain is adjusted when the instrument is built so that the sum of the signal from the inflight calibration signal and the downward solar flux at Titan occupy between half and three quarters of the 4096 available digital steps. The signal from the inflight calibration system is adjusted to be roughly equal to the signal expected from the sun at the start of the descent. This gives about 1000 digital steps for the violet signal at the start of the descent. The random noise in the ULV channel is comparable to the size of a digital step. The gain of the DLV system is larger by about a factor of ten than that of the ULV system to account for the lower expected signal looking down on Titan. We can measure the absorption of the violet energy in the bandpass of the violet photometers during the descent to a few tenths of a percent of the downward flux at entry.

3.3.6. *Sun Sensor*

The timing of all of the upward-looking DISR measurements requires precise knowledge of the solar azimuth angle. To satisfy this need a sun sensor is located beside the shadow bar. The field of view of the sensor is a 64° cone centered 47° from the zenith. The sun sensor consists of a window, a lens system, a filter, a reticule containing three slits, a pair of lenses to focus the light on a silicon photodiode detector, and its associated readout electronics. As the sun crosses the field of view, three large pulses are seen as the sun's image passes through the three slits of the reticule. The time of the maximum signal in the center slit defines the azimuth of the sun. The first and third slits are not parallel to the center slit, but converge to permit determination of the zenith angle of the sun. The times of all three slit crossings are transmitted in housekeeping. The time between the first and third slit crossing compared to the times between successive crossings of the center slit (the

rotation period) gives the angle between the spin axis of the probe and the vector toward the sun.

In addition, the brightness of the central pulse in each rotation past the sun is included in the telemetry to give a measure of the direct solar beam at the wavelength of the sun sensor system (939 nm) as a function of altitude. The sun sensor is designed to track the direct solar beam down to 1/1000 of its brightness outside Titan's atmosphere. At the nominal solar zenith angle of 50°, the sun signal would be lost at a vertical extinction optical depth of 4.4. This compares to a vertical optical depth of less than about 1 in some current models of Titan at the wavelength of the sun sensor.

The sun sensor uses several logic tests on the relative timing of the series of three pulses on successive rotations to distinguish pulses due to the sun from variations in intensity that might be due to diffuse clouds above the probe. If the probe falls beneath a thick cloud and loses lock, the internal rotation rate transmitted by the probe spin sensor is used to time DISR data collection. The DISR sun sensor continues to look for the sun after losing lock, and will find the sun if it reappears from behind a passing cloud.

3.3.7. *Surface Science Lamp*

The purpose of the surface science lamp (SSL) is to illuminate the surface of Titan in spectral regions where strong atmospheric absorption bands prevent sunlight from penetrating to Titan's surface. The SSL permits continuous measurements of the spectral reflectivity of the surface to be made throughout the entire spectral range. The SSL is a 20 Watt lamp with a parabolic reflector which illuminates the surface and fills the narrow 3×9 degrees FOV of the IR spectrometer with enough light to give a S/N of 50 at 60 m altitude within the strong methane bands even if the surface reflectivity is as low as 0.05.

The lamp system is activated when an altitude of 700 meters is reached (given by the radar altimeter) and is operated during the last several minutes of the descent where a continuous sampling of the reflection spectrum of the surface is obtained using both the DLVS and DLIS.

3.4. Internal Calibration System

Almost all of the science goals of the DISR experiment require measurements to be made on an absolute photometric scale. This is difficult enough for a single optical system and detector, let alone for a system as complex as DISR. The measurements of the apparent brightness of the sun at high altitude near the start of the descent at continuum infrared wavelengths is expected to be relatively unaffected by atmospheric scattering and absorption, and so can provide an important check on the absolute calibration of this one DISR optical system. The ability to tie all the various DISR systems together on a single photometric scale is provided by the internal calibration system built into the DISR sensor head.

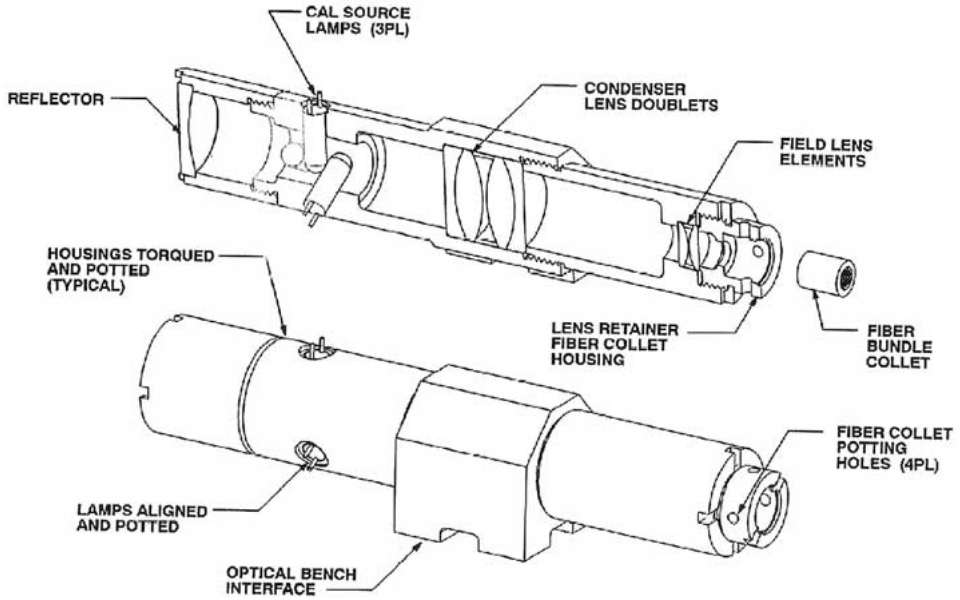

Figure 11. The assembly that collects light from the three redundant 1-watt lamps and illuminates the bundle of fibers that carry the light to the input end of each of the DISR sub-instruments.

The internal calibration system consists of a set of three redundant 1-watt lamps which illuminate one end of a bundle of thick quartz fibers (see Figure 11). Each of these fibers carries some light from the calibration lamps to the first optical element in each of the other DISR optical systems. This light is reflected from either the inside of the window for that system or from a small reflector mounted on the back of the window and passes through the rest of that optical system to the detector. The fraction of the light from the calibration lamps carried to the input of each DISR measuring sub-instrument is carefully measured before launch, and is expected to remain constant through the mission. We should be able to track changes in the sensitivity of detector pixels, in the transmission of the imaging fiber optic conduit, or in other optical elements during the cruise by monitoring the relative outputs of each DISR system to the light provided by the internal calibration system.

It is important to emphasize that we are not relying on the stability of the absolute output of the lamps of the internal calibration system, only on the stability of the relative fraction of the light carried to each DISR subsystem by the thick quartz fibers of the calibration system. These quartz fibers are not expected to be susceptible to darkening by energetic particle bombardment. Thus, the changes in the relative output of the different DISR optical pixels can be tracked with time after launch and even measured at several times during the Titan entry.

There are no moving parts in the internal calibration system, so the light from this system is added to the light from the ambient Titan atmosphere during the descent. The light from the calibration system is designed to exceed by a large

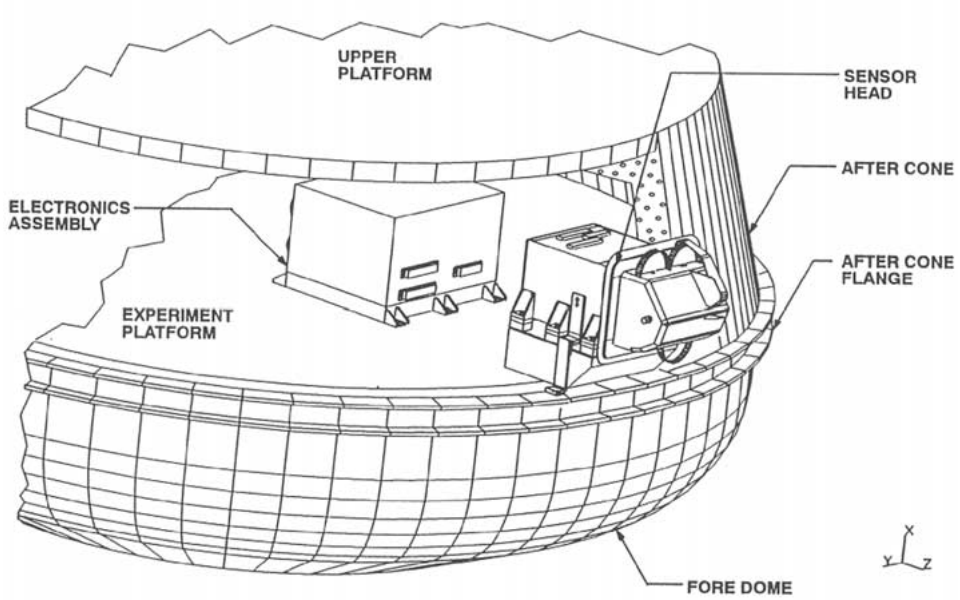

Figure 12. The arrangement of the Electronics Assembly and the Sensor Head on the instrument shelf of the Huygens Probe.

factor the light from the ambient atmosphere. In addition, we have designed the internal calibration procedures to collect light with the calibration lamps on, then off, and then on again at the same azimuth to permit accurate subtraction of the ambient signal from the signal provided by the calibration system. The calibration light levels are adequate to make measurements with S/N better than the target value of 100 even after subtraction of the portion of the signal due to the ambient atmosphere.

3.5. MECHANICAL DESIGN

The DISR instrument consists of two packages, the sensor head (SH) and the electronics assembly (EA) mounted to the top of the instrument shelf in the Huygens Probe. The sensor head is mounted on a metal bracket above the top surface of the instrument shelf and sufficiently far outboard so that the front of the SH protrudes out through the back side of the probe. This permits clear views from the zenith to the nadir and in directions to $\pm 85^\circ$ in azimuth from the radial direction. (See Figure 12.)

The EA (see Figure 13) is a box containing six boards mounted horizontally above the power supply which is built into the chassis base. The six boards include the CCD drive board provided by MPAE, the data compression board provided by TUB, the IR detector system drive board provided by the PO, and the digital board, the CPU board, and the auxiliary board provided by LMA. The mass of the EA is

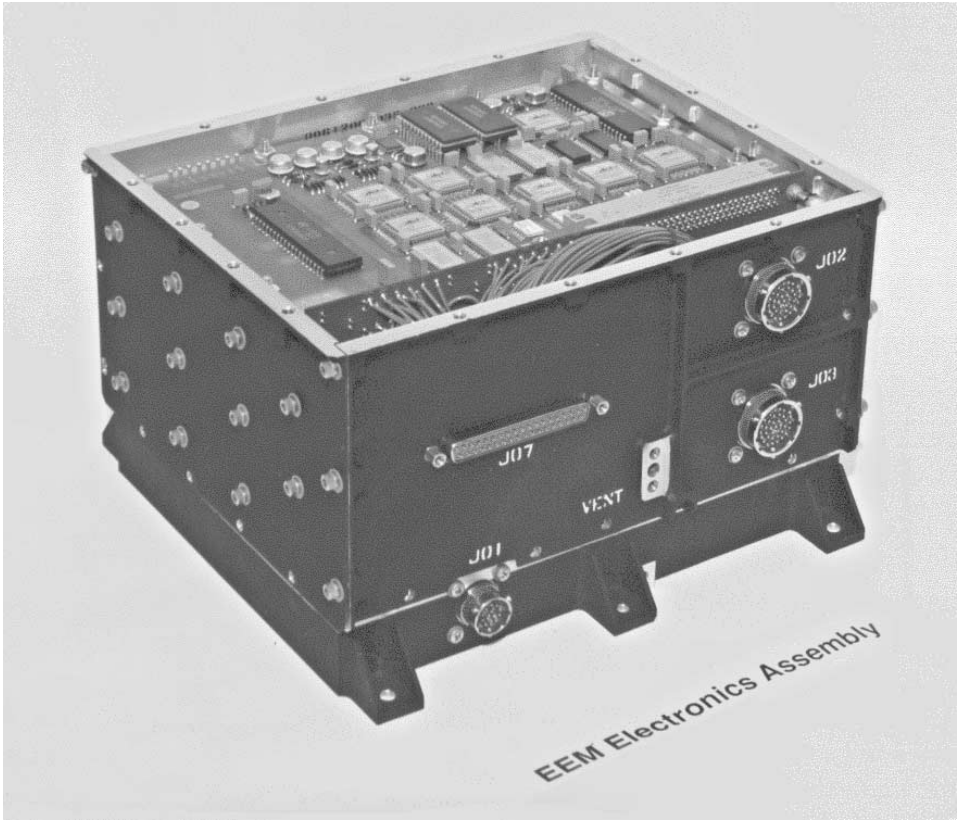

Figure 13. The Electronics Assembly box with the lid removed showing the Data Compressor board at the top of the stack of electronics boards.

4.4 kg including radiation shielding on particular electronic parts. The six boards are an integral part of the structure and are bolted to the chassis side and back walls.

The mechanical design of the sensor head is shown in Figure 14. The SH assembly holds the detectors, fiber optics, foreoptics for the visible and infrared spectrometers, the three imaging cameras, the solar aureole camera, the internal calibration system, and the surface science lamp all in precise alignment over a temperature range of some 150 °C, for ten years, and throughout the vibration and shock environment of the mission. In addition, the thermal environment of the detectors is controlled during the descent and the detectors are protected from the energetic particle environment during the mission.

The sensor head has a CCD detector side and an IR side. The face of the CCD is held 20 μm away from the end of the fiber optic conduit that delivers light from the three imagers, the solar aureole input assembly, and the visible spectrometers. This conduit and its face that mates to the CCD are shown in Figure 15. The CCD half of the sensor head including the detector, fiber optic conduit, imager lens assemblies, solar aureole assembly, and the visible spectrometer is shown in Figure 16.

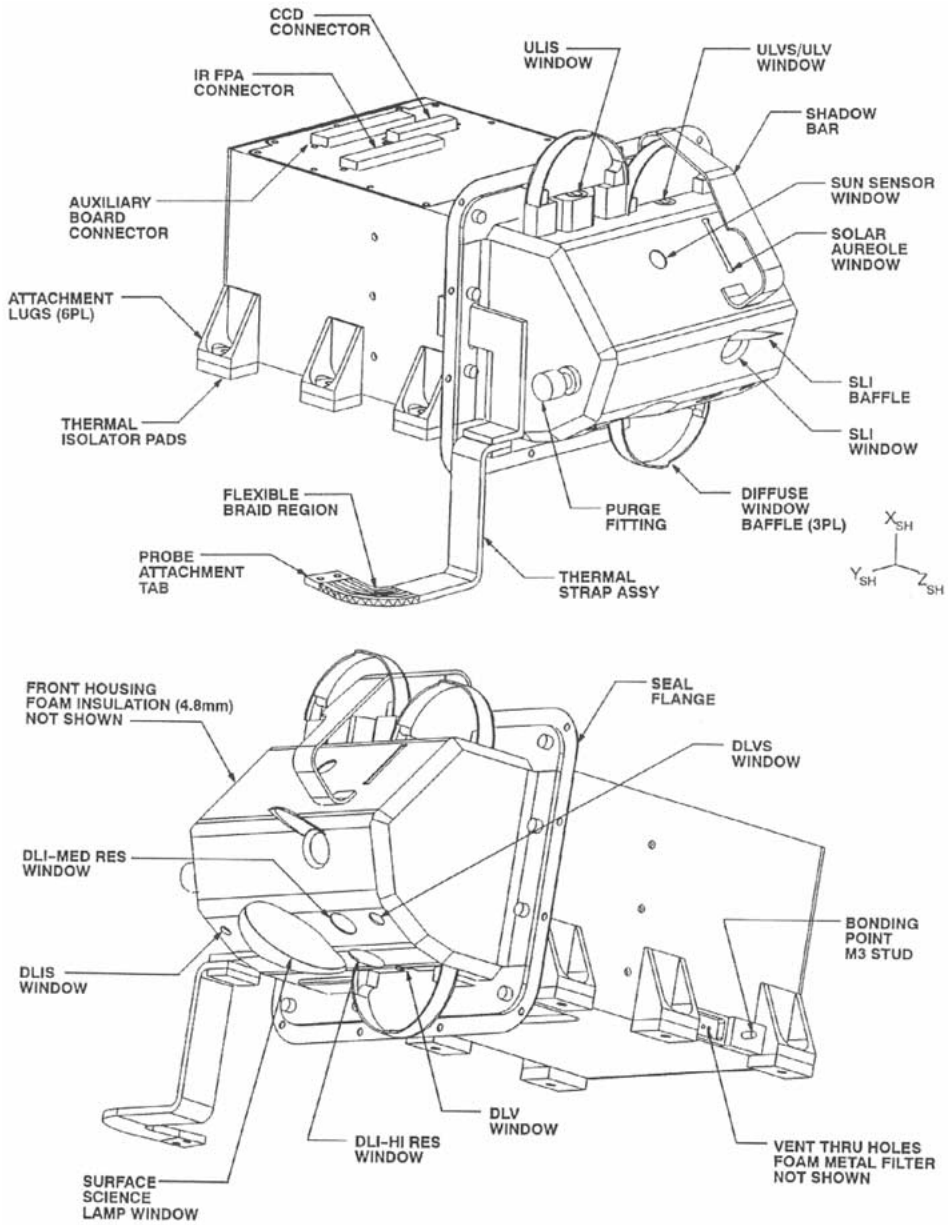

Figure 14. The Sensor Head as seen from above and from below.

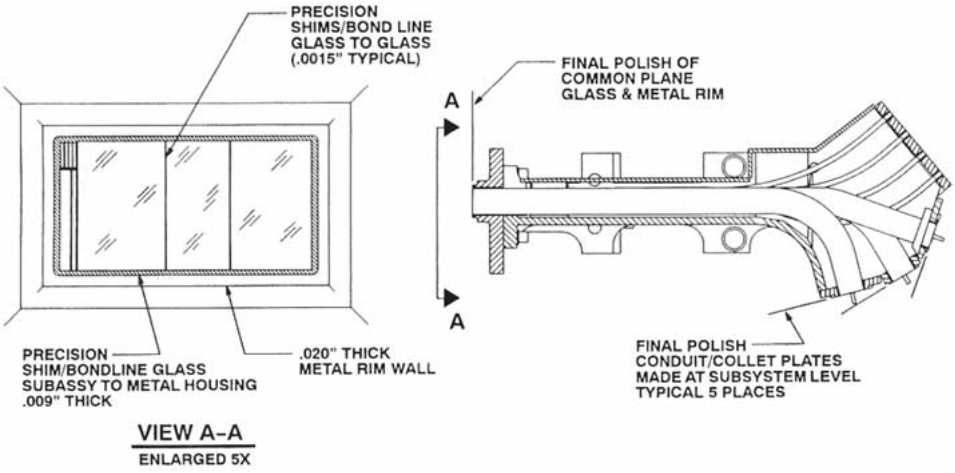

Figure 15. The fiber optic conduit including the end view that mates with the CCD detector.

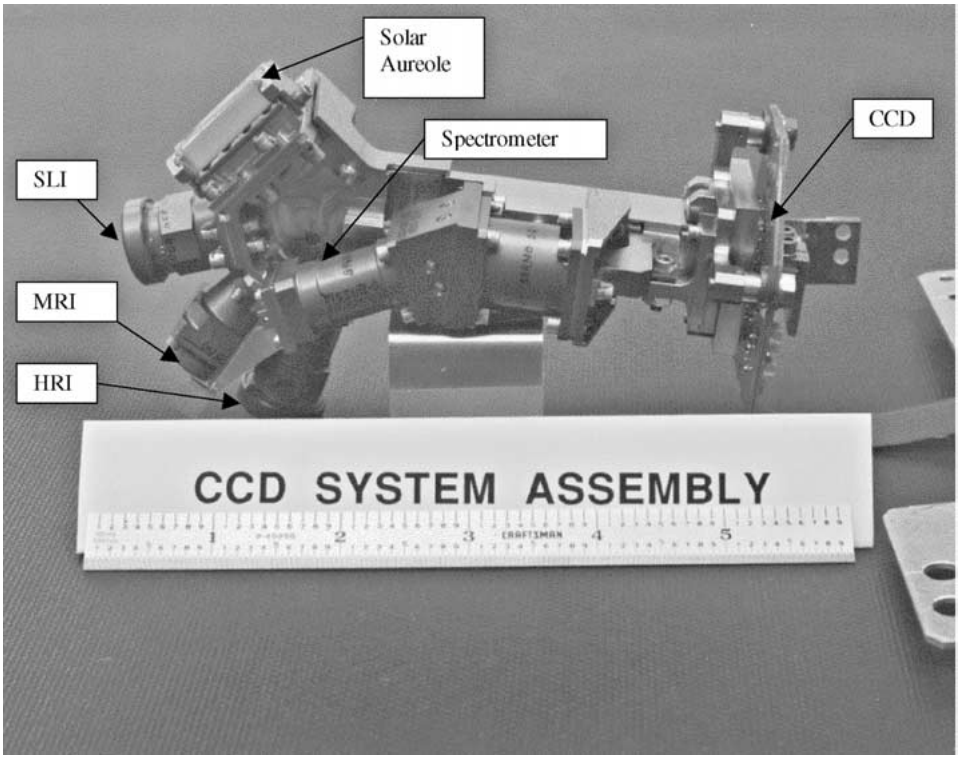

Figure 16. The CCD mated to the fiber optic conduit, the three imager lens assemblies, the solar aureole input lens assembly, and the visible spectrometer.

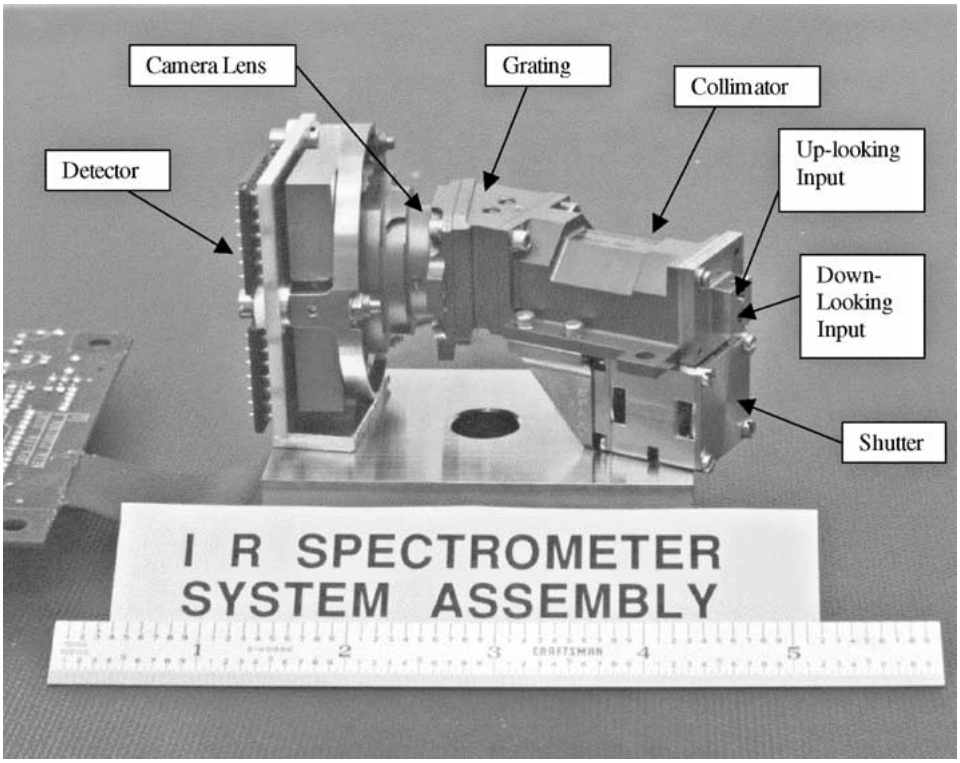

Figure 17. The IR detector mounted to the IR spectrometer, the shutter, and the input fiber collet assembly.

The IR half of the sensor head begins with the pair of IR array detectors and their preamp board. This detector is mounted to the IR spectrometer, the shutter, and the fiber input assembly as shown in Figure 17.

The two detector assemblies are surrounded by a tungsten radiation shield 4 mm thick, sufficient to prevent protons with energies <64 MeV from reaching the detectors and significantly reducing the radiation dose experienced by the detectors. The mass of this radiation shield is 1 kg out of the total mass of the SH of about 3 kg.

The optical systems are securely mounted to a titanium optical bench which is secured to the base of the sensor head housing using a ball joint and two slip joints. This optical bench provides the means of tying all the optical systems together to the detectors. Figure 18 shows how the optical bench assembly fits into the sensor head box. Figures 19 and 20 show the optics assemblies after insertion into the main sensor head box. These views show the Surface Science Lamp, the Sun Sensor, the three imager lenses, the visible spectrometer, and the input optics assemblies for the Solar Aureole system and for the visible and IR spectrometers. Several calibration fibers used to bring light to the input optics are also visible.

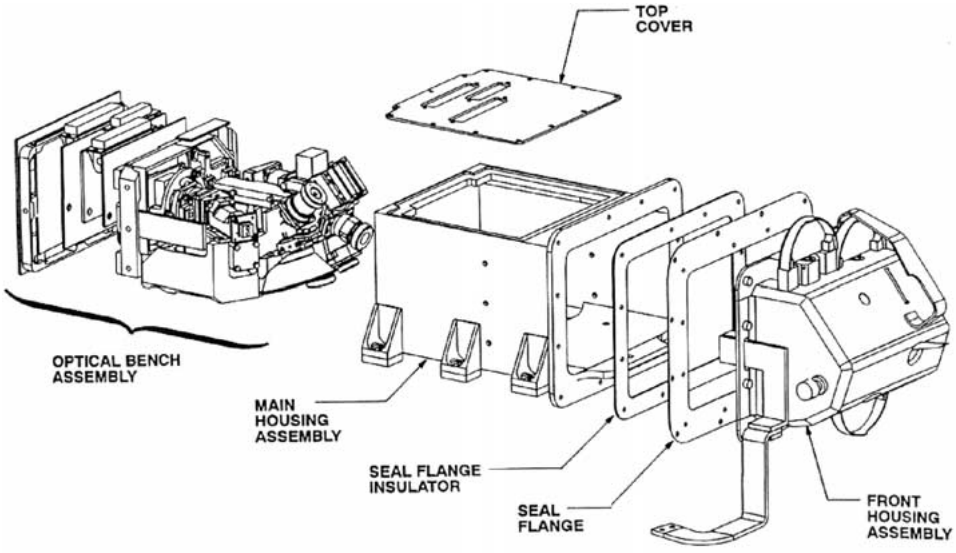

Figure 18. The optical bench assembly and how it fits into the sensor head package.

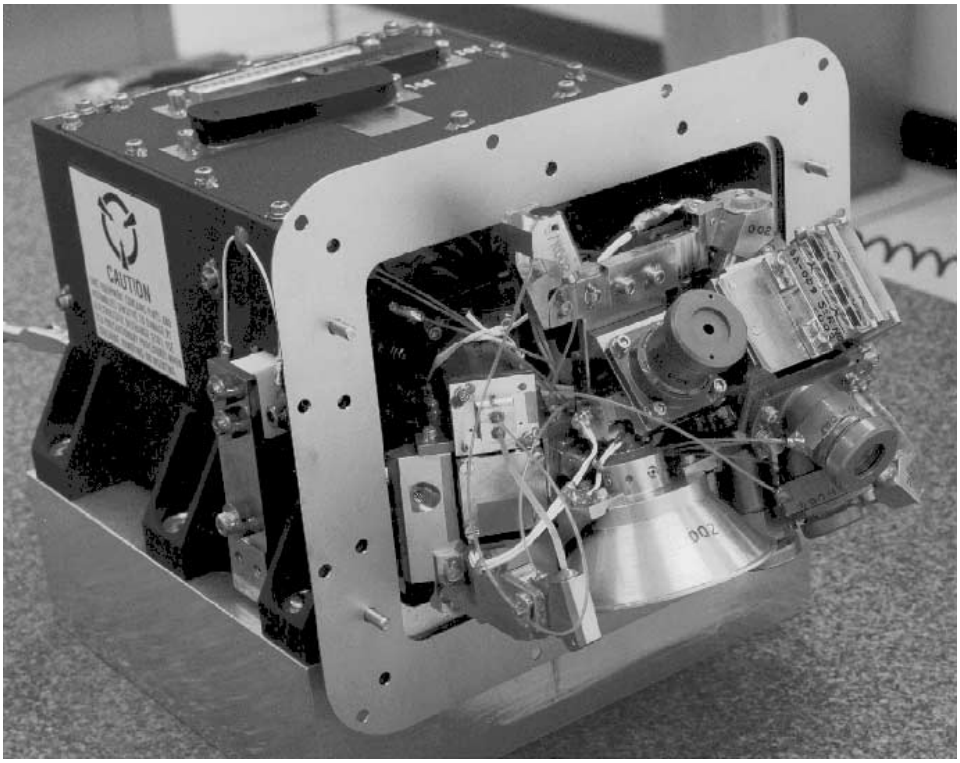

Figure 19. The optics after insertion into the main sensor head box.

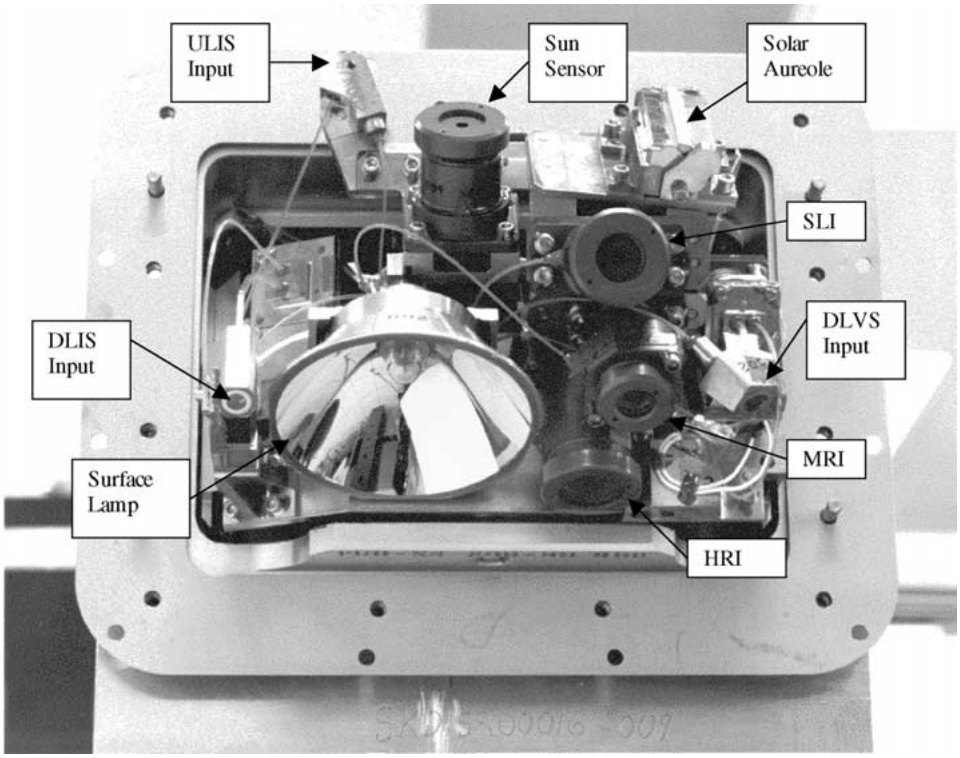

Figure 20. The sensor head before the front housing is installed. The Sun Sensor, Surface Science Lamp, imager lenses, and inputs to the DLIS and DLVS are visible along with some of the calibration fibers bringing light to the input optics.

The DISR thermal design must maintain interface constraints, cool and maintain the detectors' temperature within limits, maintain all other components within their temperature limits and minimize mass and power. In particular, it is important that the detectors are cooled as rapidly as possible from their temperatures near 260 K at Titan entry to temperatures below some 220 K to minimize the influence of dark current and to ameliorate the defects in CCD pixels that may have been damaged by energetic particle impact during cruise.

The detector cooling system includes a thermal strap to provide a heat sink to the atmosphere via an attachment to the probe. A heater ensures that the detectors will remain above their minimum temperature limit. The heater is thermostatically controlled to maintain the temperature of the detectors above 160 K. The coupling to the housing and masses of the detector components are minimized to allow a rapid cooldown. The temperatures of the PC boards in the sensor head are maintained with a second electronic thermostatically controlled heater.

The sensor head housing is constructed of aluminum to provide thermal coupling between the interior and the exterior. This will maintain the exposed windows well above the ambient atmospheric temperature. The exposed portion of the hous-

ing is covered with a low density insulation and is coated with a conductive paint. The interior housing is conductively isolated from the probe but radiatively and convectively coupled to the probe. This method allows the probe to provide some heating of the sensor head 'warm' components. The sensor head front housing is thermally isolated from the rear housing.

3.6. Compression of imaging data

Imaging data are compressed on board before transmission in order to achieve a balance between the number and the quality of images received. The images (digitized at 12 bits/pixel) are first divided by an onboard flat field to eliminate artifacts introduced by variations in the transmission of the fiber optic conduit. The data are then reduced from 12 to 8 bits/pixel using a square root software algorithm. The data are then passed to a lossy hardware data system for further compression.

For most test scenes, the image distortions are relatively small for an additional compression by a factor up to 8 using a standardized JPEG compression scheme. An implementation of such a compression by software running on the main processor would limit the image cycle time to more than 1 minute. Therefore, a dedicated hardware coprocessor has been developed which performs a complete compression of a 256×256 pixel image within less than 130 msec at low power and for light weight. The coprocessor is designed around an STV3200 DCT chip, an 80C86 microprocessor and 8 ACTEL FPGAs. The compression algorithm running on this dedicated coprocessor deviates in some aspects from the JPEG scheme in order to decrease power and mass and enhance the robustness against transmission errors. The SNR (in the image intensities) of the modified hardware implementation is <1 dB below the values achievable with standard JPEG. On simulated low contrast images as expected for Titan, the noise is increased above shot noise by factors of only some 1.7 and 2.5 for compression ratios of 3:1 and 6:1. For well exposed images, features with a contrast as low as 1% are seen in images compressed by as much as 6:1 by the lossy compressor.

3.7. Electronics

The electrical block diagram of the entire DISR instrument is shown in Figure 21. The left-hand portion of the diagram shows electronics which are in the sensor head, while the right-hand section indicates the electronics housed in the electronics assembly package. The SH contains three small boards: one provided by MPAE contains the preamps for the CCD; one provided by PO contains the preamp for the IR detector; and the third, provided by LMA, provides preamps for the Sun Sensor and its test Light Emitting Diode as well as the violet detectors of the ULV and DLV instruments. The European Co-Is also provide the three shaded boards as shown in the EA: the driver provided by MPAE for the CCD; the driver for the IR detector provided by PO; and the hardware Data Compression System (DCS) provided by TUB.

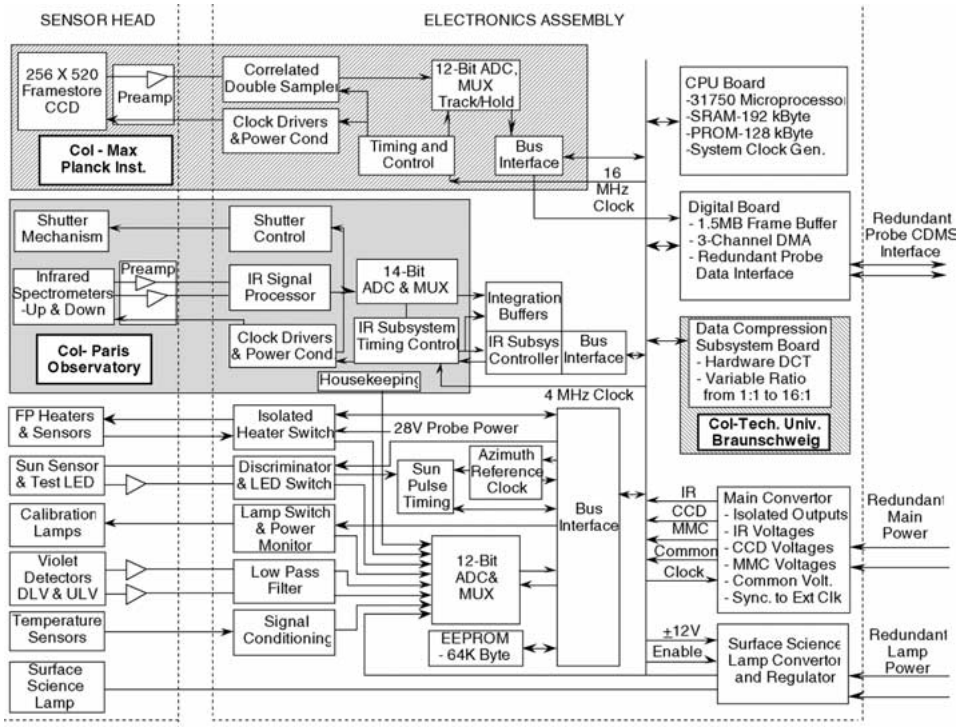

Figure 21. Block diagram of the electronics on the six boards in the Electronics Assembly. The three cards provided by the European Co-Is are shown shaded, and the functions contained on the CPU Board, the Digital Board, and the Auxiliary Board provided by LMA are shown.

The CPU board provides radiation-hard critical Random Access Memory (RAM) in 128 k bytes of program RAM and an additional 64 k bytes of data RAM. It also holds 128 k bytes of Programmable Read Only Memory (PROM) and a separate block of 64 k bytes of EEPROM which can be changed by commanded uploads. The microprocessor is a MA31750 running at a clock speed of 12 MHz capable of some 1.6 million instructions per second (MIPS). Some 1.2 MIPS are required for operation of the DISR as planned. A watchdog timer is provided with a 100 Hz clock at 16-bit resolution.

The Digital Board contains a large (1.5 Mbyte) frame buffer of static RAM accessible by the CPU or by any of three Data Management Assembly (DMA) channels. Every 10 seconds the entire frame buffer will be refreshed by CPU block read/write routine using a full Error Detection And Correction (EDAC) function provided by a single Harris Semiconductor chip.

Three programmable DMA channels are provided using Actel 1020 Field Programmable Gate Arrays (FPGA). The mode, word count, source, and destination addresses are all programmable.

The Probe interface provides dual telemetry packet channels for transmission of the science data. It provides dual Memory Load Command channels to receive

the data and/or commands from the Probe. Dual serial status channels are also provided to transmit a 16-bit housekeeping status word to the probe upon request. Redundant channels are also provided to receive the Probe Data Broadcast data such as spin rate, time, and altitude. This interface provides a means of receiving an indication of which telemetry channel is to be used for commanding the DISR.

The Auxiliary Board contains the digital interface to the IR detector system. It also contains several analog circuits to condition signals from the ULV, DLV, Sun Sensor, the Inflight Calibration System; to control the focal plane and SH electronics card heaters; and to monitor temperatures, lamp currents, and other housekeeping data in the instrument. A multiplexer and 12-bit A/D converter is used on the Auxiliary Board for this purpose.

3.8. Software and data collection modes

The DISR flight software was developed using an object-oriented design in the Ada language. The software uses a re-entrant event dispatcher to control execution based on the priorities of events occurring in both the hardware and software. Multi-tasking is not used. Hardware interrupts are used to provide services for the probe interface, the sun sensor, a general purpose event timer, the telemetry channels, the direct memory access controllers, the CCD, the IR detector, and the hardware data compressor.

The software controls the calibration and surface science lamps. The calibration lamps are turned on during appropriate parts of calibration cycles.

All commands to the DISR are processed by the software. Only six commands exist, although some have a variety of parameters.

1. A receipt-enable telecommand must begin a commanding session. This command is used to protect against spurious commands.
2. A change-mode telecommand may be used to change the operating mode of the DISR into descent mode (the default mode), into calibration mode, into single telecommand mode, or into memory access mode.
3. Single measurement telecommands direct the instrument to perform one or more repetitions of a particular measurement. These commands are useful during instrument calibration and test.
4. Single test telecommands are similar to single measurement telecommands, except they initiate preprogrammed test sequences on the specific portions of the hardware including the IR shutter, hardware data compressor, heaters, and lamps.
5. Memory upload commands are used in memory access mode to store new tables which are read by the software. These table entrys include bad pixel maps, square root compression tables, and parameters that control measurement scheduling and processing.
6. Memory dump telecommands can transfer any portion of DISR memory into telemetry for verification.

The software also coordinates and controls all data collection. Optimum exposure times are computed for each subinstrument using the CCD and IR detectors. These times are based on the data number population histograms of the most recent previous exposure of the same type. The exposure time can also be limited by the amount of smear caused by the spin of the probe.

On-board data processing functions also include several miscellaneous functions. Adjacent columns of pixels may be summed within the same instrument field of view. Data for the hardware data compressor must be reformatted before it is fed to the compressor. Lossless compression is done entirely in software. Bad pixels are eliminated according to a bad pixel map which is stored in EEPROM. Data from the imagers are also reduced from 12 bits to 8 bits before being fed to the hardware data compressor. This reduction is done using a table lookup which performs a pseudo-square root transformation of the raw data. A watchdog timer can reset the microprocessor if it times out. The software that builds telemetry packets periodically resets the watchdog timer. If telemetry is not being produced, the processor will be reset and execution will be restarted.

Calibration and instrument health data are collected at six-month intervals during the cruise. At each opportunity one of five possible activities may be performed. The Health Check sequence exercises each software controlled function to test for normal operation. The In-Flight Calibration sequence is used to obtain relative response and measure the noise level of the detectors. The Simulated Descent uses parameters loaded into special tables to test descent sequencing. Two types of activities are available for contingencies. Single Measurement and Single Test commands can be used to diagnose problems with specific instrument subsystems. Finally, memory dumps and uploads can be used to verify the contents or memory and to upload new table values to correct for instrument subsystem malfunctions.

One of the more interesting aspects of the software is the way it schedules collection of related data from various subinstruments in an optimized way. During descent, data collection is divided into cycles which form a coordinated set of measurements within a limited time span. Several different types of cycles are used to meet the differing needs of data collection during different parts of the descent. The software uses information from the probe, including the altitude, time, and spin rate, to decide which type of cycle to start next. The cycle choice also depends on the amount of buffer space available within the DISR and on the current probe telemetry rate. The software chooses a cycle type which will gather sufficient data to keep the instrument from running out of telemetry packets, yet it must also choose a cycle type which will not provide so much data that it overfills the available buffer space.

Differing requirements are placed on the data buffering scheme depending on how close the probe is to the surface. Normally data can be gathered much faster than they can be telemetered. If the probe is still high enough to allow sufficient time for telemetry before impact, data may be profitably buffered, allowing the buffer to fill further as each cycle passes. On the other hand, if the probe is near the

surface, each data set should be telemetered as soon as it is complete to prevent the probe from hitting the surface with substantial amounts of data still in the buffer.

Early in the descent the probe is falling rapidly. It is important to measure quantities such as the solar flux deposition and solar aureole profile within vertical intervals which are small compared to the atmospheric scale height. Cycles high in the atmosphere are driven by a cycle duration constraint, even if many cycles are in the buffer a long time before they are telemetered. However, at some altitude it is important to start each new cycle with almost nothing in the buffer. The most recent, lowest altitude data will be transmitted immediately if the buffer is in this state.

We use both of these scheduling algorithms during the descent. Above 20 km altitude, we use duration-constrained scheduling. At 20 km, we pause to permit all previously buffered data to be telemetered. After this, new cycles are only begun when the telemtery buffer is nearly empty.

Within data cycles, it is usually important to schedule measurements at particular azimuths. Images, for example, must be scheduled to occur at 12 equally spaced azimuths to provide data for a mosaic. The software determines the azimuth at the beginning of each cycle and predicts its change with time during the cycle using a quadratic extrapolation. As new information about the spin rate becomes available from the sun sensor, these predictions are updated during the cycle and the following measurements are scheduled using the revised predictions.

4. Measured Quantities

The altitudes and times during the descent where various types of cycles are gathered are shown in Figure 22. The instrument is turned on near 170 km altitude. In order to fill the initially empty telemetry buffer as rapidly as possible, the instrument begins with a data collection cycle which contains an image panorama. The data collected in cycles which contain image panoramas are shown in Table 2. Note that on alternate cycles of this type, the azimuths of the images are offset by 15°, half the width of the images. These cycles contain a full set of spectral data (with downward looking visible spectra in the center of each of the images) and solar aureole data as well. Above 20 km, these cycles are constrained to collect all their data in between 1.5 and 4.5 minutes.

Above 20 km altitude, a non-imaging cycle is chosen as the next cycle if the DISR telemetry buffer contains data that will take more than four additional minutes to transmit. Non-imaging cycles are interleaved between imaging cycles to produce spectral measurements at higher vertical resolution than would be possible if all cycles contained image panoramas. The time for data collection in non-imaging cycles is limited to between 1.5 and 3 minutes. The maximum cycle duration prevents long gaps between observations which might occur at very slow probe rotation rates where a cycle might take a very long time to complete. The minimum

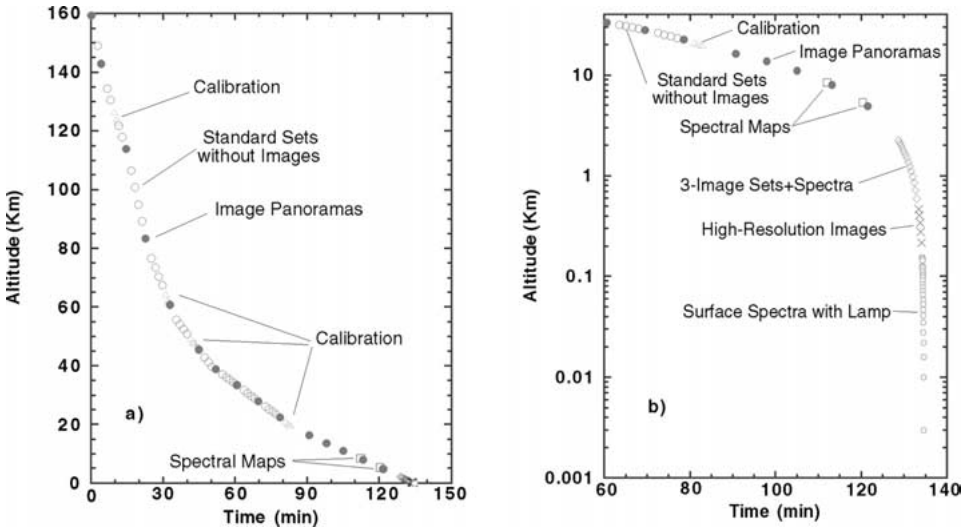

Figure 22. Vertical profile of various types of data sets obtained during Titan entry. The variation throughout the entry is shown in (a), and the variation at low altitude is emphasized in (b).

TABLE 2
Image cycle measurements

Subinstrument	Azimuths
Solar Aureole	1.5° (under the shadow bar), 174°
ULVS and ULV	5.5° (under the shadow bar), 140°, 180°, 320°, 338°
HRI, MRI, SLI, and DLVS	2°, 32°, 62°, 92°, 122°, 152°, 182°, 212°, 242°, 272°, 302°, 332° or 17°, 47°, 77°, 107°, 137°, 167°, 197°, 227°, 257°, 287°, 317°, 347°
Dark current	180°
ULIS	315°–45°, 290°–315°and 45°–70°, 90°–135°and 225°–270°, 135°–225°
DLIS	0°–45°, 45°–70°, 90°–135°, 135°–180°, 180°–225°, 225°–270°, 290°–315°, 315°–360°
DLV	0°, 180°

cycle time forces the scheduler to wait before the beginning of the next cycle and is used to tune the relative numbers of imaging and non-imaging cycles. Increasing the minimum cycle duration allows the telemetry buffer to be emptied further during the cycle, and increases the likelihood that an imaging cycle will be chosen next.

The standard non-imaging cycle differs from the imaging cycle in three respects: (1) 6 (rather than 12) DLVS spectra are obtained evenly distributed in

azimuth beginning 20° from the sun; (2) no HRI or MRI images are obtained; and (3) six SLI images are obtained evenly distributed in azimuth beginning 15° from the azimuth of the sun. The SLI data in 2 13-column wide regions are summed to two columns of brightness as a function of zenith angle, losslessly compressed, and included in the telemetry stream. The location of the horizon can be determined in each of these six azimuths relative to the sun on non-imaging cycles. These data, together with the full SLI images on imaging cycles, constrain the attitude of the probe during every measurement cycle.

Special calibration cycles are performed four times above 20 km at roughly equally spaced detector temperatures. These data use the on-board calibration lamps to provide signals which dominate those from Titan. These cycles provide relative calibrations of the upward and downward looking subinstruments as well as corroboration of the flat field properties of the CCD and IR detectors. A special long exposure measurement is also made with the IR subinstrument while the shutter is closed to accurately determine the dark current generation rate for each pixel.

At 20 km altitude a special 'pause' cycle occurs in order to empty the telemetry buffer. Imaging cycles are then gathered between 20 km and 3 km, with each new cycle beginning only when the telemetry buffer drains to a preset low level. This sequence is interrupted twice (near 9 and 4 km altitude) for the Spectrophotometric Cycles when downward-looking spectra are obtained as rapidly as possible for one probe rotation. These data map the spectral reflectance of the surface at high spatial resolution.

If normal image cycles were continued below 3 km altitude, telemetry of the data would not be completed before impact with the surface. Therefore, between about 3 km and 500 m special cycles are used in which a set of HRI, MRI, SLI images, spectra, and solar aureole measurements are obtained as rapidly as the telemetry rate permits regardless of the azimuth. (See Figure 22b).

Between 500 m and 250 m, single HRI images are obtained as rapidly as the telemetry rate permits (about every eight seconds). Single HRI images and dark current measurements are the only data collected in this altitude interval. In the last image near 250 m the scale will be about 25 cm/pixel.

The surface science lamp is turned on at an altitude of 700 m. For the final 250 m of the descent we obtain only DLV, DLVS, and DLIS measurements. Some 19 spectra are obtained with the Surface Science Lamp turned on. These yield continuous reflection spectra of the surface over the spectral range of the DLIS for constraining the composition of the surface. As the probe continues to rotate slowly while these exposures are collected, each will view a different region on the surface. Two of the 20 pixels along the DLVS slit will be illuminated by the SSL, and these will permit the DLIS spectra to be extended to shorter wavelengths. The S/N of these spectra increase as $1/(\text{altitude})^2$ reaching more than several hundred before impact for surface reflectivities exceeding a few percent.

If the instrument survives impact, it will collect data according to a special sequence. One purpose of these cycles is to measure transient phenomena such

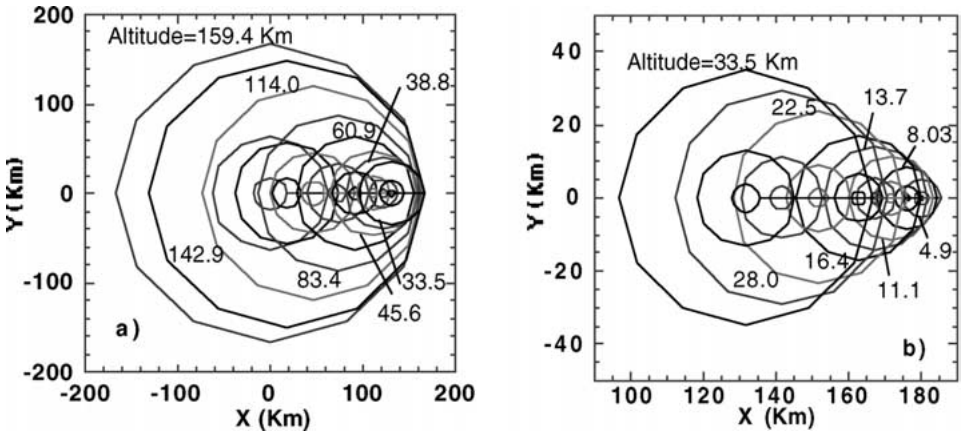

Figure 23. Coverage of image panoramas on Titan's surface including nominal drift due to wind. (a) Image panoramas at altitudes above 30 km altitude, (b) Image panoramas below 35 km.

as reflection from any cloud of dust or spray which may occur due to probe impact. A set of 10 upward- and downward-looking spectra are collected first using the ULV, ULVS, ULIS, DLV, DLVS, and DLIS subinstruments. Following these spectral measurements, images are taken with the three cameras. The SLI should give images from the foreground to 6° above the horizon. If the probe survives long enough, it may be possible to see cloud features blown by the wind. Spectra and image measurement sets are then gathered alternately for the remainder of the mission. Approximately two minutes after impact, the surface science lamp is switched off. After that it is alternately switched on and off every two minutes. All measurements after impact are taken as rapidly as possible until the buffer fills up. After the buffer is full, new measurements are gathered as buffer space allows.

A summary of the data collected in various parts of the descent is given in Table 3. The coverage of the region of the surface seen in the HRI and MRI frames in each panoramic mosaic is given in Figure 23. A nominal wind model was used to generate the drift in probe with time. Figure 23 shows that a significant amount of overlap is expected in various mosaics from which the wind profile can be derived.

Figure 24 shows the areal coverage as a function of spatial resolution for the images from the three frame imagers of DISR. Notice that the resolution at the highest altitudes matches typical resolutions available from the Cassini orbiter camera when the frame covers one tenth of the disk. DISR images begin at this resolution and extend to some three orders of magnitude higher resolution.

4.1. LABORATORY CALIBRATION

During the course of the hardware phase of this work, a total of three complete DISR instruments were produced. The calibration of these units constituted a considerable effort. For each instrument, the relative spectral response, absolute response, field of view, spectral resolution, and spatial resolution were measured over

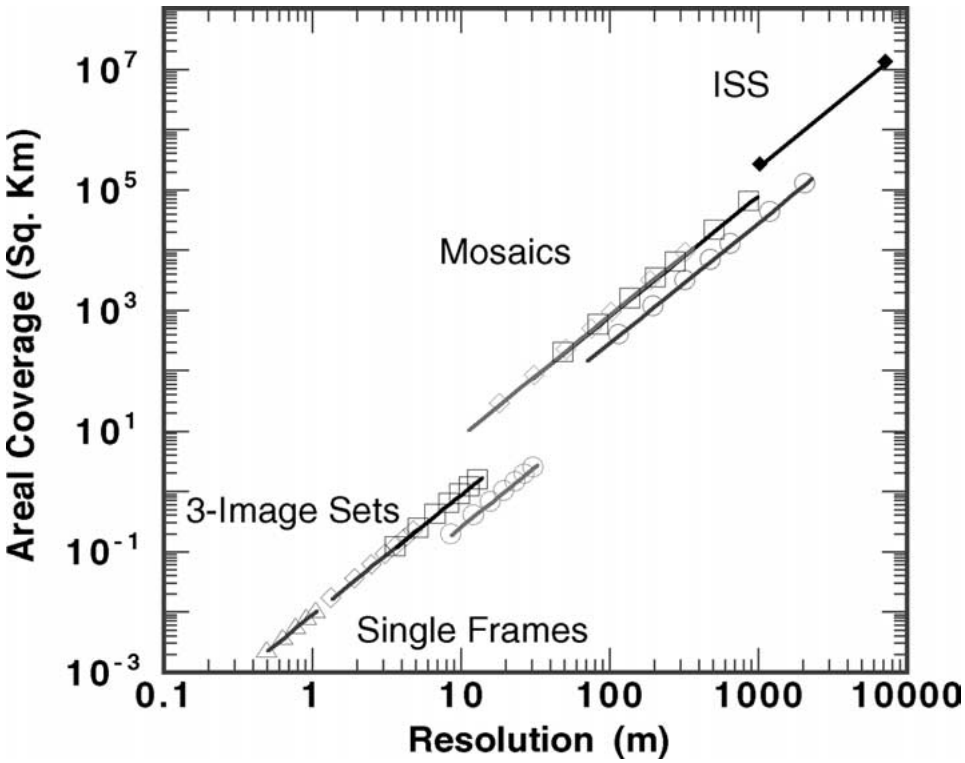

Figure 24. Areal coverage on Titan's surface Vs. Spatial resolution. The coverage and resolution of mosaics made using the SLI (circles), MRI (squares) and the HRI (diamonds). Every other panoramic mosiac is shown as a point. Every other frame of the 3-image sets are shown also using the same symbols. The coverage and resolution of each of the five single HRI frames at the lowest altitudes is shown by a triangle. For comparison, the coverage and resolution of the ISS camera on the Cassini orbiter is shown by solid diamonds when Titan fills the frame, and when the frame covers 1/10 the diameter of Titan.

a temperature range from 180 K to 300 K for the 13 optical systems (subinstruments) which include the three frame imagers, the solar aureole camera (with four channels), the upward and downward looking visible spectrometer, the upward and downward looking infrared spectrometer, the upward and downward looking violet photometers, the sun sensor photometer, the surface science lamp, and the inflight calibration system. Because of the pressure to deliver the instrument in time for integration into the probe, the time available for such tests on the flight instrument was limited to about two months. A total of 5.1 Gbytes of calibration data was collected for the flight instrument during August and September of 1996 before delivery.

These calibration measurements were made using a custom facility designed at the University of Arizona. A key element was the design of a cold box which could be purged with dry nitrogen to prevent condensation on the sensor head. The inside

TABLE 3
Summary of descent data

Altitude Range (km)	36-Image Cycles	Non-Image Cycles	3-Image Sets + Spectra	High-Res. Images Only	Spectra Using Lamp	3-Image Sets	Spectral Sets
160–20	10	33	–	–	–	–	–
20–3	5	–	–	–	–	–	–
3–0.5	–	–	20	–	–	–	–
0.5–0.25	–	–	–	2	–	–	–
0.25–0.0	–	–	–	–	18	–	–
After Impact (first 10 min.)	–	–	–	–	–	83	93

Total number of images: >500.
Total Direct, Diffuse, Upward, Downward sets of flux measurements: 68.
Solar Aureole Measurements: 48 in each of two colors and two polarization states
Surface Spectra: 642 in IR, >3100 in Vis.

of the box was cooled by cold nitrogen gas. In addition, the copper strap attached to the detectors in the sensor head was attached to a clamp cooled by liquid nitrogen and fitted with a heater. The front of the sensor head was mounted through a 3 by 6 inch hole in a 20 inch diameter integrating sphere. Light injected through a small hole in the sphere produced a diffuse illumination that could fill the filed of view of all the DISR instruments simultaneously with a uniformity of 2% or better. The brightness and color of the wall of the sphere could be measured through a second small hole in the sphere.

The wavelength scales of the visible and infrared spectrometers could be determined by illuminating the inside of the sphere with light from neon-mercury and krypton emission line lamps. Driving the temperature of the sensor head while making exposures with all the DISR spectrometers established the wavelength scales of the spectrometers over temperature.

The relative spectral response of the solar aureole cameras and the imagers were measured over temperature by illuminating the integrating sphere with an Optronics OL-750 dual pass monochrometer that was scanned over wavelength at each temperature. The relative output of the monochrometer was monitored with a calibrated silicon and germanium detectors viewing the wall of the integrating sphere through one of the small holes in the sphere.

The absolute response of the each optical system was measured over temperature by illuminating the integrating sphere using a high intensity Optronics 740 tungsten lamp. The brightness and color of the wall of the sphere illuminated with this lamp was measured by using the laboratory spectrometer which was calibrated using an Optronics 455 standard lamp traceable to the bureau of standards.

By using the integrating sphere in this way, all the windows of the DISR instrument could be stimulated simultaneously with light of a known brightness and color while the temperature of the detectors were driven by the cold box.

A separate optical system was used to measure the spatial resolution and field of view of each of the DISR subinstruments at room temperature. A ten inch diameter spherical mirror was used to produce a collimated beam of light. A small reference detector in the beam monitored any changes in the intensity of the lamp. A computer controlled altitude-azimuth mount was built to turn the sensor head through a wide range of angles while each window was centered in the collimated beam. The relative measurements of each DISR optical system over angle were recorded as a function of orientation. More than 1000 points were used to define the relative spatial response of the ULV, DLV, ULIS, and ULIS systems which used bear's ear baffles to limit the field of view to roughly half the upward or downward hemisphere. For the instruments with smaller fields of view, we used several cuts across the field in orthogonal directions. The collimator was fitted with a linear polarizer to measure the orientation of the polarizers in the solar aureole channels, and to confirm the low sensitivity to the orientation of linearly polarized input light light in the spectrometers.

In addition, special calibration targets consisting of vertical and horizontal stripes were imaged by the HRI, MRI, and SLI to measure the geometric distortion across the fields of view of these imagers.

The collimator and the computer driven altitude-azimuth mount were used to produce measures of the point spread function of the imagers and solar aureole camera at many locations in each field of view. In these tests, successive images of the collimated beam were made after steps of a fraction of a pixel in vertical and horizontal directions at several locations in each field of view.

For most of the tests, the detector temperature was above the cold values expected at the end of the Titan descent. For all the calibration tests, data were collected with the illumination source turned on and then off so that any dark signal produced by the detectors could be subtracted from the bright measurements before analysis. This simple need effectively doubled the amount of data that had to be collected for all but the measurements from the infrared spectrometer system, for which the shutter operated at 5 Hz throughout, and both shutter open and closed data was automatically recorded. The dark current produced by each pixel of each of the DISR detectors produced as a function of integration time and temperature was recorded and fitted to a model for comparison with the experience during the mission.

The response of the flight system to the inflight calibration lamps was also recorded over a wide range of temperatures with each of the three redundant calibration lamps.

The calibration of the sun sensor system posed special problems. Normally, sunsensor data are recorded only when the system is locked onto a series of pulses that satisfies the critera loaded in software for being valid pulses due to fairly

regular rotation of the instrument. In this case, a breakout box was used to isolate the analog signals from the detector of the sun sensor system in order to measure the relative spectral response of the system. To test the dynamic behavior of the system, and to obtain a full absolute calibration, a special device was constructed of a flat mirror that could be rotated under computer control in the output beam of the collimator. This reflected collimated beam was swept past the input of the sun sensor system at a variety of spin rates and elevation angles to callibrate this system. The times of the first and third pulse relative to the time of the center pulse as the system was illuminated at various elevation angles served to map the locations of the slits in the sunsor system.

Finally, measurements of the crosstalk from each DISR system into each of the other systems was measured at room temperature was measured in a series of tests in which only a single window at a time was left unmasked on the DISR sensor head. Further, cross talk as a function of temperature was measured by making a series of measurements in the integrating sphere while the temperature of the detectors and optics were driven to simulate the temperature profiles expected during the Titan entry. The actual brightness and color of the wall of the integrating sphere was measured by separate laboratory instrumentation to provide a 'ground truth' in these tests.

The results of the calibration are sufficiently extensive and important to warrent separate publication. We include here only a few samples to give a feeling for the quality of the measurements. Figure 25 shows the relative spectral response of the SLI over a wide range of detector temperatures, while Figure 26 shows the absolute response of the three imagers as a function of detector temperature. Figure 27 shows the relative spectral response of the two solar aureole channels and one of the imagers at a temperature of 200 K. Figure 28 shows the relative spatial response of the ULVS. The relative spectral response of the violet photometer, visible spectrometer, and infrared spectrometer are shown in Figure 29.

5. Results from Test Observations

5.1. Test program

In all, three flight-type DISR sensor heads were built. The intention was to build first a prototype instrument (DISR01) in time to make optical tests which could be used to refine the design if that were to prove necessary. However, delays in development and fabrication resulted in the first instrument being produced at about the time the flight unit was needed for integration into the flight probe. The fabrication of the second unit, DISR02, (to serve as the flight spare) was begun immediatiely upon the completion of the first unit. Hence, optical tests on the first unit were completed too late to influence the fabrication of the second. The first unit was calibrated, delivered, and integrated into the flight probe as rapidly as possible while the second unit was being completed.

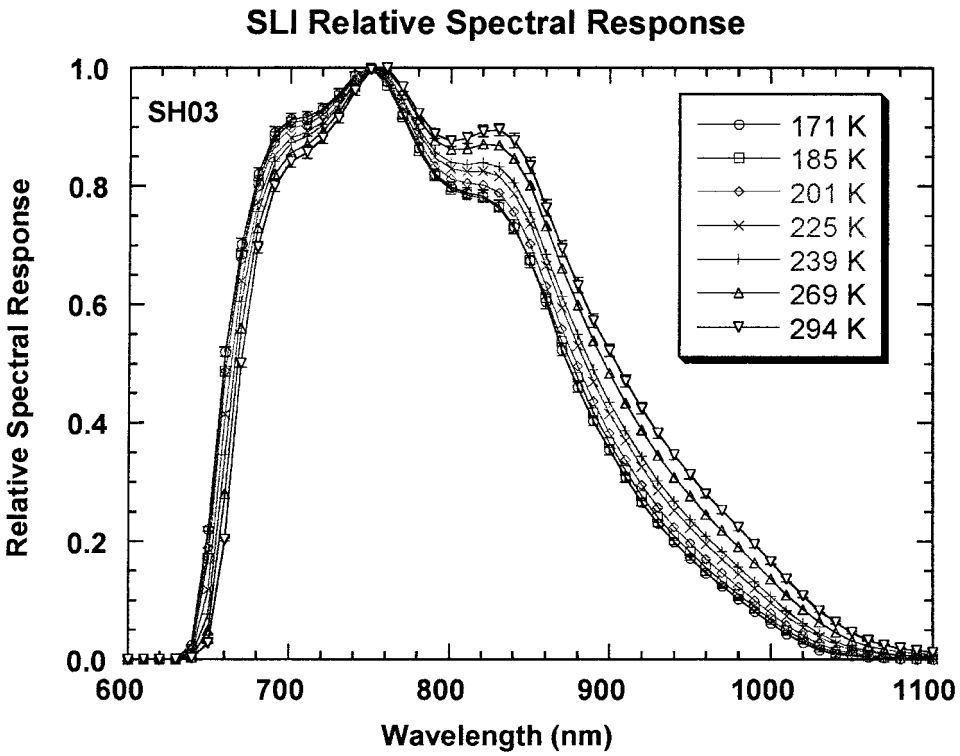

Figure 25. The relative spectral response of the SLI as a function of wavelength at several different detector temperatures, as labeled. The relative spectral response is available for each pixel in the imager. The relative response varies very little over the imager; the curves shown are for the average over the SLI array. The relative spectral response of the MRI and HRI are very similar.

During the testing of the first unit, a problem involving cross talk in the fiber image conduit feeding the CCD was discovered. Imperfections in the conduit permitted a few tenths of a percent of the light traveling down the conduit to scatter across the conduit and then scatter down a portion of the conduit far from the first scattering. In this way, a small fraction of the light can travel laterally a considerable distance across the detector. The amount of light is sufficiently small that it does not affect the performance of any single sub instrument (imager, solar aureole or visible spectrometer). However, because the imagers are broad-band instruments while the visible spectrometer divides the light into 200 spectral bins, the absolute sensitivity of the imagers is some two orders of magnitude greater than that of the spectrometers. Thus, the imagers are saturated by a large factor during the long (1 second) integration necessary for the visible spectrometer measurements. In this way, the light scattered from the imager portion of the conduit can amount to an appreciable fraction of the spectrometer signal when spectra are collected.

The need for rapid delivery of the first unit permitted only small changes to the first unit to partially overcome this effect before integration into the probe. The

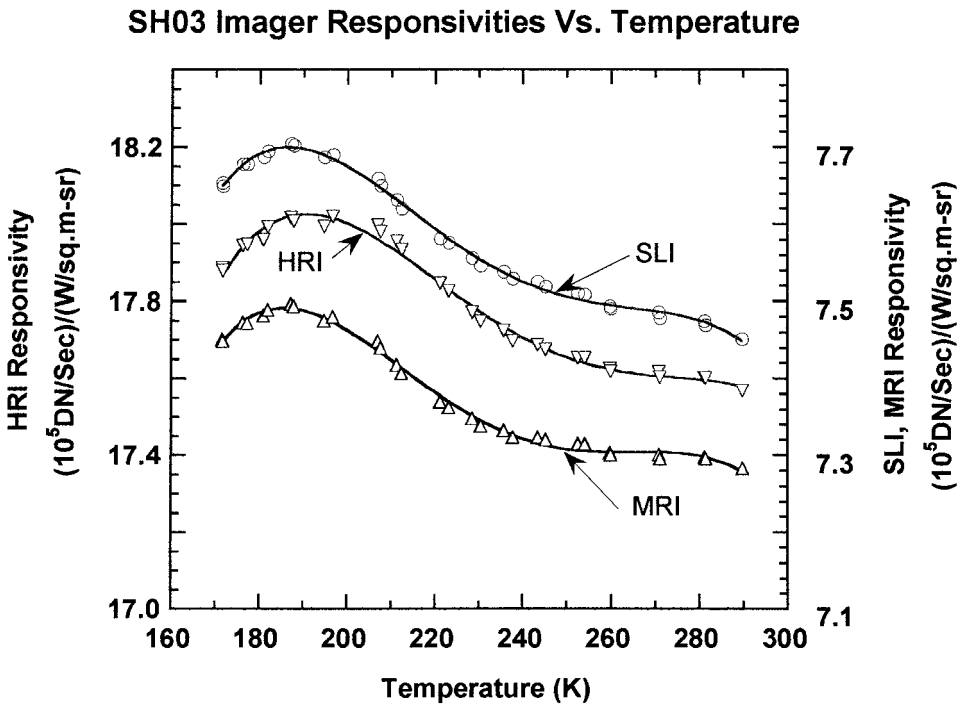

Figure 26. The average absolute response of the three DISR frame imagers as a function of detector temperature, as labeled. The response varies slightly from from pixel to pixel, and the ratios of the responsivity of each pixel to the average are available from the calibration measurements.

crosstalk could be partially compensated by decreasing the transmission of the imager window nearest to the spectrometer portion of the fiber conduit. By decreasing the transmission of the MRI window to 25%, the cross talk from the imagers to the spectrometers was reduced to about 20% or less of the spectrometer signal. In addition, software was added to read additional columns of the detector on each side of the spectrometer columns to measure the scattered light from the imagers during spectral readings. These data could be used to compensate for the light scattered from the imagers and correct the spectral measurements to a few percent. The price paid for this improvement to the visible spectrometer measurements was a decrease in the S/N of the MRI by about a factor 2.

After completion of the second DISR unit, we decided to proceed with the production of a third unit (DISR03) that could largely correct the crosstalk in the fiber optic conduit between the imager and spectrometer portions of the bundle. This was done by using a then-recently space-qualified optically opaque epoxy to bond the separate sections of the fiber optic conduit together. This decreased the cross talk between the imagers and the spectrometers by about an order of magnitude, and permitted the transmission of the MRI window in DISR03 to be doubled relative to that in DISR01. The third unit was tested, calibrated, and exhanged with the first

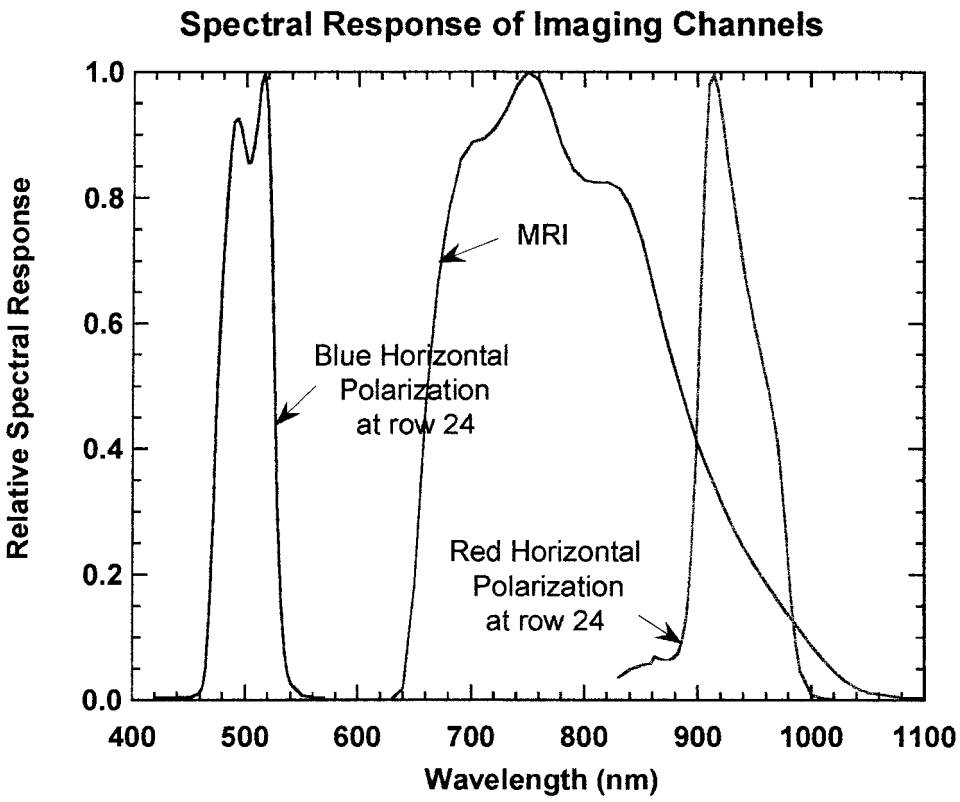

Figure 27. The relative spectral response of two of the solar aureole channels and of one of the frame imagers at a detector temperature of 200 K, as labeled.

unit (DISR01) in the flight probe. DISR03 is the unit currently on its way to Titan, while DISR01 was placed in bonded storage to serve as the flight spare.

Once a good flight model and flight spare model were safely available, DISR02 was available to serve as a field test unit. In view of the complexity of the instrument, we feel it is essential to obtain high fidelity data in the earth's atmosphere that can be used to develop reduction, analysis, and inversion algorithms well in advance of the Titan entry. Thus, we have instituted a modest program to collect a realistic data set using the DISR02 model. This program includes images of natural terrain from a helicopter at several altitudes up to 10,000 feet above the surface, as well as upward and downward solar spectra and solar aureole observations from the ground. In order to obtain these data at realistic integration times for the instrument, we have fastened 1% neutral density filters over the windows of the three imagers and the four solar aureole channels. Some data have been collected with no additional attenuation over the upward or downward looking spectrometers or the violet photometers to avoid any modification of the spatial response functions produced by the external baffles around the diffusers of these instruments. The use of neutral

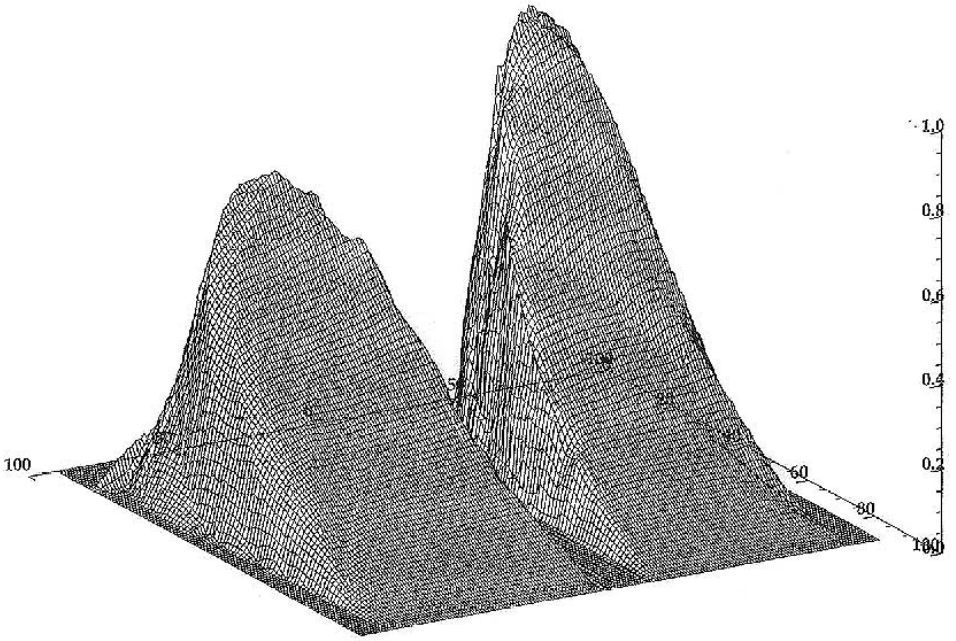

Figure 28. The relative spatial response of the ULVS as a function of azimuth and zenith angle. The gap in response due to the ten degree wide shadow bar is clearly visible.

density filters over the imagers and not over the spectrometers has the advantage of decreasing the cross talk from the imagers to the spectrometers to a negligible level in the DISR02 unit, somewhat as we believe we have achieved with the modified fiber optic conduit in the DISR03 flight unit. In addition, a special absorbing film attenuator was developed which can be fastened over the ULVS, ULV, and DLV diffusers without significantly modifying the spatial response function of these instruments. This has permitted us to obtain unsaturated data from the ULV and DLV systems in the Earth's atmosphere despite the fixed time constant of these systems. Also, we can obtain data from the ULVS system which includes strong crosstalk from the imagers to test our ability to correct for crosstalk using the extra column readings surrounding the visible spectrometer portion of the CCD.

We began our test program by fixing the instrument on a horizontal plate that could be rotated about a vertical axis mounted on the roof of our building. Data from tests using this device were obtained in 'single-measurement mode.' This was followed by tests using a rotating plate driven by a stepper motor to simulate the rotation of the instrument during descent through Titan's atmosphere. In this case, the data were collected in 'descent mode,' and used the sun sensor to determine the azimuth of the observations exactly as planned during Titan entry. Finally, we have begun using a system that can produce a controlled wobble of the spin axis in two dimensions to test our ability to measure and correct for any swinging motion under the parachute during Titan descent. In addition, we have obtained some data during

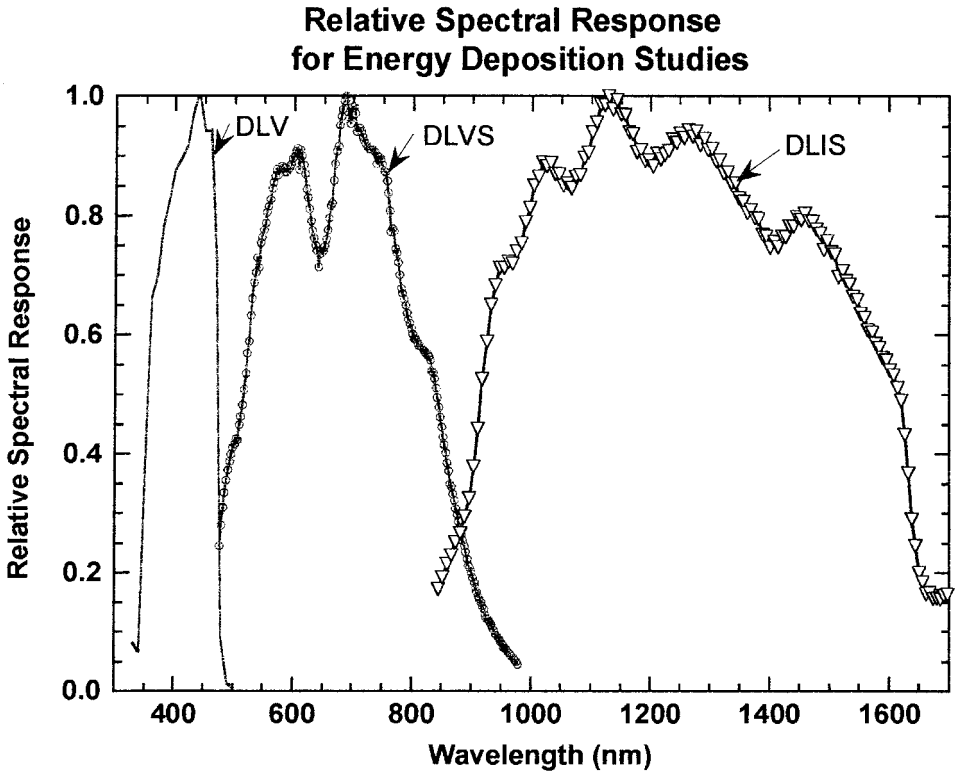

Figure 29. The relative spectral response of the DLV, DLVS, and DLIS at a temperature of 200 K as a function of wavelength. The spectral response of the ULV, ULVS, and ULIS are similar. Together, these channels permit measurment of the upward and downward solar flus from 350 to 1700 nm.

helicopter flights to illustrate the type of imaging data produced by the DISR. We describe some of the data obtained in this program in the following sections to give an impression of the type of data we expect from Titan.

5.2. TOTAL DOWNWARD SOLAR FLUX FROM UPWARD LOOKING SPECTROMETERS

We have used the DISR02 unit to obtain data both in 'single measurement mode' by manually pointing the instrument at the azimuth angles relative to the sun where data are planned for the Titan entry, and with the instrument mounted on a rotating platform and using the sun sensor to control acquisition in 'descent mode' exactly as programmed for Titan entry. The first test was made in 'single measurement mode' on the morning of September 3, 1997 at nine solar zenith angles between about 25° and 50°. We manually aligned the instrument to obtain data at each of the azimuths planned for non-imaging cycles. For the ULVS observations, measurements were made with the instrument pointed at 5.5°, 140°, 180°, 320° and 338° from the azimuth of the sun. For the ULIS, obsevations were made with the

instrument stationary at 0°, 58°, 112°, 180°, 248°, and 302° from the azimuth of the sun.

For both the ULVS and ULIS observations, the count rate when the sun was not directly illuminating the diffuser was fit to a cosine curve in azimuth, and the count rate due to the diffuse sky was predicted at the azimuths where the direct solar beam together with the diffuse skylight illuminated the diffuser. This predicted count rate for the diffuse sky was subtracted from the total count rate from measurements that included the direct beam plus diffuse light. The remaining count rate was divided by the absolute responsivity of the instrument at the location of the sun in the field of view to give the spectrum of the direct beam from the sun. The diffuse measurements alone were reduced to give the average diffuse intensity in the field of view with the approximately cosine zenith angle weighting provided by the diffuser and uniform weighting in azimuth. This value multiplied by π gives the downward diffuse flux. With this processing, the spectrum for the downward diffuse flux and the flux in the reduced direct solar beam is shown in Figure 30 when the sun was at 35° solar zenith angle. When the direct solar beam flux is multiplied by the cosine of the solar zenith angle and added to the downward diffuse flux the resulting total downward solar flux is given in Figure 31. Also shown in this Figure 31 is the downward total solar flux at 35° solar zenith angle outside the atmosphere of the Earth.

Measurements of the type shown in Figure 31 will be available for some 80 different altitudes on Titan below 160 km. They will be combined with the results of the ULV measurements to give the total downward solar flux as a function of altitude. Because no neutral density filter was added over the ULV photometer for the September 3, 1997 test, the ULV data for that day are saturated. The vertical lines in Figure 31 show the portion of the spectrum covered by the violet photometer measurements planned for Titan. The total integrated solar flux from 350 to 1700 nm will be used with the upward flux to give the net flux and the solar heating rate as a function of altitude.

5.3. Extinction optical depth vs. wavelength from upward looking spectrometers

Figure 32 shows the set of nine ULVS spectra of the direct solar beam at solar zenith angles from 25.7° to 50°. Also shown is the solar flux from Neckel and Labs (1984) convolved to the spectral resolution of the ULVS instrument. Figure 33 shows the log of the direct beam flux vs. the secant of the solar zenith angle (the airmass) at a few continuum wavelengths across the ULVS spectra of Figure 32. The natural log of the ratio of spectra at any airmass to the spectrum outside the atmosphere gives the total extinction optical depth for molecular Rayleigh scattering, aerosol particle scattering, and molecular gaseous absorption for that slant path through the atmosphere of the Earth. Figure 34 shows the total vertical extinction optical depth as a function of wavelength from the ULVS and ULIS observations

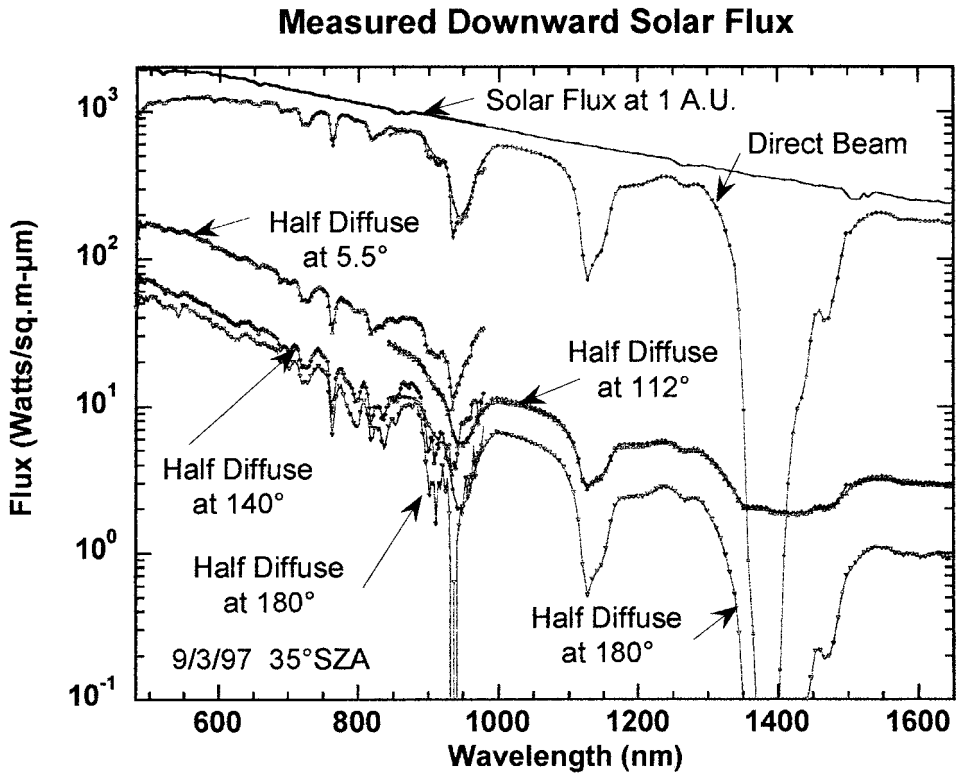

Figure 30. ULVS and ULIS spectra obtained at solar zenith angle 35° for different azimuths from the sun as labeled. The solar flux outside the Eeath's atmosphere is shown, along with the spectrum of the direct solar beam at 35° solar zenith angle. The average intensities observed when the instrument was pointed at azimuths of 5.5°, 140° and 180° from the sun for the ULVS and at 112° and 180° for the ULIS have been multiplied by $\pi/2$ to give the diffuse downward flux in the half of the diffuse beam centered at those locations. The total diffuse downward flux is obtained by fitting the diffuse flux as a function of azimuth by a function that is linear in the cosine of the azimuth. The average of this value multiplied by π is the entire downward diffuse flux.

near 35° solar zenith angle for wavelengths between 460 and 1600 nm. Note the good agreement in the region of overlap between the two spectrometers. Also note from Figure 33 that straight line exponential fits (Beer's law) to the observations at these continuum wavelengths at the nine values of airmass intercept the vertical axis for zero airmass at a flux ratio quite near 1.0, and thus are in good agreement with the Neckel and Labs (1984) solar flux at 1 A.U. outside the Earth's atmosphere.

A more precise confirmation of the absolute calibration of the DISR visible spectrometer is available from the ULVS data covering a wider range of airmass (1.8 to 3.3) obtained in descent mode on the rotating platform during a test on November 23, 1998. Assuming that the direct beam flux follows Beer's law permits extrapolation to zero airmass from these observations. Figure 35 shows this extra-

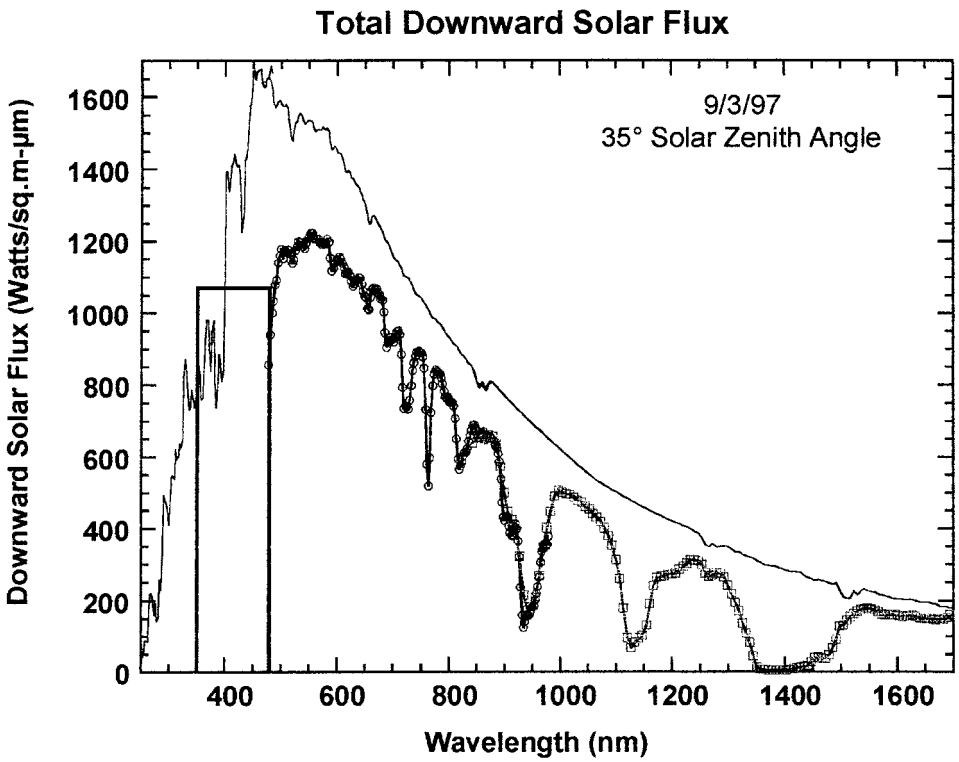

Figure 31. Total direct plus diffuse downward solar flux measured by the ULVS and ULIS for 35° solar zenith angle. The solar flux outside the Earth's atmosphere multiplied by the cosine of 35° is also shown. The observed flux is reduced below that outside the atmosphere by Rayleigh molecular scattering, by aerosol extinction, and by molecular absorption bands of water, oxygen, and ozone. The vertical lines at 350 and 480 nm indicate the passband of our Violet Photometer channels.

polation to zero airmass compared with the Neckel and Labs spectrum at 1 A.U. convolved to the resolution of the DISR ULVS. Note that numerous small features in the Neckel and Labs spectrum are reproduced in the extrapolated ULVS spectrum. The level of the extrapolated spectrum is about 3 percent below the Neckel and Labs measurements in continuum regions of the spectrum.

At wavelengths where molecular absorptions occur in the Earth's atmosphere, the Beer's law extrapolation to zero airmass falls well below the Neckel and Labs spectrum. This is not due to errors in calibration but is due to the nonlinear absorption in the terrestrial molecular bands as shown in Figure 36. Figure 36 shows the observations of November 23, 1998 for 6 wavelengths (all boosted by 3% to adjust for the small calibration shift). At the continuum wavelengths (560, 601, and 701 nm), the data extrapolate linearly to unity (the Neckel and Labs solar flux) at zero airmass. Attempting to extrapolate the data in the three wavelengths which include significant molecular absorption results in an intercept at zero airmass that is significantly below the solar flux outside the atmosphere. Extrapolating the data

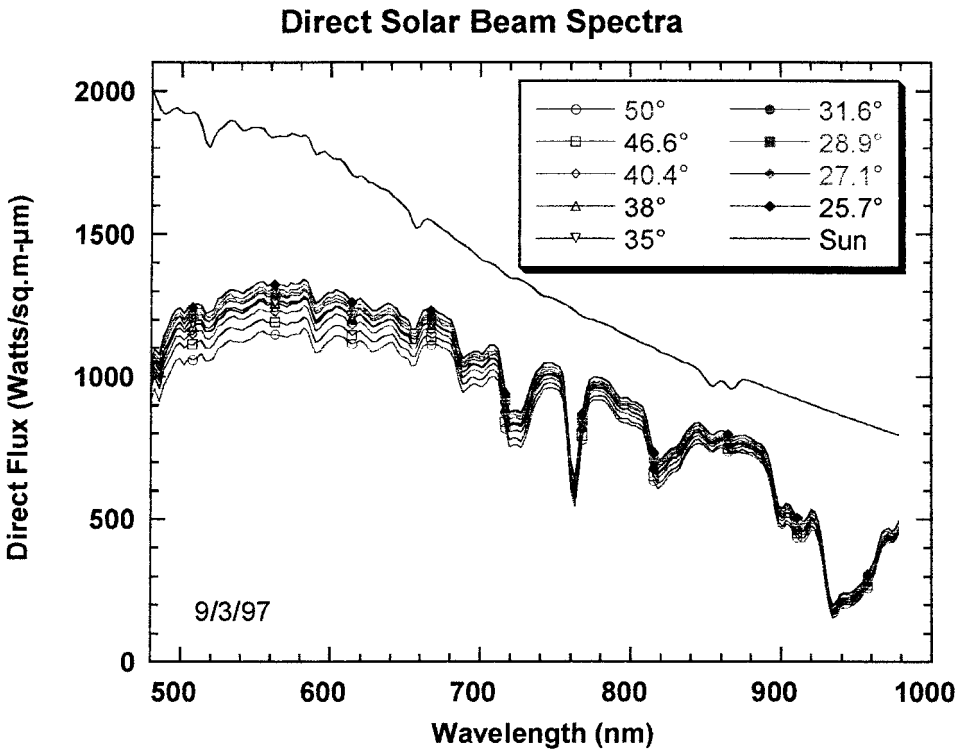

Figure 32. The flux in the direct solar beam measured by the ULVS at 9 solar zenith angles as shown compared to the solar flux outside the atmosphere of the Earth.

assuming that the total extinction optical depth is proportional to the vertical optical depth (kappa) times the airmass to a power, alpha, results in the dashed curves of Figure 36 at these wavelengths. When either the contribution due to particles and Rayleigh scattering (which both have an alpha of unity) dominate the total extinction or the contribution due to the molecular absorption (for which alpha is $<$ unity) clearly dominates the total extinction, kappa and alpha can be found as functions of wavelength from these observations as shown in Figure 37. Notice that the derived value of alpha is >0.95 in the continuum regions (i.e., except in the strong oxygen band near 760 nm and the strong water bands near 680 nm, 720 nm, and longward of 780 nm).

In the data obtained in single measurement mode on September 3, 1997, the optical depth for aerosol scattering was much larger than on November 23, 1998, and so the particle and Rayleigh scattering extinction were subtracted from the total extinction observed in the September test before the nonlinear molecular parameters alpha and kappa were found. The results of the partitioning of Rayleigh scattering, aerosol extinction, and molecular absorption as functions of wavelength for both days are shown in Figure 38. Note that the aerosol extinction was much less on November 23, 1998 than on September 3, 1997. The opposite was true for

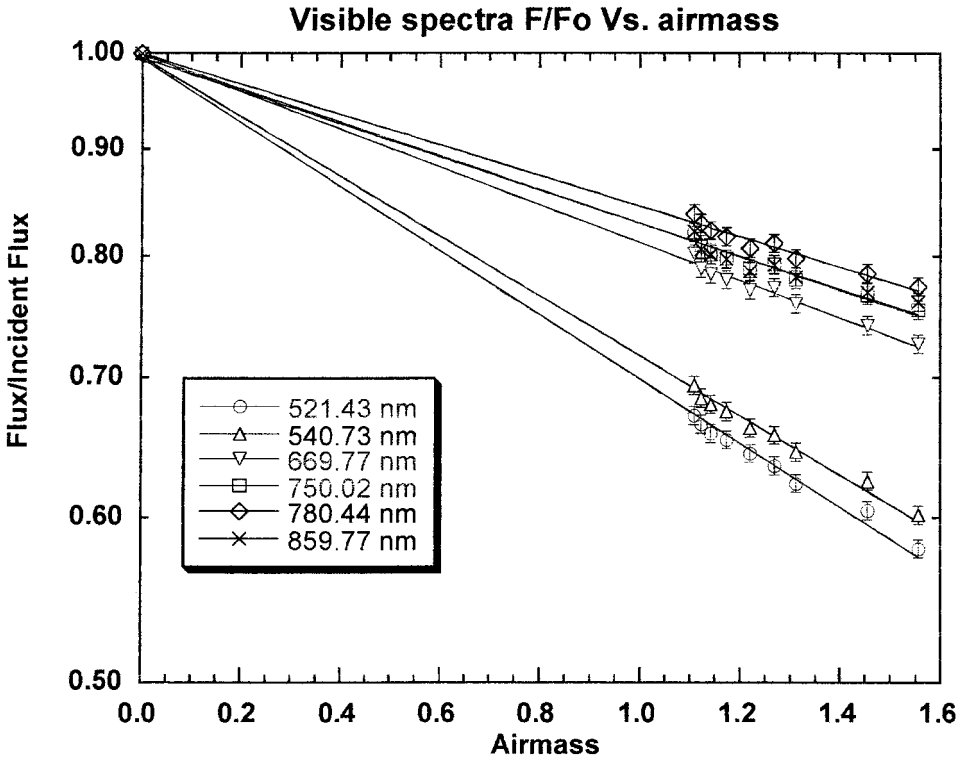

Figure 33. The flux in the direct solar beam at six continuum wavelengths plotted as a function of airmass (secant solar zenith angle). The slopes are the extinction optical depths at each wavelength due to molecular Rayleigh scattering and aerosol particle extinction.

the water absorption. This was larger by roughly a factor of 2 in the September observations compared to the November observations. It is quite reassuring to note that the extinction in the oxygen band at 760 nm remained the same on the two days. While we could not determine the values of alpha from the September observations in the continuum regions after the extinction due to Rayleigh scattering plus aerosols was subtracted (no absorption remained to be fit), the values of alpha derived on both days are in good agreement in the water and oxygen bands since the molecular absorption dominated the small amount of aerosol extinction on November 23 (when the total extinction was fit) and the aerosols and Rayleigh scattering were correctly subtracted before fitting the bands in the September observations.

A final check on the spectral observations of the direct solar beam was made by computing a model spectrum using the Modtran program developed by the U. S. Air Force (Bark *et al.*, 1989). Here the number of free parameters included: (1) the altitude at which the observations were made (to permit computation of Rayleigh molecular scattering and oxygen absorption); (2) the total vertical column abundance of water vapor (taken to be 3.34 precipitable cm in the model shown in Figure 39); and (3) the number density and size of the atmospheric aerosols. The

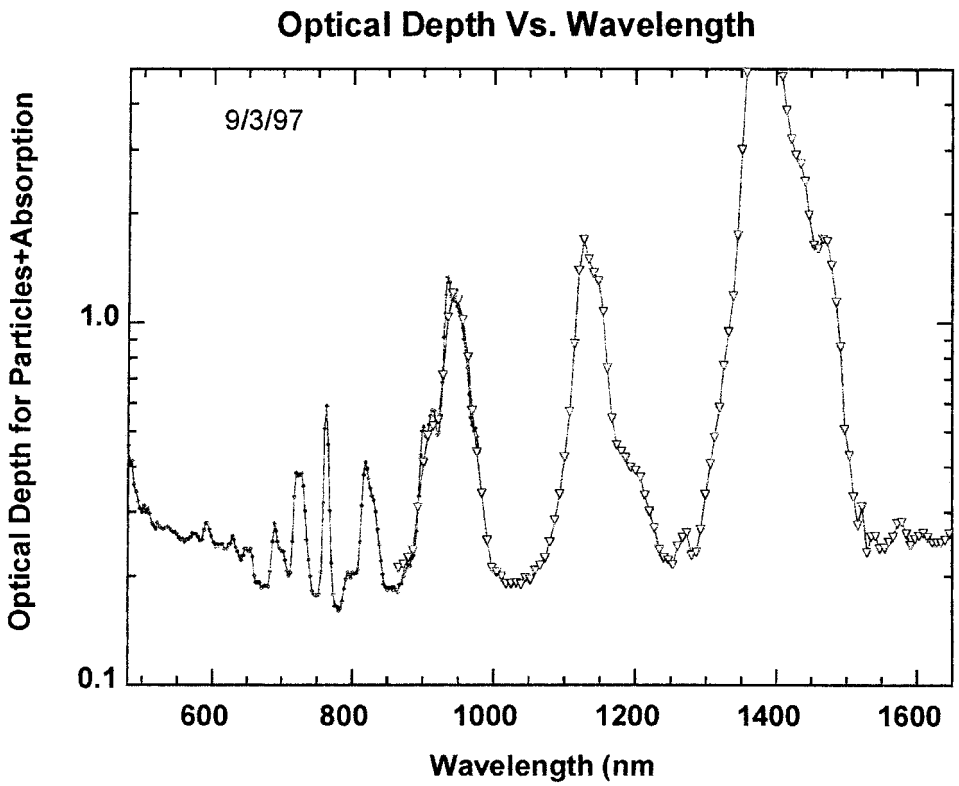

Figure 34. The total extinction optical depth due to Rayleigh scattering, aerosol extinction, and molecular absorption from the ratio of the direct beam fluxes near 35° solar zenith angle and the solar flux outside the Earth's atmosphere from Neckel and Labs (1984). Note the good agreement in the region where the ULVS and ULIS spectrometers overlap between 850 and 960 nm.

aerosol parameters were taken from our analysis of the solar aureole observations in the 500 nm channel, as discussed below. The comparison of the ratios of downward direct beam flux to flux outside the atmosphere as a function of wavelength from the model (solid line) and from our observations of the ULVS and ULIS is shown in Figure 39. In general, the comparison is very good except for the ULVS observations between 800 nm and 960 nm. In this region the responsivity of the CCD changes relatively steeply with temperature. In the calibration of the DISR02 unit the temperature was driven unusually rapidly near room temperature, possibly causing errors in this spectral region. In the calibration of the flight model, DISR03, the temperature was driven more slowly in the temperature ranges of interest during the Titan descent. Nevertheless, the agreement of the model with the observations is gratifying, with the same water abundance fitting the observed shapes of water bands for bands that vary greatly in strength.

During the Titan descent, methane will play a role similar to that of water in the Earth observations. Knowledge of the absorption coefficients for methane as

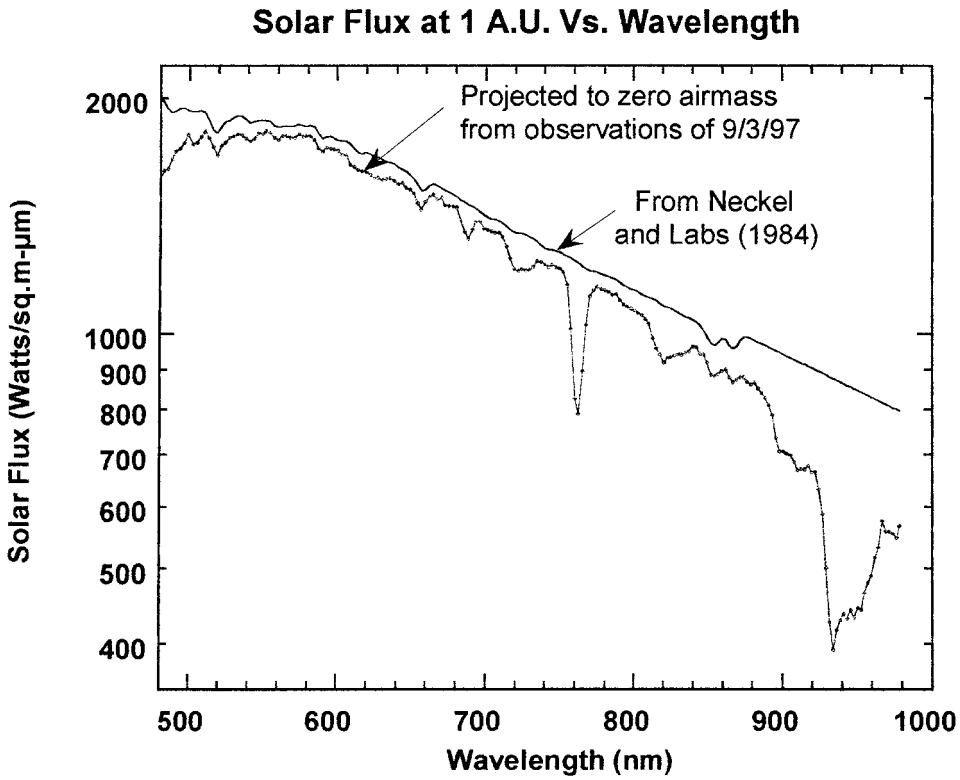

Figure 35. Assuming Beer's law holds, the spectra measured on November 23, 1998 are extrapolated to zero airmass and compared with the measurements of Neckel and Labs (1984). Note that many small solar features are present in the DISR observations. At continuum wavelengths the DISR extrapolation (and hence the DISR calibration) is within about 3% of the Neckel and Labs values. In terrestrial absorption bands, Beer's law does not apply, and the extrapolation is below the values of Labs and Neckel.

functions of wavelength will permit the extinction optical depth due to methane at each altitude to be used to determine the methane abundance as a function of altitude. The wavelength dependence of aerosol extinction will be found at each altitude, and will be compared with the aerosol size found from the solar aureole observations.

5.4. Particle Size and Number Density from Solar Aureole Measurements

The solar aureole measurements are made through polarization analyzers that are oriented vertically and horizontally in filters centered near 500 nm and 935 nm. The data are collected in a section of the detector covering 6 columns by 50 rows at a scale of approximately 1°/pixel. The rows extend from approximately 28 to 78° solar zenith angle. The region of the sky covered is about 6° by 50°. The direction

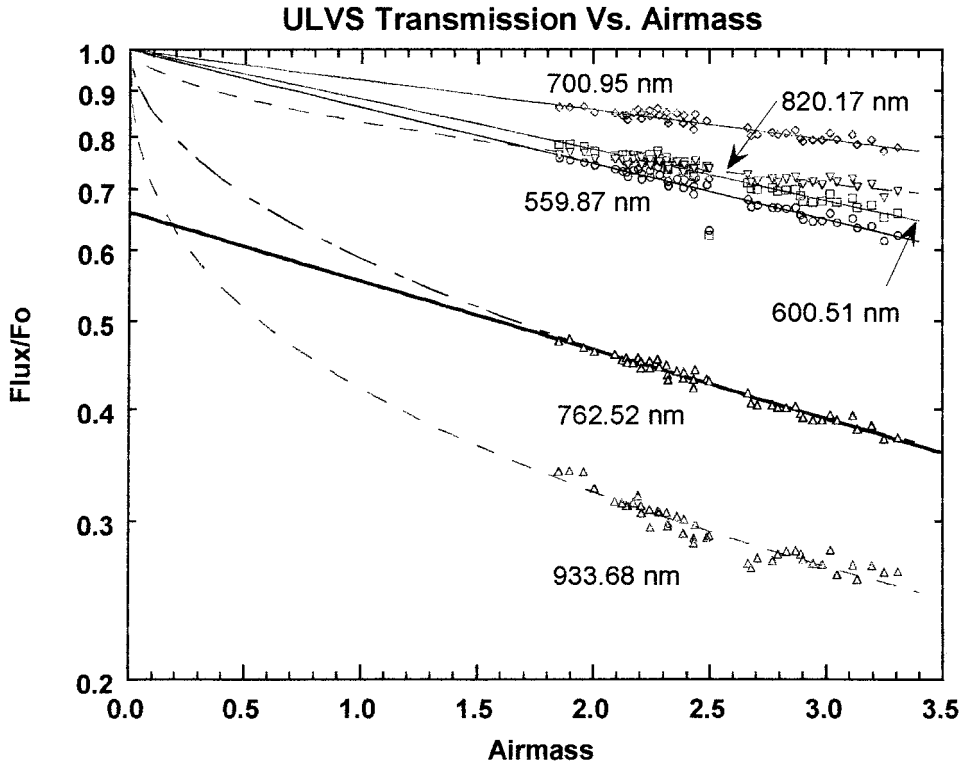

Figure 36. ULVS transmission (Direct beam flux/incident flux from Neckel and Labs (1984) versus airmass at 3 continuum wavelengths and 3 wavelengths in molecular absorption bands. In the continuum wavelengths near 560 nm, 601 nm, and 701 nm linear absorption (Beer's law) holds, as shown by the solid lines. Where molecular absorption is important, the absorption is decidedly nonlinear. The dashed lines show nonlinear absorption proportianal to airmass raised to a power less than 1.0. Note that all the DISR measurements have been boosted by 3% based on the results shown in Figure 35.

of view of the solar aureole channels is tipped about 6° in azimuth to the left (as seen looking out from the sensor head) from the 0° reference meridian of azimuth defined by the sun sensor slit system. Measurements are planned between azimuths of about 5° and 11° and near 180° from the sun. Figure 40 shows the region near the sun observed through the blue channels on September 3, 1997. Here the total intensity is shown obtained by adding the components measured through the vertical and horizontal polarization analyzers. If the direction of polarization is assumed to be known, the measurements can also give the degree of linear polarization. Measurements made near 180° azimuth are polarized perpendicular to the scattering plane (maximum electric vector horizontal) for Rayleigh molecular scattering and for scattering by the small aerosol particles expected in the atmosphere of Titan. Observations made near 180° azimuth are summed for the six columns of the solar

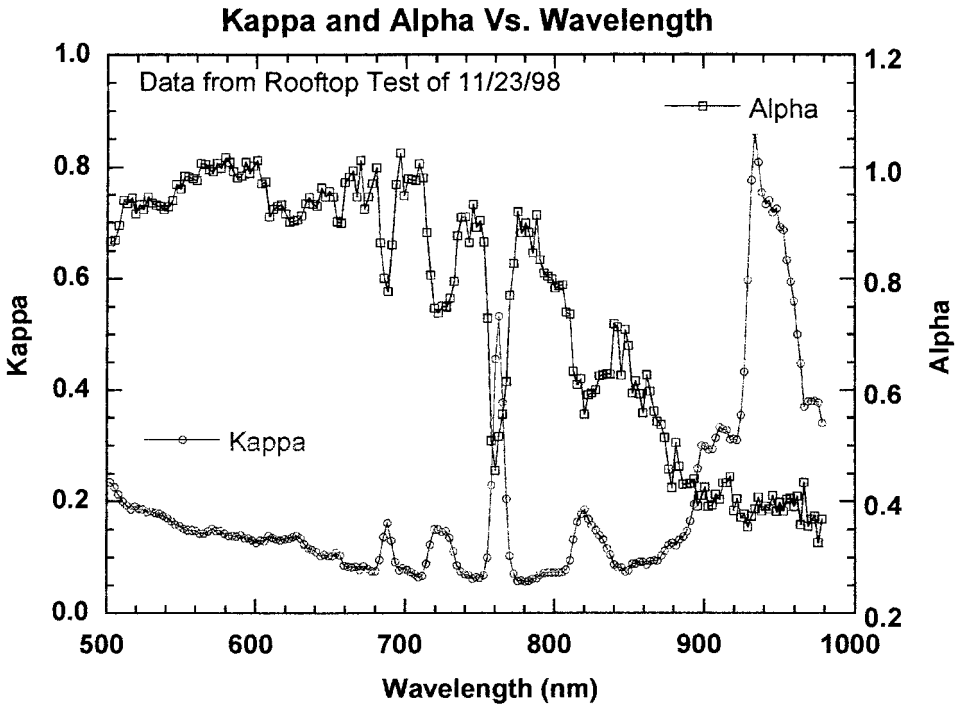

Figure 37. Nonlinear absorption parameters kappa (the extinction optical depth for unit airmass) and alpha where the extinction optical depth = kappa * airmass$^{\alpha}$. Note that alpha is near unity in continuum regions (near 700 nm and shortward of 680 nm) and significantly less than unity in regions where molecular absorption is important.

aureole system in each of the four color and analyzer channels and returned for each of the 50 rows.

Solar Aureole measurements were collected in single measurement mode on September 3, 1997 at nine different solar zenith angles. Figure 40 shows the contours of blue channel intensity (given by I/F where πF is the incident solar flux though the filter bandpass) near the sun. The intensity and the degree of polarization observed for the Earth when the solar zenith angle was 36° are shown in Figure 41. Similar observations are collected in the two red solar aureole channels.

The solar aureole observations are sensitive to the projected-area size of the particles, to the ground reflectivity, to the shape of the single scattering phase function at scattering angles up to some 140°, and to the single scattering polarizing properties of the particles in addition to the total extinction optical depth (determined from the ULVS measurements). Some simple models are shown in Figure 42 compared to the blue observations. It appears that spherical particles with a relatively narrow size distribution characterized by a single effective size are not able to fit the observations well. When the particles are large enough to have about the right shape near the sun, the phase function produces too little

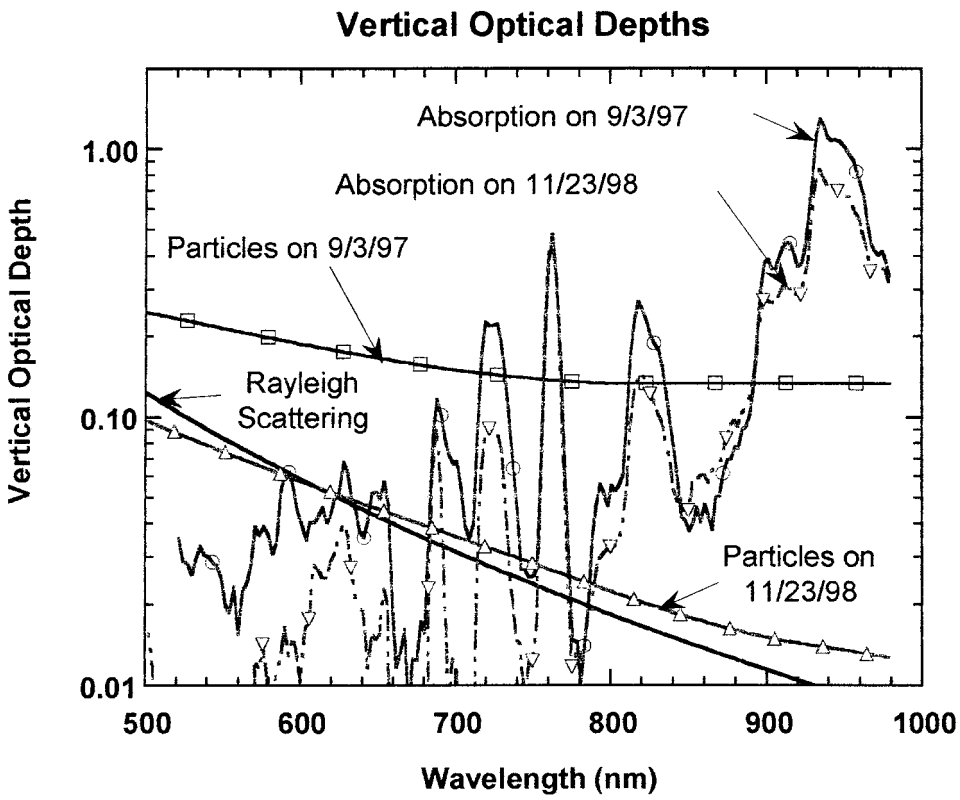

Figure 38. Vertical optical depths due to Rayleigh scattering, aerosol particles, and molecular absorption versus wavelength in two observing sessions as labeled. Note that the vertical optical depth of the oxygen band at 760 nm is unchanged on the two dates, while the aerosol optical depths and the amount of water is rather different.

light 90° from the sun. A baseline model consisting of a layer of small particles (geometric cross section weighted) mean radius of 0.1 μm above (or even mixed with) a layer of particles with a geometric cross section weighted mean radius of 6 μm comes close to fitting the observations. The observations are compared to the baseline model and one model with a narrow size distribution in panel (a) of Figure 42. Panels (b) though (e) show the baseline model with one parameter at a time changed away from the best-fitting value. Panel (b) shows that the height of the peak near the sun constrains the radius of the large particles to be near 6 μm. Panel (c) shows that the shape of the observations some 10 to 20° from the sun constrains the radius of the small particles to be near 0.10 μm. Panel (d) shows that the observed brightness near 90° scattering angle (azimuth = 180° and zenith = 50°) constrains the vertical optical depth of the small particles to a value near 0.10 when the total aerosol optical depth is fixed at 0.25 from the ULVS observations at 500 nm. Panel (e) shows that the ground reflectivity is constrained to be near

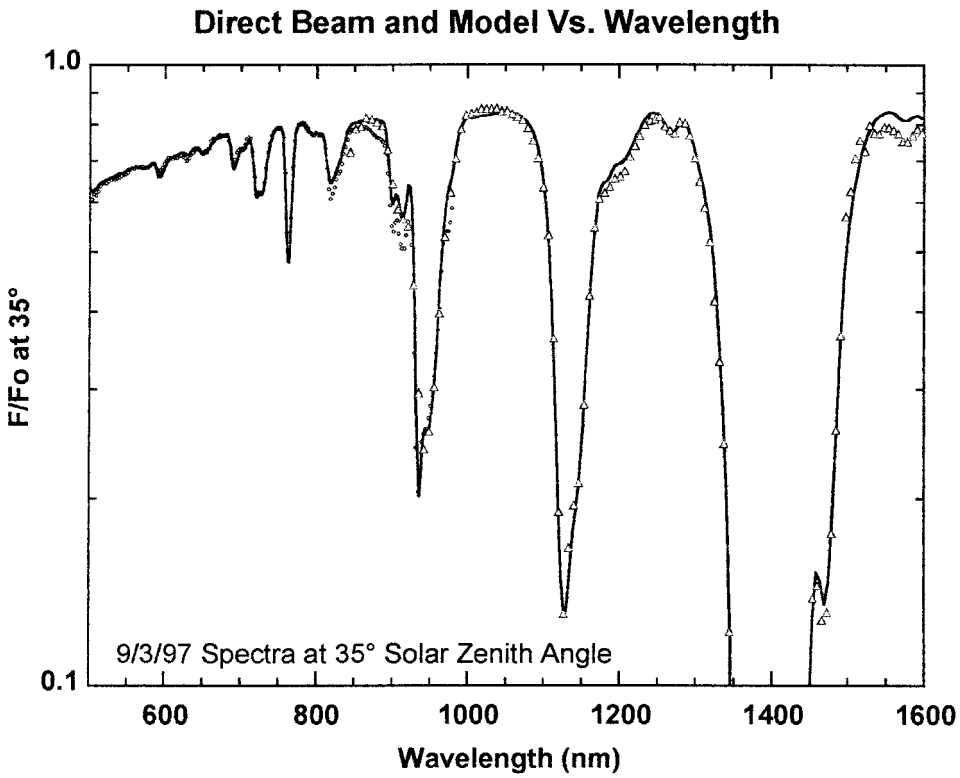

Figure 39. Solar flux measured at 35° solar zenith angle divided by solar flux ourside the Earth's atmosphere as a function of wavelength from the ULVS (dots) and the ULIS (triangles). The heave solid curve is a model computation using the Modtran program developed by the Air Force. The absorption bands of oxygen (near 640 and 760 nm) of water vapor (most other significant features) and continuum extinction due to atmospheric aerosols plus Rayleigh scattering are shown. The free parameters of the fit include the altitude of the observation (for molecular scattering and oxygen absorption), the amount of water vapor in the atmosphere (3.34 precipitable cm), and the number density and size of atmospheric aerosols (derived from our solar aureole observations below.)

0.05 μm by the observations near the horizon both in the direction toward and away from the sun.

Figure 43 shows the predicted extinction optical depth for the solar aureole baseline model as a function of wavelength compared to the extinction optical depth measured from the upward-looking visible spectrometer at several continuum wavelengths on the same day. Note that the large particles alone have nearly a constant extinction optical depth with wavelength, unlike the spectral observations. When a component of small particles is added in the baseline model, the predicted extinction optical depth is in reasonable agreement with the spectral observations. The models shown in panels (b) through (e) give some idea of the uncertainty in each of the parameters in the baseline model.

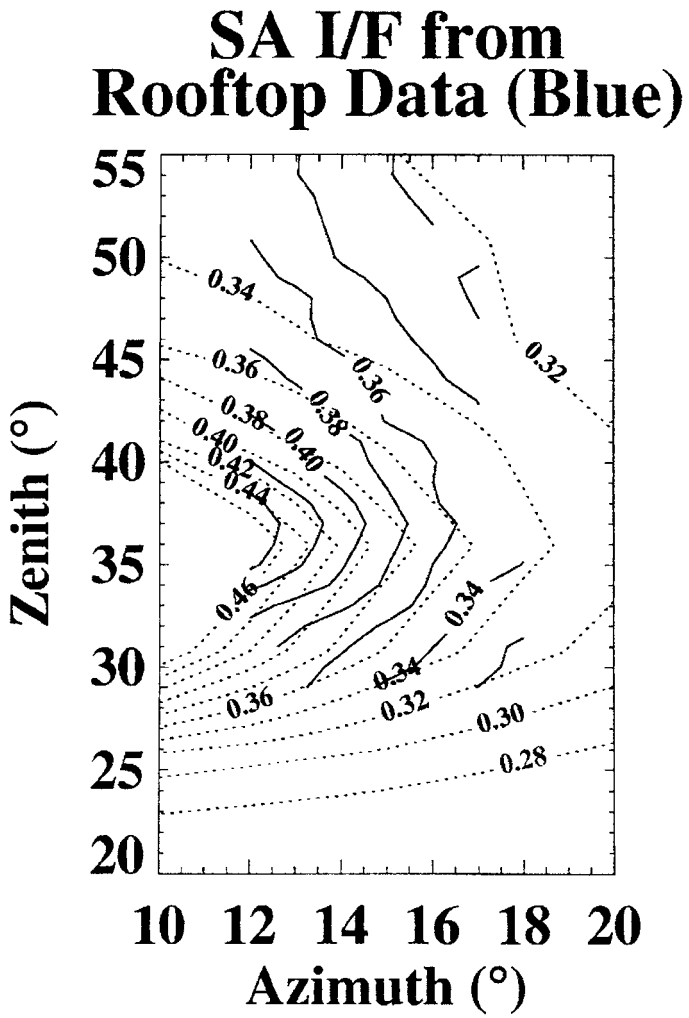

Figure 40. Contours of I/F near the azimuth of the sun in the blue Solar Aureole channel observed when the solar zenith angle is 36°.

For these observations in the atmosphere of the Earth, the 6 μm radius particles may be associated with water droplets in a thin haze. The population of particles with radius near 0.1 μm may be associated with sulfate pollution products. Other observers (see Remer *et al.*, 1997) have often noted bimodal and even trimodal populations of aerosols in urban areas.

On Titan, the situation will be different, but a similar interaction of the solar aureole and upward-looking spectrometer observations is expected. On Titan the process will be easier in that we will have observations at a large number of altitudes, and can follow the changes of particle size with depth one layer at a time with the properties of the particles at all higher altitudes already determined. The

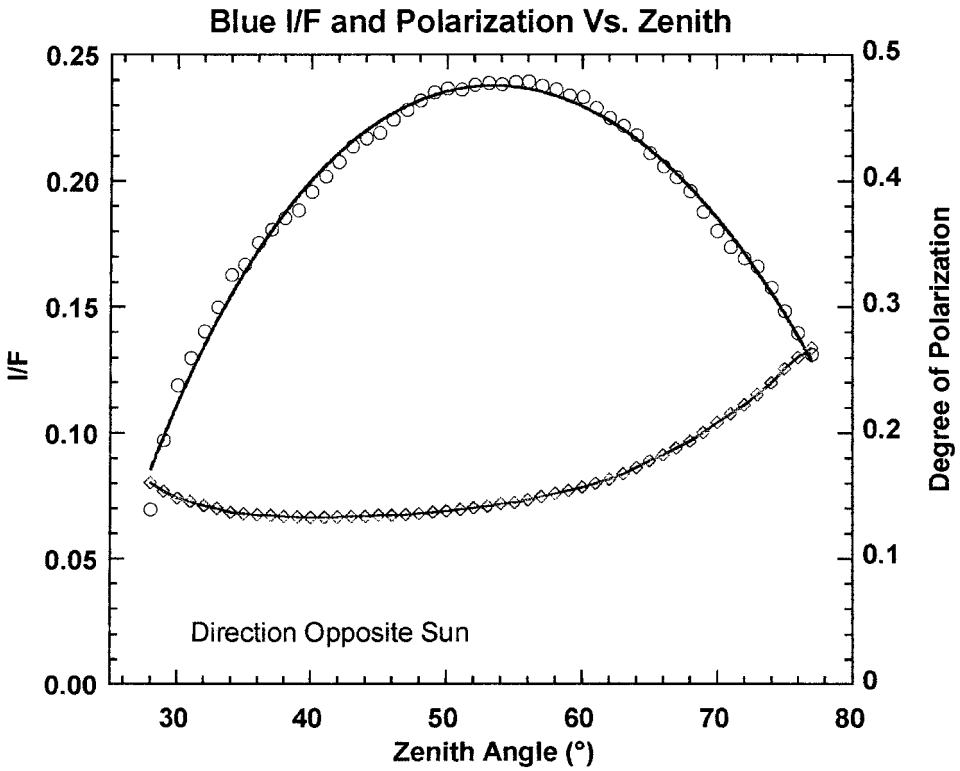

Figure 41. The intensity I/F (shown by diamonds, where πF is the incident solar flux) and degree of polarization circles in the blue solar aureole channel at 180° azimuth as a function of zenith angle. The solar zenith angle of the observations is some 36°.

situation will be more difficult in that single scattering calculations will have to be available for non-spherical fractal particle aggregates. Also, calculations for the spherical atmosphere rather than for plane parallel layers will be needed. Finally, however, the addition of the red solar aureole observations will give enhanced sensitivity at low altitudes while the blue channel will give good sensitivity at high altitudes because of the much larger optical depth of the expected small particles at blue compared with red wavelengths on Titan.

5.5. PANORAMIC IMAGES

On December 17, 1997, near the winter solstice, we flew DISR02 in a helicopter over Picacho Peak, Arizona. Images were recorded at 4 different altitudes above ground level (150, 1280, 2500, 3260 m) at local times between 11:00 to 15:30. Solar zenith angles ranged from 57 to 72°, similar to those anticipated during the descent to Titan's surface in November, 2004. At each altitude we acquired 24 sets of simultaneous exposures of the HRI, MRI and SLI for a total of 72 images. The

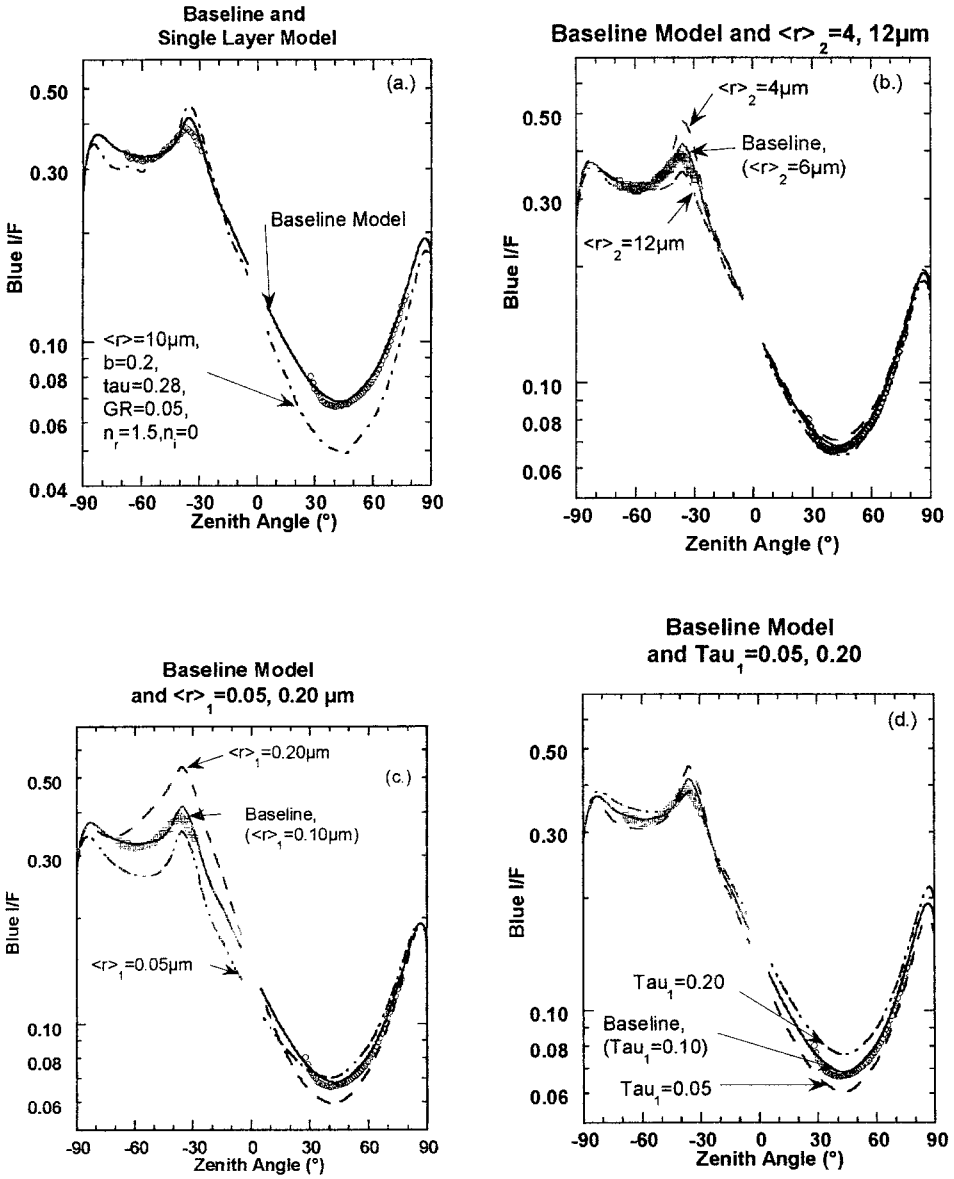

Figure 42. The intensity I/F (where πF is the incident solar flux) as a function of zenith angle at 15° azimuth from the sun (as negative zenith angles) and and opposite the azimuth of the sun. In (a), a model with a single layer of particles is compared with the observations. When the particle size is adjusted to fit near the sun, the brightness opposite the sun is much too low. The baseline model consisting of a layer of particles with $\langle r \rangle = 0.1\,\mu\text{m}$ above a layer with $\langle r \rangle = 6\,\mu\text{m}$ is also shown. In panels (b) through (e) one parameter at a time is adjusted away from the baseline model. The regions of the data that are sensitive to the size of the large and small particles, the optical thickness of the small particles (with fixed total optical depth), and the ground reflectivity are shown.

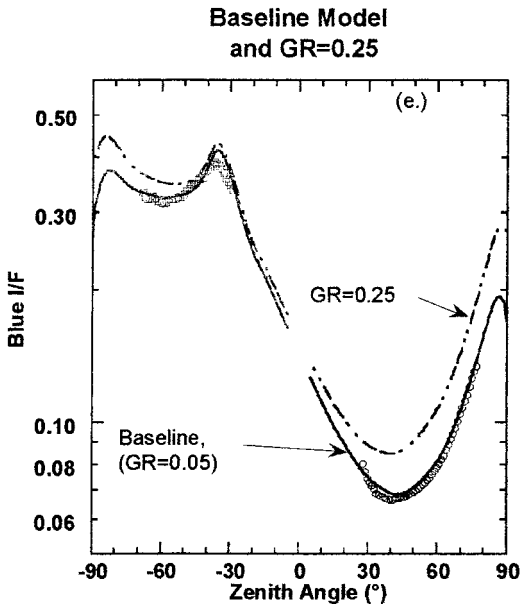

Figure 42. Continued.

exposures were staggered by about 30° in azimuth. The three highest-altitude sets contained sufficient overlap to allow the construction of panoramic mosaics.

Assembling each set of two-dozen image triplets into a mosaic requires determining the roll, pitch and yaw angles and the vertical and horizontal displacements of the DISR Sensor Head relative to some absolute origin at the time each triplet is recorded. During the descent, the values of the altitude, the yaw and a combination of the roll and pitch will be available from DISR housekeeping information, but the other attitudinal and positional variables must be fixed using the recorded scene information. Anticipating this need, an image-driven registration algorithm has been developed. It acquires the fiducials necessary for constructing a properly rectified and registered mosaic from the images themselves. The Picacho Peak test flight serves as a rigorous test of this strategy.

The registration procedure requires knowing the approximate altitude and the radius of the planet's surface. It is based on the geometry map generated by the calibration of each imager's optical distortion field. This mapping assigned each pixel, in each of the three DISR imagers, two dihedral field angles relative to the center of each imager's field of view. These relative maps were combined with the results of an additional calibration: one that determined the absolute pointing of several tens of individual pixels in each imager's field. Joining the two calibration data sets resulted in the assignment of an absolute nadir and an absolute azimuth angle to each of the imager pixels.

Possessed of this pointing information, and using a graphical interface which allows images to be magnified, contrast-stretched and individual pixels to be iden-

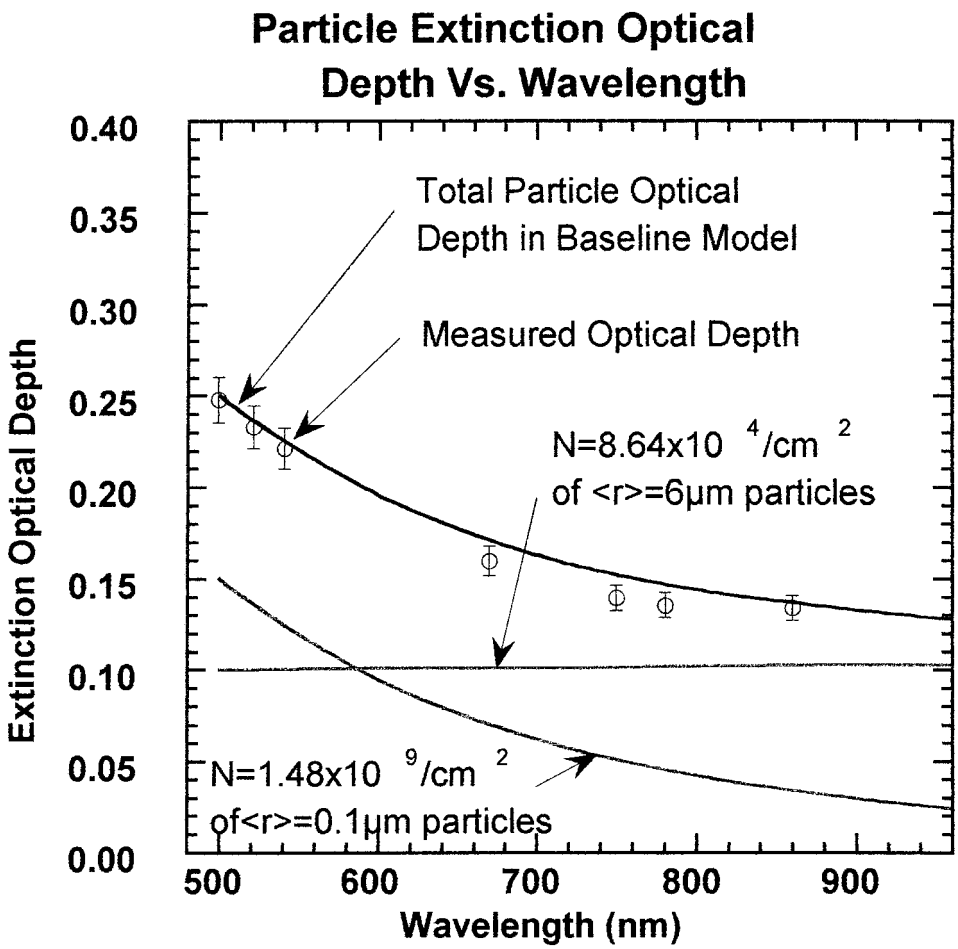

Figure 43. The extinction optical depth of the particles determined from the upward-looking visible spectrometer (points) compared with the extinction optical depth as a function of wavelength of the particles in the baseline model. The extinction optical depths of the small particle component, the large particle component, and the total extinction optical depth of the particles in the baseline model are shown. Note that the baseline model determined from the total extinction optical depth and solar aureole measurements at 500 nm are in reasonable agreement with the extinction optical depth determined throughout the wavelength region from 500 nm to 1000 nm.

tified as control points, the images are projected onto two planes: (1) a mercator plane, in which the horizon is projected as a horizontal line and (2) a gnomonic plane, where straight lines on the surface of the Earth are preserved. First, in the mercator plane, the horizon line is identified and located in each SLI image. Roll and pitch angles sufficient to make the horizon horizontal and place it at the projection coordinate appropriate to its nadir angle are determined for each corresponding triplet. Yaw angles are roughly determined. Then, in the gnomonic plane, MRI and HRI images are displaced (X and Y), rotated (yaw) and magnified

or contracted in size (Z) as needed to achieve a faithful relative alignment. Given the incomplete decoupling between motions and the obscuration of control points, significant iteration between these orthogonal projection planes is required. Two additional projections, stereographic and conic, also help to minimize distortion and reveal additional detail. After achieving geometric registration, a Hapke (1981) model of the average surface reflectance is derived from the pointing information and solar position and divided into the observed intensities at each location to photometrically balance the individual images of the mosaic observed at different scattering geometries.

The resulting panoramic mosaics are shown in Figures 44, 45, and 46. In Figure 44, a mosaic of the (72) images recorded near 3260 m altitude is shown in a stereographic projection. This projection emphasizes the SLI frames and the 50°-wide vertical field of view they provide, a view that includes the horizon and cloud features above the horizon. It shows the success of the photometric model in equalizing the stretch of the various individual frames, especially those near the anti-sunward direction around Picacho Peak itself, which had been washed out by a considerable backscatter. A solar glory has been revealed in one of the frames opposite to the sun's position and the shadow cast by the mountain is also evident.

In Figures 45 and 46, the data are shown projected onto a plane tangent to the Earth's surface (gnomonic). Figure 45 displays only the images of the two downward-pointing higher-resolution imagers, the HRI and MRI. Its outer boundary is near 55° nadir angle. Figure 46 shows a magnified view of the central part of Figure 45 to illustrate the full resolution of the HRI images.

In all three versions of the mosaic, the many squares of farmed land act as a grid pattern that rigorously tests the ability of the algorithm to align the images. The procedure is successful, demonstrating an alignment with a typical error of about one pixel in a test where the unknowns are less determined than they will be when constructing the actual Titan panoramic mosaics. The mission mosaics should be easier to produce in two respects: The descent module is not likely to gyrate as sporadically as did the helicopter during the Picacho flight and, as mentioned above, several of the parameters describing the attitude of the instrument will be available from housekeeping data.

5.6. Downward looking visible reflection spectra (spectrophotometric mode)

Images of the campus of the University of Arizona were obtained using DISR02 from a rotating platform fastened to one corner of the roof of the Lunar and Planetary Laboratory building. When these data were taken, DLVS spectra were also taken every 3.75° in azimuth. These spectra were obtained to simulate the data we expect to collect at two altitudes in the 'Spectrophotometric Map' cycles during the Titan descent. The imaging data are displayed as a panoramic image in Figure 47. Here the DLVS spectra were binned into 'blue', 'green' and 'red' channels as well

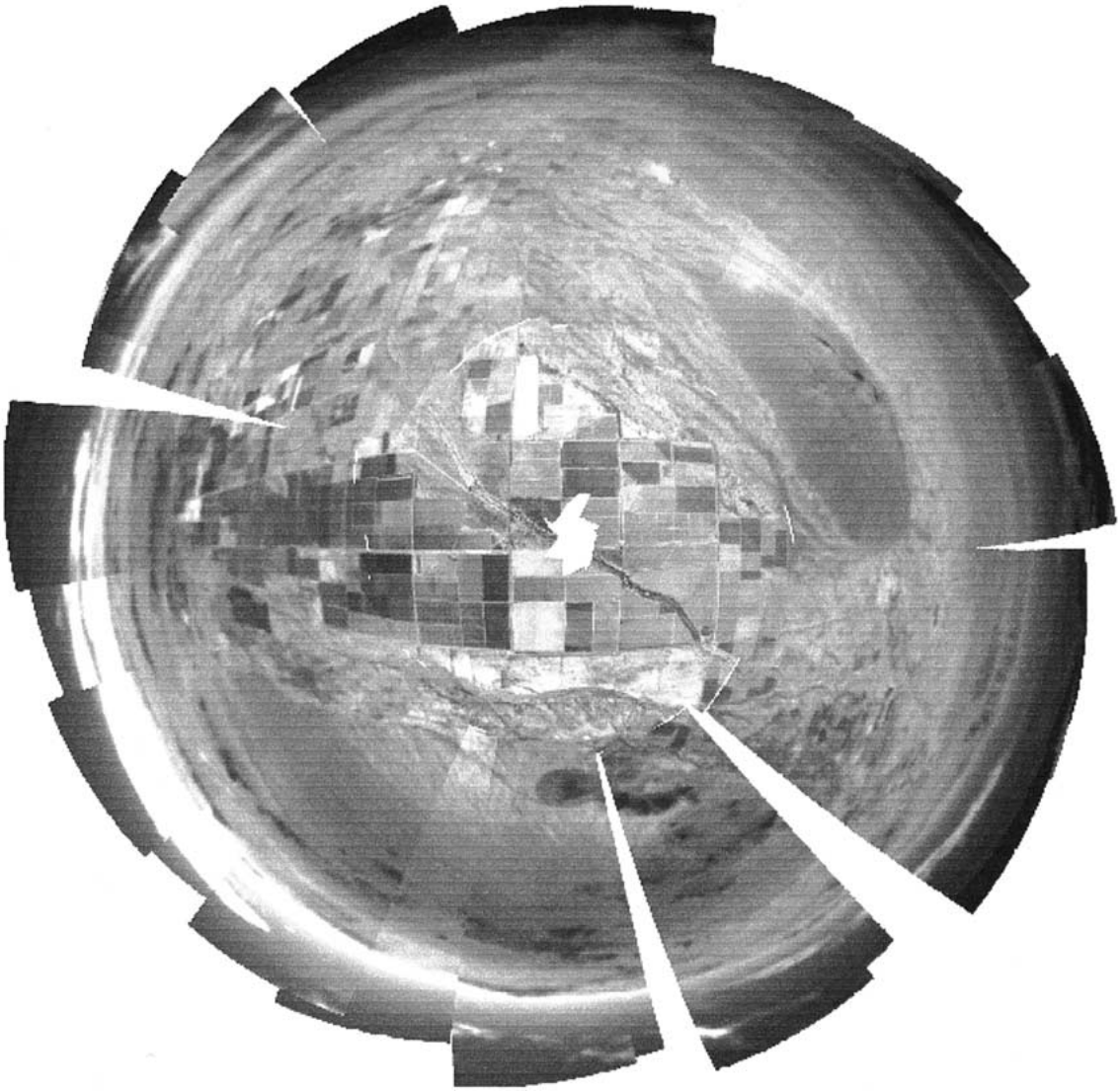

Figure 44. Stereographic projection of Picacho Peak from 3260 m altitude.

as in an 'IR' channel extending from 660 nm to 1000 nm. The ratio of blue/IR, green/IR, and red/IR were interpolated in the spectral map and the ratios multiplied by the intensity observed in the IR image mosaic generated from the imaging data. The result is an image that contains high spatial resolution intensity information and lower resolution color information. The same method can be used to obtain color information from the spectrophotometric maps planned for Titan. At other altitudes, correlations of reflection spectra with different morphological types of terrain may permit other color image displays.

Figure 45. Gnomonic projection of Picacho Peak area from 3260 m altitude showing the images from the MRI and HRI.

Notice that four blocks in the color image are marked in the image of Figure 47. The upward intensity spectra of these four regions are shown in Figure 48. Figure 49 shows the four spectra divided by a model of the total downward solar spectrum at the zenith angle of the sun when the DLVS spectra were obtained. In this way the atmospheric features in the reflected light can be corrected, and spectra of surface spectral reflectivity (I/F) can be produced Notice the relatively smooth spectrum of the concrete sidewalk, the spectrum of the green grass (with its high

Figure 46. Enlargement of the central portion of Figure 45 to show the full resolution of the HRI imager near the nadir.

reflectivity at wavelengths longer than 720 nm, and the bumps in the red portion of the spectrum from the two samples where dirt was visible among the grass. Similar techniques are planned for the Titan observations.

Figure 47. Gnomic projection of U. of A. Campus from the roof of the Lunar and Planetary Laboratory building. The high spatial resolution information from the MRI and HRI is combined with the low spatial resolution spectral information from the DLVS in spectrophotometric mode to add color to the image. Spectra at the four regions marked in the figure are shown in Figure 48.

5.7. Downward looking IR spectra using the surface science lamp

We also were able to observe using the DLVS and DLIS after sunset using the surface science lamp to illuminate a portion of a dusty asphalt street behind the Lunar and Planetary Laboratory building on the campus of the University of Arizona. The instrument was some 20 m above the street when the observations were made. The spectral reflection of the dry street from these measurements is shown in Figure 50. The dips in the apparant reflectivity near 950, 1130, and 1380 nm are due to the strong absorption due to water vapor in the 40 m path from the instrument to the street and back to the instrument. After these data were obtained, we soaked the street with water and observed the reflection spectrum a second

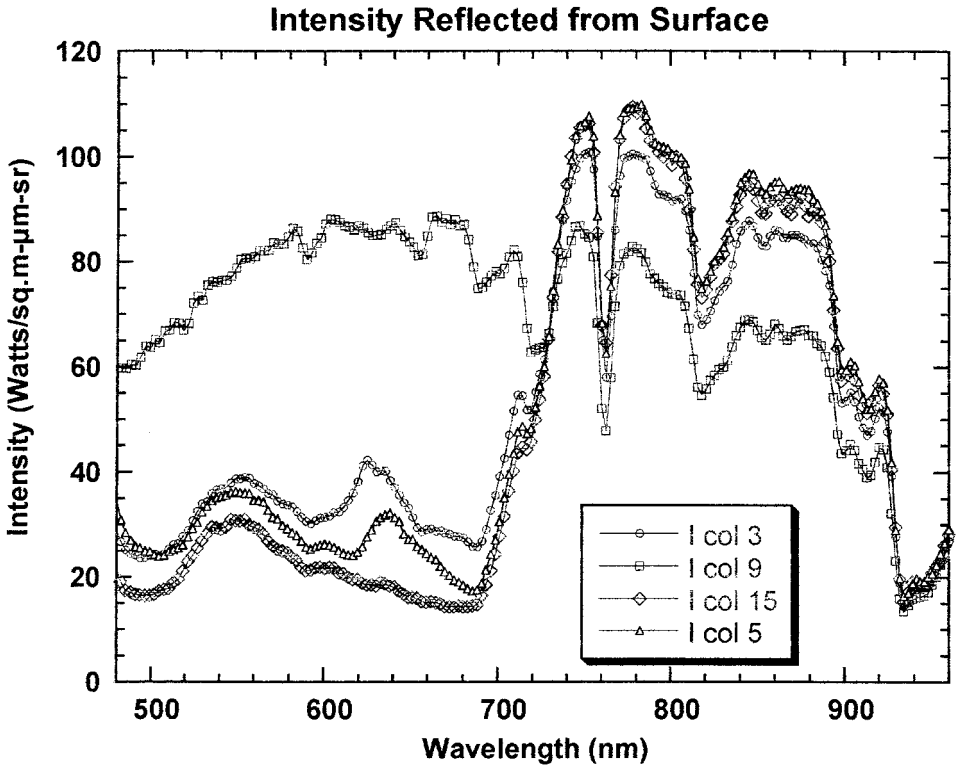

Figure 48. The intensity I in Watts/(sq.m-μm-sr) reflected from the four regions on the surface marked in Figure 47. The presence of atmospheric molecular absorption features is clearly seen.

time. Note the lower reflectivity after wetting the street, and what appears to be a rather different shape for the water bands in the near IR (likely due to liquid water on the surface rather than only gaseous water vapor in the path between the instrument and the street). Similar measurements are planned for the lowest 200 m of the descent on Titan in order to obtain continuous spectral measurements of the reflectivity of the surface, even including regions where strong methane bands prevent the penetration of sunlight to illuminate the surface. As in the case for the Earth, corrections may have to be made for gaseous absorption in the tens of meter path between the instrument and the surface.

5.8. SUN SENSOR MEASUREMENTS

We made the first test using an apparatus that spins the instrument at a controlled spin rate as a function of time on August 3, 1998. On that day we rotated the instrument at a variable rate with time similar to the rotation rate profile we expect during entry into Titan's atmosphere. The measurements of the rotation rate from the times of the center slit crossings of the DISR sun sensor are shown for another test on October 2, 1998 in Figure 51. Notice that the measurements are well

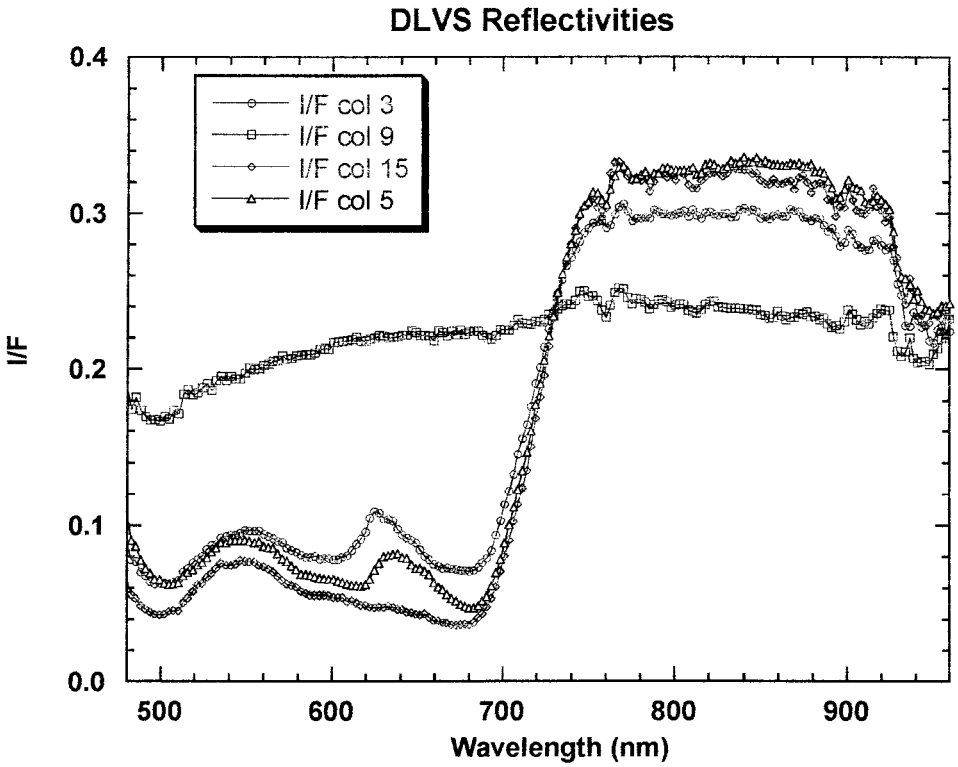

Figure 49. The intensity spectra in Figure 48 divided by a model of the total downward solar flux through the Earth's atmosphere based on the measurements of the ULVS. Note that most atmospheric absorption features have been eliminated. The small remaining feature at 760 nm is due to the slightly different spectral resolution in the ULVS and DLVS.

behaved. Near some 2300 seconds into the test the solar zenith angle was about 67°. During several of our tests using DISR02 we noticed a tendency to lose lock for a few rotations and then reacquire lock a few times near this zenith angle. We suspect that the narrow slits in the sun sensor of our field test unit, DISR02, may be partially obstructed by debris at this zenith angle. In any case, the sun sensor was able to control the azimuth of the data collection during all but a few minutes of the descent, and very nominal data sets have been acquired during our tests.

Figure 52 shows the measurements of the angle from the instrument vertical (perpendicular to the instrument baseplate) and the direction to the sun during the October 2 test as a function of time as well as the true solar zenith angle as a function of mission time on that day. The measured zenith angle agrees with the computed zenith angle to about 0.2°, about the accuracy with which we are able to level the instrument on our rotating apparatus. The rms deviations from the slow trend in the error are 0.12°. This is about what we expect from the ability of our rotating table to spin the instrument smoothly. Thus, the accuracy with which we can determine the tip angle of the spin axis to the direction of the sun can be

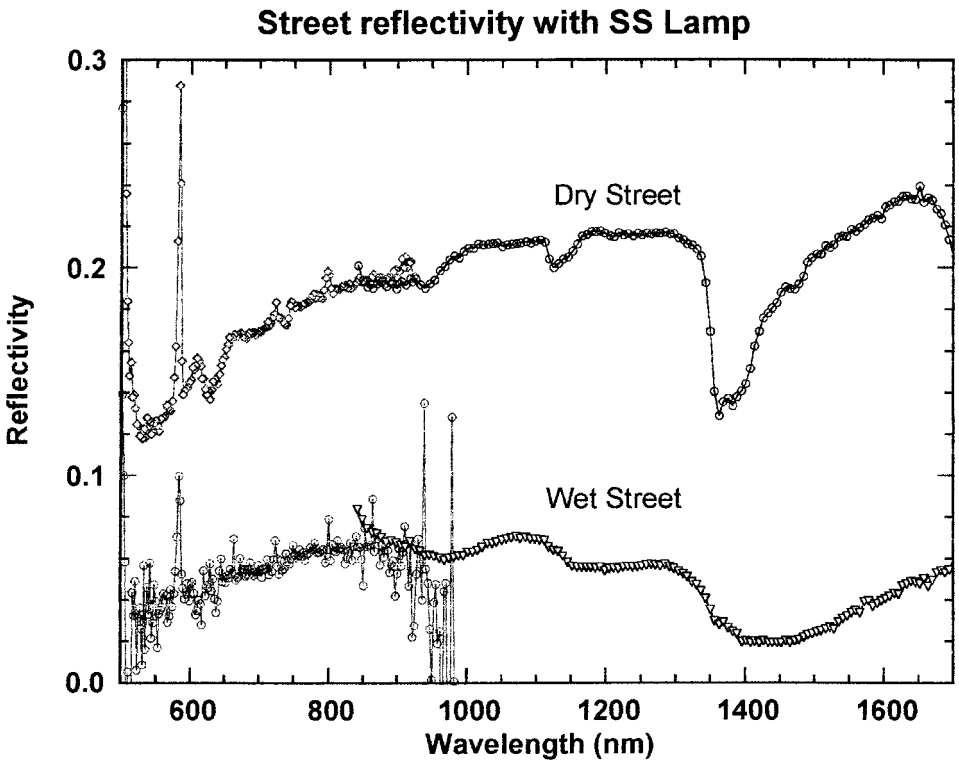

Figure 50. The reflection spectrum of a dirty paved street behind the Lunar and Planetary Labortory of the University of Arizona measured after dark using the Surface Science Lamp of DISR02 mounted some 20 m above the street. The upper curve is the the dry street, while the lower curve is for the street after wetting the street with a garden hose. The emission feature near 580 nm is from emission line street lamps in the area. The absorptions near 950, 1130, and 1380 nm in the 'dry street' reflectivity curve are due to the water vapor in the path between the instrument and the street. Note that the shape of the water absorptions are broader for the liquid water in the 'wet street' spectrum.

determined to an accuracy comparable to the angular resolution of our best imaging data (0.12°).

Figure 53 shows the values of the direct solar beam at the wavelength of the sun sensor (near 940 nm) as a function of airmass for several tests between August 1998 and April 1999. During the July and August tests, clouds built up during the afternoon, and the measured flux from the direct solar beam decreased suddenly several times at the larger airmasses as clouds blocked the direct solar beam. The smooth curves through the points in Figure 53 are models constructed by adjusting two constants: the vertical optical depth of aerosols and the vertical optical depth of water vapor in the 940 nm band. The extinction due to aerosols is linear with airmass, while the extinction due to water vapor varies as the airmass to 0.6 power in this band. On days when the observations spanned a large range of airmass, the vertical optical depths of both the aerosols and the water vapor could be uniquely

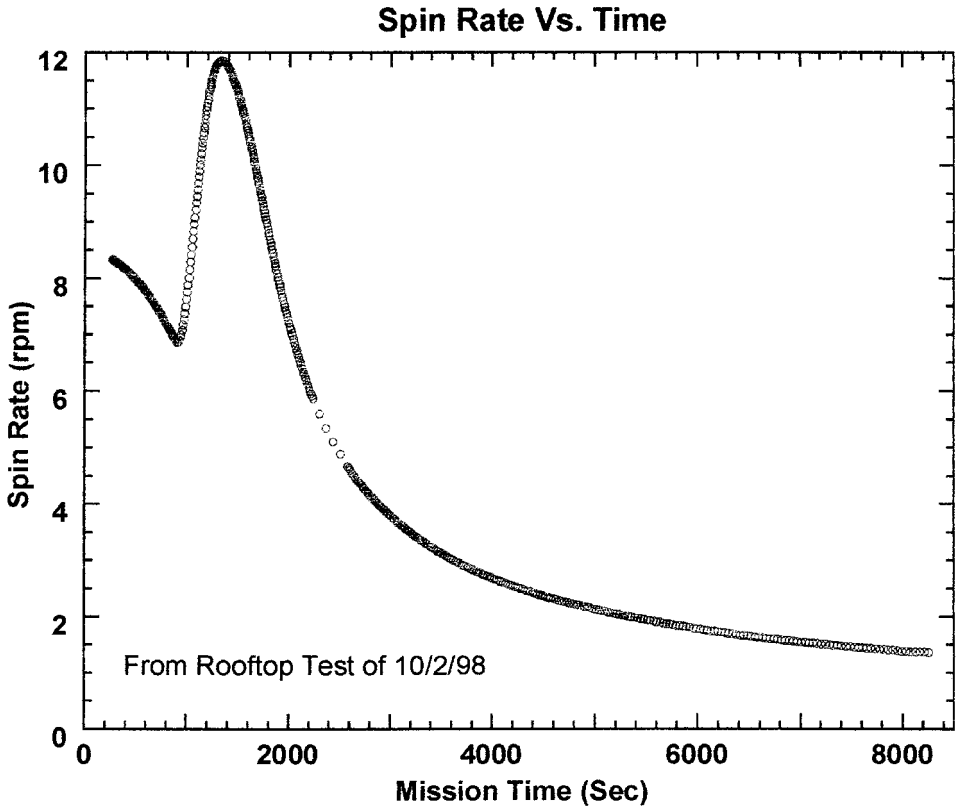

Figure 51. The rotation rate as a function of time determined from the sun sensor during the rooftop test of October 2, 1998. The rotation rate was designed to simulate the rate expected during Titan entry. The sun sensor lost and then reacquired lock a few times near a mission time of 2400 s.

determined from the sun sensor observations alone. Figure 54 shows the vertical column water vapor abundance (in precipitable cm) derived from the vertical water vapor opacity in the 940 nm band of the sun sensor passband as a function of time through the second half of 1998 and the first half of 1999. (One observation in September 1997 was plotted in September 1998.) Also shown are the measurements of dew point recorded on the campus of the University of Arizona. Note that the total vertical water abundance derived from the sun sensor measurements is well correlated with the dew point measurements. Also shown is the first water abundance measurement made on Mt. Bigelow outside of Tucson compared with the dew point measured in the city on that day. The observation on Mt. Bigelow near 9000 ft elevation corresponds to less water than indicated by the dew point measument in the city of Tucson (2400 ft). Both the dew point measurements and the DISR water vertical abundance show the expected increase in atmospheric water in the summer monsoon season followed by a decrease in the cooler and dryer winter months.

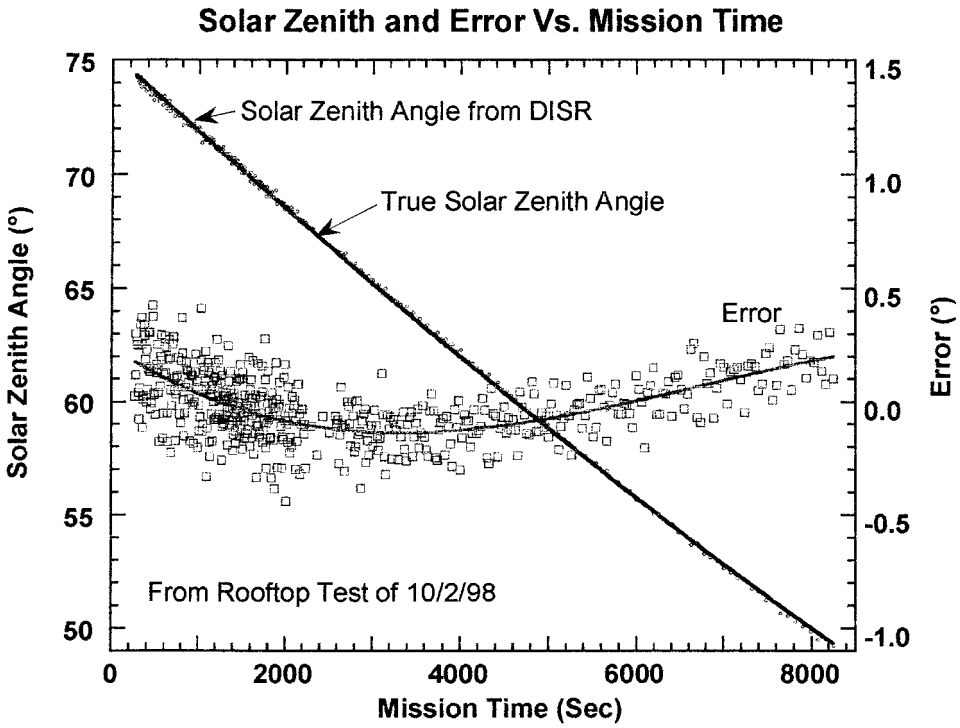

Figure 52. The angle from the instrument vertical (perpendicular to the instrument baseplate) as a function of time compared to the solar zenith angle as a function of time computed from the Astronomical Almanac during the test on October 2, 1998. The error was less than $\pm 0.2°$, corresponding to our ability to hold the baseplate horizontal in our test apparatus. The standard deviation of the error is about $0.12°$ from the mean trend of the error. This is dominated by the ability of our apparatus to rotate the instrument smoothly during each rotation.

The sun sensor wavelength was chosen to fall in a continuum region for the Titan atmosphere, and will be used to provide high time resolution (between 4 and 30 seconds) of the aerosol optical depth . These data will be an important addition to the measurement of the direct solar beam from the ULVS and ULIS at lower time and vertical resolution.

The results of our first test made on the rotating platform with a tipping motion added are shown in Figure 55. Many clouds were present on this day, and the sun sensor kept loosing and reacquiring the sun. Nevertheless, the apparent zenith angles of the sun in the tipping frame of reference of the instrument are shown by the points in the figure. The smooth curve is the expected variation of the apparent zenith angle with time which is the sum of a $2°$ amplitude sine wave with a period of six minutes on the slow setting of the sun with time. The plot demonstrates that we can measure the component of the tip of the instrument baseplate in the direction toward the sun from the sun sensor to an accuracy of some $0.2°$, about the size of a SLI pixel. The relatively slow six minute period was chosen for this test

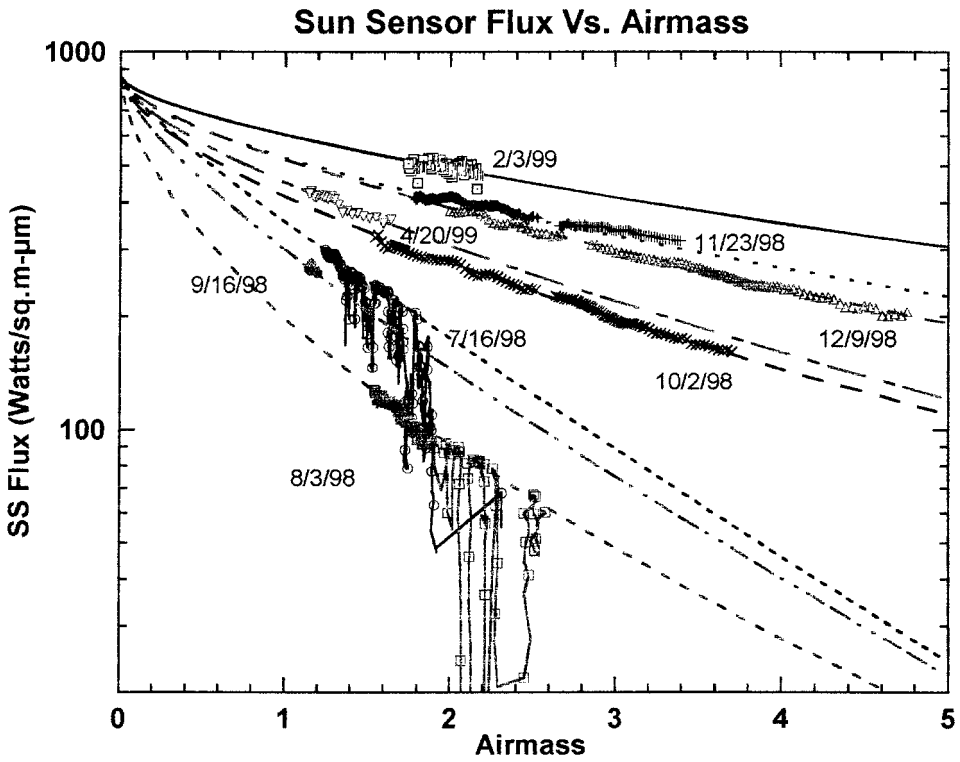

Figure 53. The flux derived from the sun sensor in its passband near 940 nm as a function of airmass during several rooftop tests between August, 1998 and April, 1999, as labeled. The smooth curves are models obtained by adjusting the vertical optical depths of aerosols and water vapor for each day. The aerosol optical depth varies linearly with airmass, while nonlinear the water vapor absorption varies as the arimass to 0.6 power. All the models reach the same value outside the atmosphere (at airmass = 0.0). Thick clouds blocked the solar beam occasionally during the observations in summer monsoon season in July an August.

to be sure that the sine wave would be adequately sampled even in the presence of gaps in the observations due to clouds. On Titan, the oscillation due to wind gusts may be much faster than in this test, but our time resolution will be between several seconds and a few tens of seconds. The sun sensor observations will be able to provide important constraints on the orientation of the probe on each rotation of the spacecraft (some 500 times) during the descent.

The sun sensor attitude information gives the angle between the normal to the instrument platform and the vector to the sun. This is equivalent to the component of the tip of the instrument platform toward the sun. The orthogonal component of the instrument tip (i.e., the component in a direction perpendicular tto the azimuth of the sun) can be constrained by images of the horizon from the SLI. While complete SLI images are only obtained on image cycles, a condensed form of SLI data is obtained during all nonimage cycles. These data include the sum of the

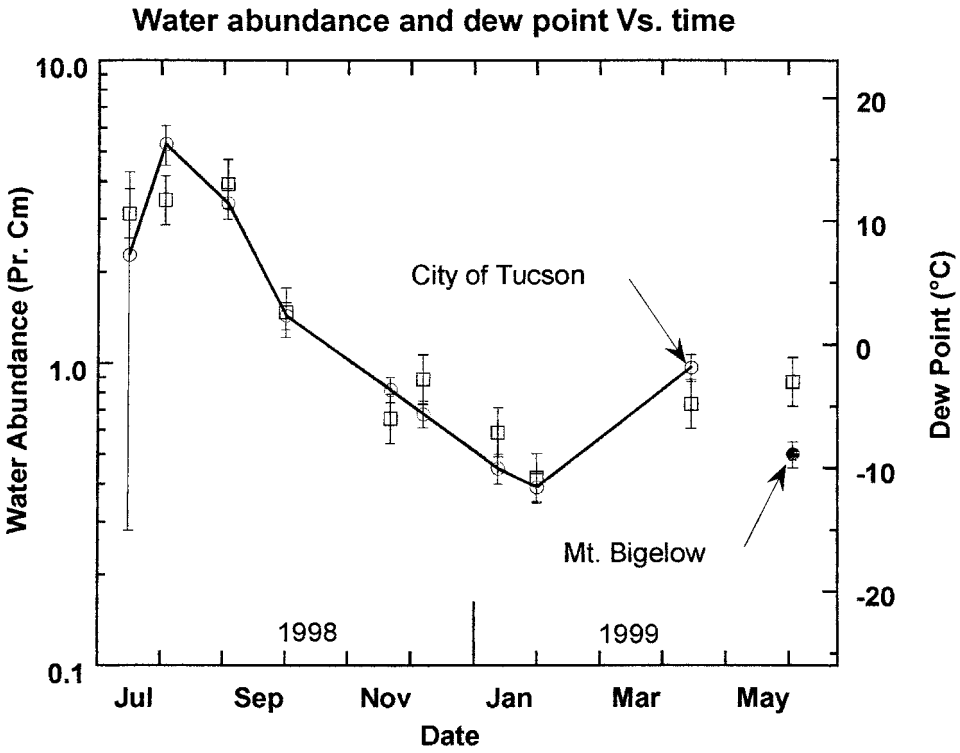

Figure 54. Measurements of dew point (open squares, right scale) measured on the campus of the University of Arizona Vs. time compared with vertical abundance of water vapor (left scale) derived from the vertical water opacity in the 940 nm band of the DISR sun sensor measured on the roof of the Lunar and Planetary Laboratory in Tucson (open circles) and on Mt. Bigelow at an elevation of some 9000 feet (solid point) outside the city of Tucson. The dew point and water abundance plotted in September 1998 were actually observed in September of 1997. The error bar on the July observation is particularly great because the afternoon clouds shortened the range of airmass sampled, and the total vertical opacity in the sun sensor passband could less reliably separated into linear aerosol opacity and nonlinear water vapor opacity. The correlation of the dew point measurements (which varied by a few degrees during the DISR observations) and the vertical column water abundance observed by DISR for the measurements in Tucson is evident. As expected, the water abundance above the Mt. Bigelow site is less than would be expected from the dew point measured at the lower elevation (2400 ft) in the city of Tucson.

intensity in two vertical regions each 13 CCD columns wide (2.6°) and 50° high at six different azimuths relative to the sun. Thus, the SLI image and SLI strip data will be able to constrain the other component of the tip of the instrument platform some 50 times during the descent. Data on platform orientation at still higher time resolution will have to come from other housekeeping observations or from fitting together mosaics from our individual imaging frames which are obtained several times per rotation low in Titan's atmosphere.

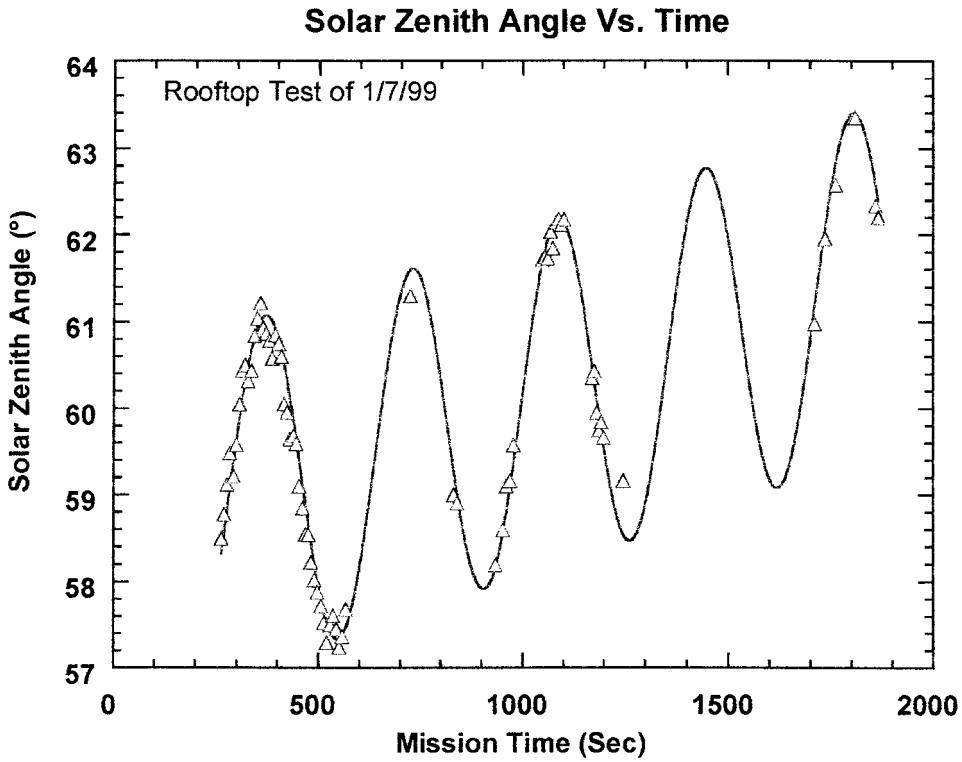

Figure 55. The solar zenith angle measured by the DISR during a test in which the instrument rotated and also tipped toward and away from the sun. The points are the measured values. The smooth curve is the expected variation from the sinusoidal tip of 2° amplitude and 6 minutes period superimposed on the increasing zenith angle of the sun as the sun set. The DISR measurements are generally within about 0.2° of the expected values.

5.9. VIOLET PHOTOMETER MEASUREMENTS

Ideally, one would like to have a perfectly flat spectral response with sharp cuton and cutoff wavelengths in the violet photometer system in order to eliminate any sensitivity to the shape of the violet spectrum when the ULV and DLV data are reduced to give the energy in the upward and downward flux between the wavelength limits of the filter. While the filters of the ULV and DLV systems are not absolutely flat, they are flat to about 15 percent. Further, it is possible to choose the three parameters of an equivalent rectangular filter (cuton wavelength, cutoff wavelength, and effective mean response) that give exactly the correct flux in an arbitrary spectrum that can be described by up to a second order polynomial in wavelength (Tomasko *et al.*, 1980). For our ULV and DLV photometers the cuton and cutoff wavelengths defined this way are 350 nm and 475 nm, respectively. While the solar spectrum is far from quadratic in the violet region of the spectrum, most of the structure is due to sharp absorption lines that have a structure much finer than the variation

in response with wavelength of our violet filter. Test calculations show that we can give a model-independent flux between the cuton and cutoff wavelengths that is uncertain by <1% (aside from absolute calibration uncertainties) instead of the 15% or so that one might guess from the departure from flatness of our violet filter. Of course, the constraint on the integral of the violet spectrum times the relative spectral response of the ULV and DLV instruments is well determined, and can be used to constrain any model of the spectrum and level of violet radiation in Titan's atmosphere.

The violet photometers have a fixed gain and time constant appropriate for Titan, and give saturated readings on Earth without the addition of an external filter. In general, simply adding a glass neutral density filter on the top of the diffusers will change significantly the relative spatial response of the violet optical system consisting of the external bear's ear baffle and the diffuser. However, we have been able to add a thin sheet of absorbing material to the top of the external diffuser in the ULV, ULVS, and DLV systems which has changed the spatial distribution function rather little from the values measured in our laboratory calibration to permit unsaturated measurements of violet flux in our rooftop measurement program. This filter consists of a small piece of high contrast black and white 35 mm film that was exposed to image a target consisting of evenly distributed black circles on a white background. In the negative image, the film consists of absorbing black grains surrounding a pattern of clear circles. The spacing and size of the circles are arranged so that the area of the circles is approximately 1% of the total area. The circles are arranged so that the 4 by 5 mm diffuser is covered by a grid of some 40 rows of 50 holes each, thus sampling the total area of the diffuser. Little light is reflected from the black emulsion to the external baffles and then back to the diffuser, so the spatial response pattern is largely unchanged from the pattern measured before the film filter was added.

The relative spatial response in not entirely unchanged, however. The substrate of the film also attenuates the light that is not blocked by the darkened silver grains. Tests show that the film itself has a vertical optical depth of about 0.07 at the wavelengths of the violet photometers. When the transmission of the filter and its modification of spatial response function due to the film are included, however, measurements with the ULVand DLV systems are possible on Earth.

The results of one set of measurements with this sysem are shown in Figures 56 and 57. The values of the direct solar beam in the violet fall exponentially with increasing airmass over the region from about 2.2 to 4.6 airmasses, as would be expected. The data indicate that the optical depth for unit vertical airmass was about 0.48 in the violet passband on this day. The cosine of the zenith angle times the direct solar beam gives the downward direct flux in the violet channel. The mean diffuse intensity is measured using the 170° wide field of view in azimuth looking 180° from the sun and within 5° of the sun under the shadow bar. The diffuse intensity convolved with the wide azimuthal field of view varies to a good approximation as the cosine of the azimuth from the sun. The spatial response of

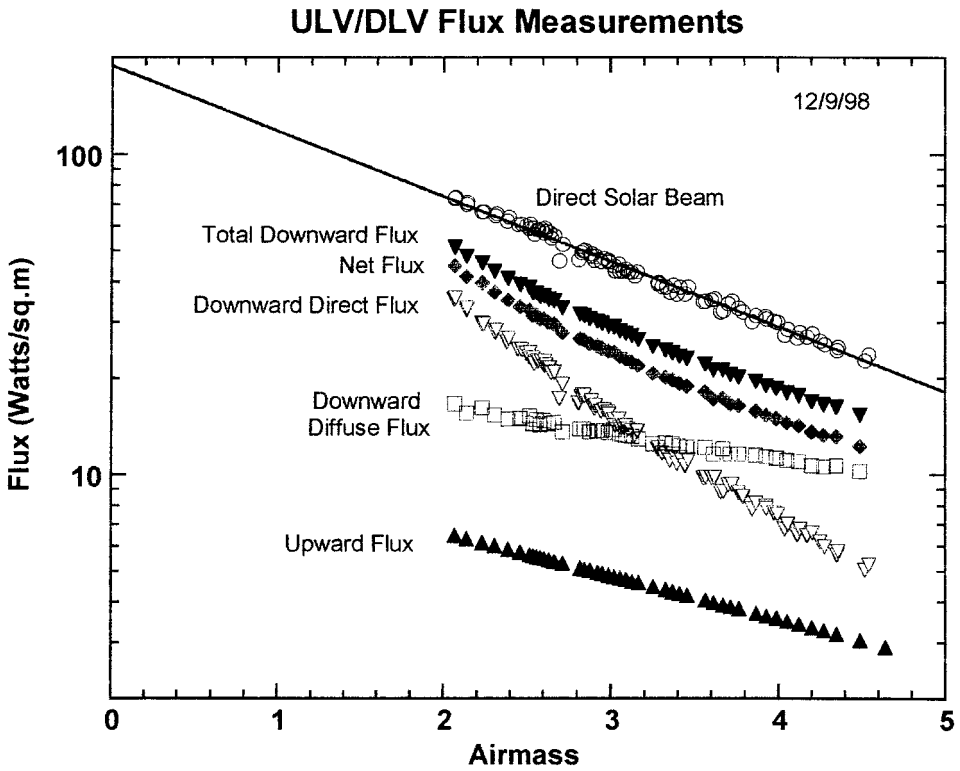

Figure 56. The log of the flux plotted against airmass from test data obtained from the violet photometers on 12/9/98. The open circles are for the direct solar beam. The direct downward flux, the diffuse downward flux, the total downward flux, the upward flux, and the net flux are also shown as labeled.

the ULV and DLV diffusers in zenith angle approximates a cosine response, so π times the measured mean intensity is a good approximation to the downward diffuse flux. The total of the downward diffuse flux and the downward direct flux gives the total downward flux is shown in Figure 55. The upward diffuse flux is obtained from the average of the DLV mean intensities measured with the 170° wide field of view in azimuth measured at 0° and 180° azimuth with the approximately cosine weighting in nadir angle. The total upward flux versus airmass, as well as the total downward minus upward flux, (the net flux) are shown as functions of airmass. Figure 56 shows the total downward, upward, and net fluxes on a linear scale versus airmass. The derivative of such net flux measurements on Titan will give the solar heating rate as a function of altitude due to sunlight between 350 and 475 nm.

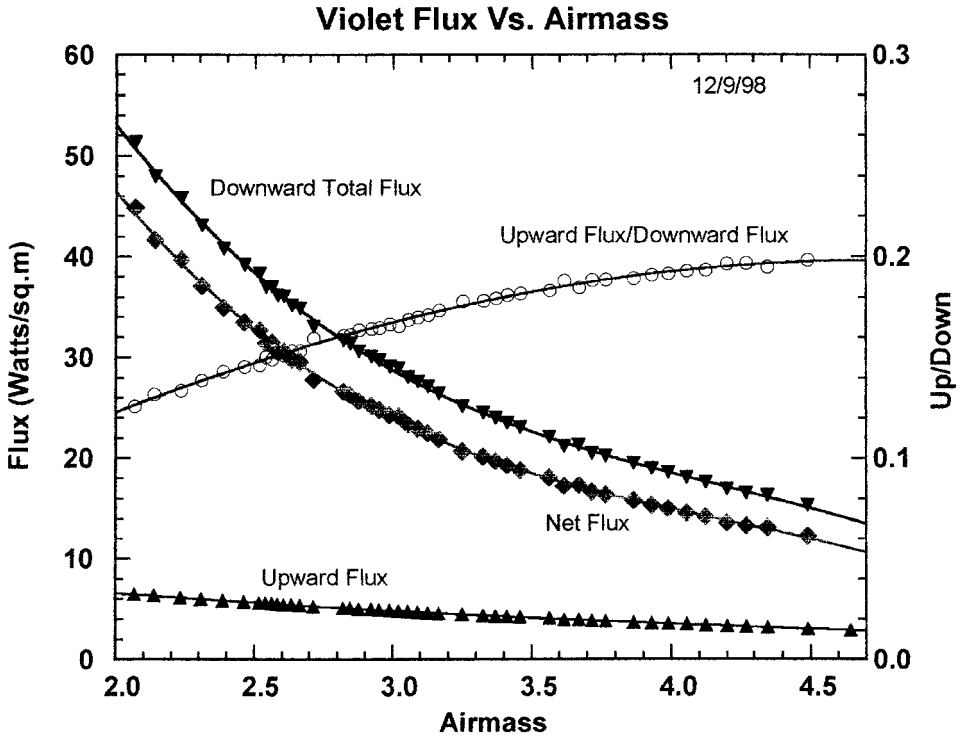

Figure 57. The total upward, downward, and net violet flux between 350 and 475 nm as a function of airmass are shown on a linear scale. Also shown on the right hand scale are the ratio of the upward/downward violet flux. This ratio represents the effective reflectivity of the surface, and shows a modest increase as the elevation angle of the sun decreases (the airmass increases).

5.10. FUTURE PLANS

We have recently added a programmable wobble to the spinning platform to test and simulate the operation of the instrument under a swinging parachute. During this phase of our tests we have begun to make panoramic mosaic images of the Tucson valley from a U.S. Forest Service tower on the top of one of the surrounding mountains. This will give us valuable information on the ability of our housekeeping data from the sun sensor and from the SLI strip data obtained in each data cycle at 6 different azimuths to yield the attitude of the platform during the descent to permit more automatic assembly of image mosaics from our Titan entry observations. The attitude of the instrument is also needed for reduction of our flux and solar aureole observations as well as our goal of measuring winds from the drift of features in images obtained at different times.

In addition, we are currently planning a series of test images made from various heights between 5 and 15 meters of specially constructed targets. The data will be used to develop and test algorithms for finding the heights of features in the images from data acquired at various altitudes above the surface. Ultimately, we hope to

develop a capability to produce stereographic maps of the heights of the terrain in our Titan images.

5.11. SUMMARY

We have included brief samples of data from each portion of the field test unit including ULVS, DLVS, ULIS, DLIS, ULV, DLV, SA, Imagers, Sun Sensor,and Surface Science Lamp. This ground test program has proven very valuable for developing reduction, display, and analysis algorithms that will be necessary to reduce the complex data from the DISR instrument rapidly after entry into the atmosphere of Titan. Already, the brief samples of data shown provide convincing evidence of the value of the data anticipated from the experiment to support the goals for studies of energy balance, aerosol properties, gaseous composition, and the nature of the surface of Titan.

Acknowledgements

The planning, design, development, fabrication, and test of the DISR instrument would not be possible without the collaboration of a large number of dedicated and highly talented individuals. We wish to especially thank the many dedicated contributors at Lockheed Martin Aerospace, Denver and their suppliers, for their work on the design and development of the mechanical, optical, electrical and software of the DISR instrument; the engineers and technicians of the Paris Observatory for their work on the infrared detectors, their support electronics, and the shutter; the people of the Max Planck Institute for Aeronomy for their work on the design of the CCD detector and its read electronics; and the engineers of the Technical University of Braunschweig for their design and development of the data compression hardware. Without the dedicated efforts of all these people the DISR would not be possible.

References

Bark, A, Bernstein, L. S. and Robertson, D. C.: 1989, MODTRAN: A Moderate Resolution Model for LOWTRAN7, GL-TR-89-0122.

Bodin, P. and Reulet, J. F.: 1987, A New Channel for SPOT in the SWIR Band, *S.P.I.E.*, **865**, 142–149.

Dave, J. V.: 1971, Determination of size distribution of spherical polydispersions using scattered radiation data, *Appl. Opt.* **10**, 2035–2044.

Hapke, B.: 1981, Bidirectional Reflectance Spectroscopy 1. Theory, *J. Geophys. Res.*, **86**, 3039–3054.

Hoffman, J. H., Hodges, R. R., Donahue, T. M., and McElroy, M. B.: 1980, Composition of the Venus Lower Atmosphere from the Pioneer Venus Mass Spectrometer, *J. Geophys. Res.*, **85**, 7882–7890.

Hunten, D., Tomasko, M. G., Flasar, F. M., Samuelson, R. E., Strobel, D. F., and Stevenson, D. J.: 1985, Titan, in Saturn, T. Gehrels and Matthews, M. S., editors, University of Arizona Press, 671–759.

Lemmon, M. T., Karkoschka, E., and Tomasko, M.: 1995, Titan's rotational light curve, *Icarus*, **113**, 27–38.

Lunine, J. I.: 1993, Does Titan have an ocean? A review of current understanding of Titan's surface, *Rev. Geophysics* **31**, 133–149.

Lunine, J., Flasar, F. M., and Allison, M.: 1991, Huygens Probe Wind Drift: Science Issues and Recommendations, A Report to the Huygens Project.

Nakajima, T., Masayuki, T., and Yamauchi, T.: 1983, Retrieval of the optical properties of aerosols from aureole and extinction data, *Appl. Opt.* **22**, 2951–2959.

Neckel, Heinz and Dietrich Labs: 1984, The Solar Radiation Between 3300 and 12 500 Å, *Solar Physics* **90**, 205–258.

Remer, L. A., Gasso, S., Hegg, D. A., Kaufman, Y. J., and Holben, B. N.: 1997, Urban/industrial aerosol: Ground-based Sun/sky radiometer and airmorne in situ measurements, *J. Geophys. Res.* **102**, 16849–16859.

Smith, P. H., Lemmon, M. T., Lorenz, R. D., Sromovsky, L. A., Caldwell, J. J., and Allison, M. D.: 1996, Titan's surface reaveled by HST imaging, *Icarus*, **119**, 226–349.

Tomasko, M. G., Doose, L. R., Smith, P. H., Fellows, C., Rizk, B., See, C., Bushroe, M., McFarlane, E., Wegryn, E., Frans, E., Clark, R., Prout, M., and Clapp, S.: 1996, The Descent Imager/Spectral Radiometer (DISR) Instrument aboard the Huygens Probe of Titan, *SPIE Proceedings*, **2803**, 64–74.

Tomasko, M, G., Doose, L. R., Smith, P. H., and Odell, A. P.: 1980: Measurements of the Flux of Sunlight in the Atmosphere of Venus, *J. Geophys. Res.*, **85**, 8167–8186.

Tomasko, M. G., Doose, L. R., Smith, P. H., West, R. A., Soderblom, L. A., Combes, M., Bézard, B., Coustenis, A., deBergh, C., Lellouch, E., Rosenqvist, J., St.-Pé, O., Schmidt, B., Keller, H. U., Thomas, N., and Gliem, F.: 1997, The Descent Imager/Spectral Radiometer (DISR) Instrument Aboard the Huygens Entry Probe of Titan, ESA SP-1177, 109–138.